Acoustic emission source detection and wave generation on a working plate using piezoelectric actuators

PAR

Xinchang LIU

ÉCOLE POLYTECHNIQUE
FÉDÉRALE DE LAUSANNE

Suisse
2017

Thus in each specific event, there is the germ of a whole class of similar events. This idea that there is generality in the specific is of far-reaching importance.

— **Douglas R. Hofstadter**, *Gödel, Escher, Bach: An Eternal Golden Braid*

Acknowledgments

This thesis has emerged from my time as doctor student and teaching assistant at the Integrated Actuator Laboratory (LAI) of EPFL.

First of all, I would like to express my sincere gratitude to Prof. Dr Yves Perriard for providing the opportunity to join his laboratory after my Master project. I really appreciate all his efforts to conduct a perfect research team and to maintain a convivial working atmosphere. Special thanks to our industrial partner who financed and participated in this project and to all the industrial collaborators: Mr Jean-Charles Authier, Mr Oliver Chopard, and Mr Michael Egg. I would also like to thank Dr Shi Dan who contributed a lot of interesting work to this project.

I would especially like to thank Mr Paolo Germano for the help in preparing all the experiments and, most importantly, for revising my thesis. His suggestive advices and discussions were indispensable for me to finalise my thesis. I also appreciate the advices I got from Dr Yoan Civet during my writing.

I would like to mention my colleagues and former colleagues, Daniel, Florian, Pascal, Greg, Chris, Tof, Jonathan, Cécile, Douglas, Christian, Jasha, Guillaume, Louis, Jiantao. All the discussions we had together were helpful and the time I spent with you was unforgettable especially in special laboratory events. I also thank our secretaries, Magda, Myriam and Mrs Sandrine Piffaretti for all administrative help.

Finally I would like to thank all my family. They have been extremely supportive of me throughout all my studies.

Neuchâtel, April 9th, 2017
Xinchang LIU

i

Abstract

In modern automated assembly lines, part feeders play an important role to separate and sort parts. Agility and flexibility are required to achieve a good yield for different types of parts. The common working principle is to vibrate a working plate driven by electromagnetic actuators in order to orient or separate parts on it. Then, a vision system will help a robotic arm to pick up the parts if they are correctly placed. However, the vibration can only create a random movement for the parts. Hence, a new design of working plate using piezoelectric actuators has been proposed to solve this problem.

This thesis presents the modelling of the piezoelectric actuator driven working plate in order to provide a theoretical tool to explore the full potential of this new design. Despite of directly using eigenmodes to create non-homogeneous vibrations, it is also possible to use the piezoelectric actuator to detect the position of parts or to create a vibration at a specific position. An overview of possible technics which can achieve these tasks is presented. Among all solutions, the time-reversal method shows it is the best candidate.

According to the time-reversal method, an excitation pulse response is the key element to establish the theoretical study. Firstly, the expression of vibration amplitude on a plate due to an excitation pulse has been given. A damping term is added to the result, which can be determined by impedance measurement thanks to the modelling of the electrical characteristics of the coupled piezoelectric-mechanical system.

The second part deals with the detection. After the modelling of the interaction between the piezoelectric actuator and the plate, the complete time-reversal process modelling can be achieved. An example of its application on a beam is given, which shows the restored vibration amplitude has one main peak at the original position of the excitation and several smaller associated peaks elsewhere. This result demonstrates it is sufficient to detect a part dropping position with the time-reversal method.

The third part focuses on the pulse generation. The associated peaks can be removed by a combination of several excitation pulse responses. The position of piezoelectric actuators should also meet conditions predicted by theoretical analysis. The damping term is equally taken into consideration to improve the pulse reconstruction.

In parallel, the design of an electric drive for such piezoelectric system is also a challenge, due

to the great capacitance of the piezoelectric actuator, high supply voltage and wide dynamic frequency range. A solution based on self-oscillating class-D amplifiers has been proposed because it allows reaching nearly the frequency limit of the switching components. The theoretical study gives a complete modelling of the system and it implies a stability condition for the choice of the parameters. The output of this drive is a non-periodic PWM (Pulse Width Modulation) signal. An original method is proposed to give a theoretical estimation of the frequency spectrum, which is useful to determine the cutoff frequency of the output low-pass filter.

At the end, simulations and experiments are given to verify the theoretical results and to show the effectiveness to detect excitation pulse positions and the possibility to create a pulse vibration at a specific position.

Résumé

Dans une ligne d'assemblage automatisée moderne, l'alimentation de pièces joue un rôle important pour séparer et trier les pièces. Agilité et flexibilité sont nécessaires pour obtenir une bonne efficacité pour différents types de pièces. Un principe de fonctionnement courant est de faire vibrer une plaque de travail entraînée par des actionneurs électromagnétiques afin d'orienter ou de séparer les pièces sur celle-ci. Un bras robotisé est utilisé pour saisir les pièces, aidé d'un système de vision pour autant qu'elles aient été correctement placées. Cependant, la vibration ne peut créer qu'un mouvement aléatoire des pièces. Par conséquent, une nouvelle conception de plaque de travail utilisant des actionneurs piézoélectrique a été proposée pour résoudre ce problème.

Dans le cadre de cette thèse, la modélisation de la plaque de travail entraînée par des actionneurs piézoélectriques est présentée. Ceci permet de fournir un outil théorique pour étudier le potentiel de cette nouvelle conception. Outre l'utilisation directe des modes propres pour créer des vibrations non homogènes, il est également possible d'utiliser des actionneurs piézoélectriques pour détecter la position de chute des pièces ou pour créer une vibration à une position spécifique. Un état de l'art sur les techniques permettant de réaliser ces fonctionnements est présenté. Parmi toutes les solutions possibles, on montre que la méthode de retournement temporel est la meilleure candidate.

D'après la méthode de retournement temporel, l'étude de la réponse due à une impulsion est la clé pour élaborer une analyse théorique. Dans un premier temps, l'expression de l'amplitude de vibration sur une plaque due à une impulsion a été donnée. Un terme d'amortissement est introduit dans le résultat et il peut être déterminé par une mesure d'impédance grâce à la modélisation de caractéristique électrique du système piézo-mécanique.

Deuxèmement, pour le cas de la détection, la modélisation de l'interaction entre les actionneurs piézoélectriques et la plaque est établie. Puis, l'étude porte sur la modélisation complète du retournement temporel. L'application sur une barre est donnée comme exemple. Il montre que l'amplitude de vibration restaurée possède un pic principal à la position originale de l'excitation, mais plusieurs pics associés plus faibles se trouvent ailleurs. Ce résultat démontre qu'il suffit de détecter la position de chute d'une pièce avec cette méthode de retournement temporel.

Troisièment, la génération d'impulsions est présentée. Les pics associés peuvent être éliminés par une combinaison de plusieurs réponses impulsionnelles. La position des actionneurs piézoélectriques devrait également répondre aux conditions prédites par l'analyse théorique. Le terme d'amortissement est également pris en compte pour améliorer le résultat de reconstruction des impulsions.

Parallèlement, la conception d'une alimentation électrique pour le système piézoélectrique est également entreprise pour satisfaire le besoin d'alimenter la capacité de grande valeur de l'actionneur piézoélectrique, de fournir une haute tension d'alimentation ainsi qu'une grande dynamique pour la variation de fréquences. Une solution basée sur un amplificateur de classe D à auto-oscillation a été proposée car elle permet d'approcher la limite de fréquence des composants de commutation. L'étude théorique donne une modélisation complète du système et indique une condition de stabilité pour les paramètres. Le signal de sortie est de type de PWM(MLI) non-périodique. Une méthode originale dédiée à l'analyse spectrale est proposée. Elle peut être utilisée pour déterminer la fréquence de coupure du filtre passe-bas à la sortie.

Finalement, des simulations et des expériences sont données pour vérifier les résultats théoriques et pour montrer la faisabilité de détection des positions d'excitation et de créer une vibration d'impulsion à un endroit donné.

Mots clefs : *Actionneur piézoélectrique, Vibration, Alimentation de pièces, Plaque de travail, Retournement temporel, Detection de source acoustique, Auto-oscillation, Amplificateur de classe D, MLI non-périodique.*

Contents

Contents

Contents

List of Figures

List of Tables

1 Introduction

1.1 Assembly automation for mass production

The assembly automation aims to create standard parts and to reduce the requirement of manpower in a manufacturing line for mass production in order to improve the scalability and efficiency.

The first attempt of this idea can be dated back to 1798. One of the pioneers in mass production, Eli Whitney, applied the concept of interchangeable parts for the manufacturing of muskets during the Quasi-War [15]. His idea achieved a great success in that days. In his blueprint, the machines were used during the manufacturing, which guaranteed the quality of the parts. In this way, the parts do not need to be worked to fit in with the other parts and the assembly process could be significantly simplified. All of this resulted in the improvement of the efficiency and allowed his company to finish the contract of 10,000 muskets.

In the nineteenth century, the method for mass production spread out to private factories in the U.S.. Eli Terry's improved the assembly and large production problem. David Hinman and Elisha K. Root invented axe-manufacturing machinery and changed both the process and the product. William K. Jenne and Jefferson Clough redesigned the Sholes & Glidden typewriter to adapt the mass production in his factory [44]. These talent inventors and mechanicians joined the trend to improve the technology. They redesigned their products and assembly lines in the way to adapt the mass production. The innovation helped them not only for success in the market but also to create new concepts.

Another well-known millstone for the assembly automation in mass production is Ford's Model T manufacturing line in 1908. His major principles can be concluded: the standardisation of product, the use of special-purpose equipment and the elimination of skilled labour in direct production [6]. Although he is not the first man who proposed and applied all these rules, but he is the first one who showed the full potential of such continuous assembly line with a record of 15 million cars sold by the end of 1926 [6].

In 1961, George Devol published the "Programmed Article Transfer" patent [27] which is considered as the very first step which granted the robotic arm in manufacturing lines [5]. It allowed replacing workers from dangerous conditions or repetitious tasks. Furthermore, it described indeed a general purpose machine which made modern assembly lines more flexible and with less human intervention.

Since 1970s, different robotic arms have been developed for assembly purpose: the PUMA (Programmable Universal Machine for Assembly) was developed for General Motors and was based on a design from the Stanford University [9]. The SCARA (Selective Compliance Assembly Robot Arm) was designed in the Yamanashi University [74]. An other parallel robot, the Delta robot, was created at EPFL[24]. All of these robot arms use different kind of mechanical structures but with the same objective: to handle parts in the 3D space. They can all be used in production lines to pick up and move parts from one position to another, which is considered as the elementary operation in assembly processes.

Nowadays, automated assembly production lines have been widely applied for different types of part. A typical system for small parts is shown in Fig. 1.1. It normally contains a feeding system, a convoy system, a vision-based robotic arm and the box for part placing. The main objective is to sort the parts and place them in oder for the next operations.
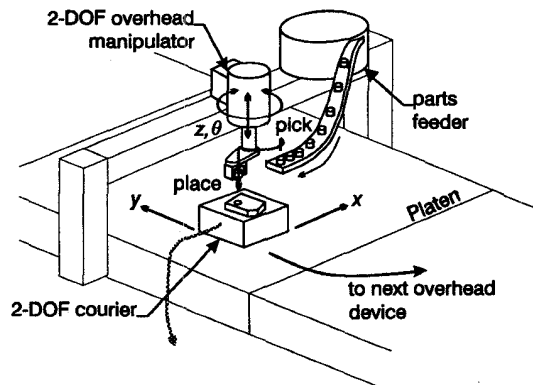
Figure 1.1 – Assembly robot [83]

1.2 Part feeders

Part feeders are devices used in manufacturing lines for the assembly or packaging process. It permits to handle the position or orientation of the parts in order to achieve certain assembling operations. Together with the development of the mass production method, the evolution of part feeders facilitate the automation, improve the efficiency and reduce the cost for the production.

The most common part feeder is the bowl feeder. As shown in Fig. 1.2, the unsorted parts can be put inside the bowl. The electromagnet actuator will vibrate the bowl so that the parts will

move up through the spiral track at the interior edge of the bowl. With specific designs of the motion filter on the track, the parts will drop back to the centre of the bowl if they are in an undesirable orientation. Only the ones in predefined orientation can come out from the outlet [19][11][46].
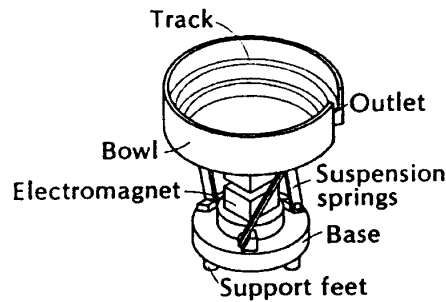
Figure 1.2 – Bowl feeder [16]

In modern manufacture lines, the flexibility becomes more and more important. As the bowl feeder requires specific mechanical filter designed for each kind of parts, it cannot be quickly reconfigured to adapt different types of part or to agilely handle the change of the design of a part. After the introduction of robotic arms and computer vision systems, the way of feeding parts has changed a lot. The system parameters can be reconfigured depending on different kind of parts. It can not only work with parts fed in order [83], but also with multiple ones fed at the same time [87]. The latter can help avoid the complex sorting system, which is especially useful for small parts difficult to be sorted.
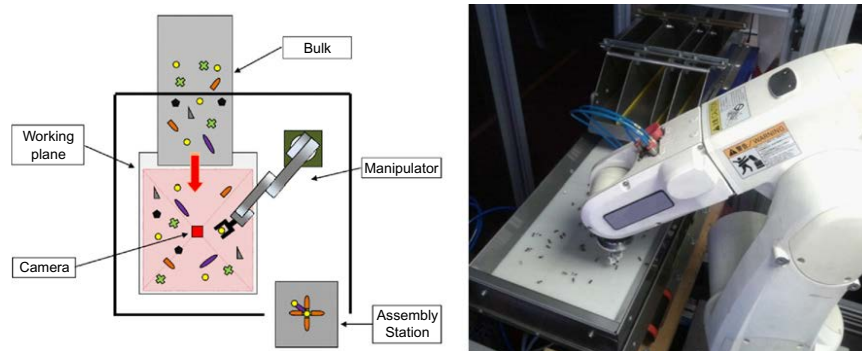
Figure 1.3 – Flexible assembly system [87]

The working plate shown in Fig. 1.3 is the place where the manipulator picks up the parts. According to the computer vision algorithm used for the position recognition, it is important to have parts separated from each other. Multiple designs can be found to satisfy this requirement. Two passive solutions are shown in Fig. 1.4. They use either a ramp or free drop to separate parts before they enter into the vision area. However, if the parts are not initially separated or well oriented, they will have no chance to be put in a correct way and should be then sent

3
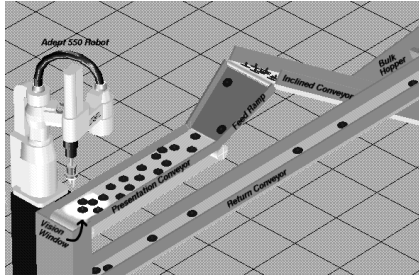
(a) Part feeder using a ramp [21]   (b) Part feeder using a wiper and free drop [50]
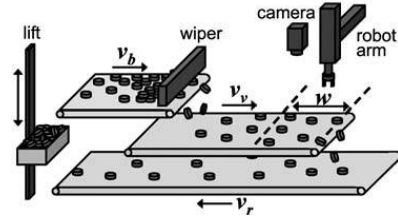
Figure 1.4 – Passive flexible feeding system

back with a return conveyor.

In order to improve the yield of the part feeding system and to facilitate the operations based on vision system, a vibratory working plate has been applied for the part separation purpose. Fig. 1.5 shows a typic design of this solution. The working plate is driven by a linear electromagnetic actuator, which can vibrate vertically the plate and the parts [17]. According to the size and shape of the parts, the vibration frequency and amplitude can be adjusted to separate or flip the parts. More operations can also be realised by adding more degrees of freedom to the working plate, as presented in [78].
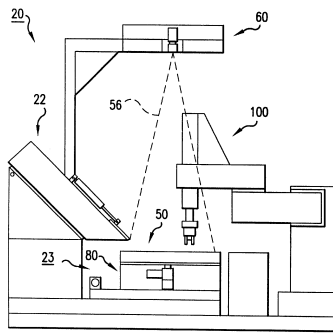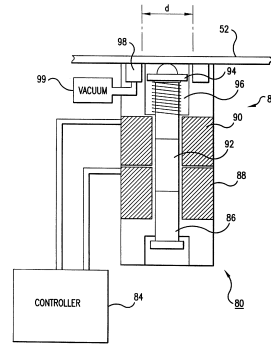
(a) System diagram   (b) Working plate and the linear actuator

Figure 1.5 – Vibratory flexible feeding system [17]

The vibratory working plate can reposition the parts while they are inside the vision area. However, with the electromagnetic actuator working at relative low frequencies, the plate is considered as a solid body. The parts laying on it will receive nearly the same impact from the plate and jump up in almost the same way. Due to the random nature of movement, two parts stuck together can still be separated from each other after several vibration cycles. But, it is not the most efficient method.

1.3 Working plate using eigen modes

If the plate vibrates at its resonant frequency, the eigen modes will be excited and the distribution of displacement along the plate will be no more uniform. The parts at different positions receive different impacts. In general, parts tend to move toward the nearest node of the eigen mode, thus, it allows repositioning the parts to specific places on a plate. A study on the part positioning using eigen modes is reported in [14]. As shown in Fig. 1.6, an electromagnetic shaker has been used. The mentioned working frequency is between 20 Hz and 100 Hz for a thin and large working plate, which is in the range of the vibration frequency of an electromagnetic vibrator.

(a) Vibrator and working plate (b) Eigen mode at 100 Hz
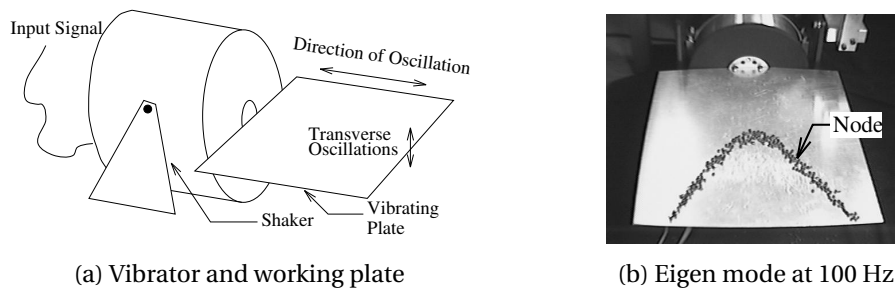
Figure 1.6 – Working plate using eigen mode [17]

The eigen frequency is related to the size of the plate. The smaller the plate is, the higher its eigen frequencies are. In recent studies [90], piezoelectric actuators have been applied to overcome the limitation of electromagnetic shakers: the miniaturisation problem and the frequency range. This innovation makes part feeders using eigen modes more compact and flexible.

By switching between different eigen modes consequently, the parts on the working plate can be displaced in a specific direction. Besides, because the horizontal velocity of a moving part depends on the distance between itself and the nearest node, with a well selected combination
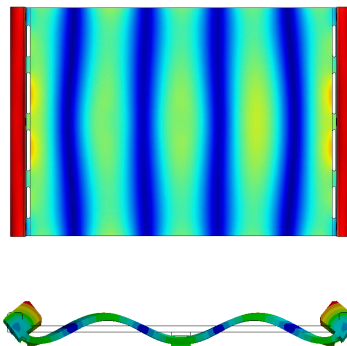
Figure 1.7 – The using of an eigen mode on a working plate excited by piezoelectric actuators [90]

of eigen modes, the separation operation based on vibration is no longer a fully random process. Thus, the part feeder becomes more controllable and efficient[90].

Thanks to the properties of the piezoelectric actuator, the part feeder based on such devices can still be improved in different directions: the piezoelectric actuators can also work as sensors, which makes it possible to detect the parts on the tooling plate; it has a fast reaction time to the input signal, which allows using not only a sinusoidal input signal but also an arbitrary input signal to create specific waves on the plate.

1.4   Scope of this study

According to the previous studies, working plates driven by piezoelectric actuators become quite interesting for parts separation and related operations. As it is still a new technology introduced to assembly systems, this thesis intends to fully study its mechanism and to propose new potential operating principles for working plates. As a result, this work will focus on the following themes:

Wave creation mechanism of the working plate driven by piezoelectric actuators   The modelling of the system is essential to understand the mechanism for waves creation. The piezoelectric actuator is indeed an acoustic emission source to generate waves. The theoretical study can also help optimise the parameters for the system design and select the position for the actuators.

Initial part dropping position detection   Dropping of the parts on the plate will generate impacts on the plate. The piezoelectric actuator can also be used as a sensor to detect the wave caused by this impact. The good understanding of the mechanism is the key point to achieve a precise result. According to the system model established in previous themes, information can be extracted more efficiently. Non-trivial cases such as multiple parts dropping will also be studied.

Customised impact generation   Eigen modes will create a non-uniform displacement field on the working plate. All the parts placed at the non-node positions of an eigen mode will receive the impact. However, for two parts stuck together at a position, a displacement at that specific position will be sufficient to separate them. Thus, it will be interesting to create an impact at one position and do not affect the parts at other positions. According to the wave generation mechanism, this operation could be realisable.

Piezoelectric actuator driving technology   Piezoelectric actuators can be considered as capacitive loads for the driver. Due to the wide range of working frequencies from several kHz

to several tens of kHz and at a relative high voltage (150 V), available commercial drivers do not meet such requirements and it can be a challenge to develop a new design of piezoelectric actuator drives working at these conditions.

This thesis consists of the themes mentioned previously. Each subject contains new ideas or new theoretical developments and the whole work is intended for in innovative part feeder design in assembly automation.

1.5   Structure of this work

This work is organised as follows:

In chapter 2, the state of the art for the related subjects is investigated. According to the objectives of this study, three different topics will be mentioned including position detection on a surface using acoustic source emission detection methods, pulse wave generation and the possible designs for the piezoelectric actuator drive.

Chapter 3 discusses firstly the theory for piezoelectric actuators modelling and for vibratory plates will also be introduced. Then, the wave generation with a pulse excitation will be studied with the consideration of damping effect.

In chapter 4, according to the plate vibration theory, the emission source detection can be applied to calculate the position of the parts dropped on the plate. Thanks to the nature of time reversal effect, multiple parts dropped at the same time can be detected as well.

In chapter 5, using the piezoelectric stacks as actuator, it is also possible to create a pulse on the plate at a specific position. The time-reversal effect will be used again to prove this method be also used to generate an pulse. Because of the damping phenomena, it should be weighted in order to obtain a better result.

The piezoelectric actuator drive design is given in chapter 6. A self-oscillating class-D amplifier is proposed as the most appreciated solution. The complete modelling compares the first order and the second order configuration. It can also predict the stability criteria for the second order configuration, which provides a reference for the design. The theoretical harmonic analysis of the non-periodic Pulse Width Modulation (PWM) can help for the parameter selection of the output filter.

Chapter 7 shows the experimental results for different applications using the principle proposed in this study. A keyboard application demonstrates the impact position detection using piezoelectric actuators as sensors. The pulse creation experiment shows the effectiveness of the proposed method.

Finally, a conclusion of the thesis is given in chapter 8.

2 State of the art

Contents

In this chapter, three major subjects will be investigated. Firstly, the wave propagation theory will be discussed. It can serve to detect the impact source or objects on the plate. The inverse effect can also help to create specific waves according to the eigenmode superposition or time-reversal theory. Secondly, the equivalent circuit of piezoelectric actuator will be reviewed. A well defined model can better represent the characteristics of the piezoelectric actuators and its coupled system. Finally, different solutions for the piezoelectric actuation will be presented. A comparison will be made in oder to select the best possible solution for the application on the working plate.

2.1 Introduction

This study aims to improve the vibrating plate for the part feeders of assembly systems. Our current experimental system replaces electromagnetic vibrators by piezoelectric actuators and only eigenmodes have been used for the operations. As the piezoelectric actuator is a more advanced vibration source, non-eigenmode waves will also be interesting to provide more possible operations for the part feeder. Meanwhile, piezoelectric actuators can also be used as sensors, which gives the possibility to detect the parts position on the plate. In this chapter, the existing theory and methods will be investigated as references for our application.

A brief discussion about the model of piezoelectric actuator will be presented, which will help the modelling of the coupled mechanical system. The actuator used in our application requires about 150 V for the power supply. Because of the range of swept frequencies (from 100 to 20 kHz), the design of the driving circuit becomes a challenge. As a result, possible types of drives for piezoelectric actuators will be investigated at the end of this chapter.

2.2 Wave propagation

2.2.1 Waves

According to previous studies and existing theories [8], most waves created by piezoelectric actuators can be classified into two categories: Rayleigh waves and Lamb waves. These two types of waves can be both deduced from two dimensional wave equations of an elastic body.

The Rayleigh wave is a surface acoustic wave (SAW). It is one of the solutions of the two dimensional wave equations. The solution shows that the particles on the top of the surface (shown in Fig. 2.1) follow an elliptical motion and the amplitude attenuates exponentially in the vertical direction. According to the solution of Rayleigh characteristic equation, the phase velocity of the Rayleigh wave depends only on the value of the Poisson's ratio of the material [8].

The Lamb wave is another solution of the wave equations for a thin layer. It contains a series of symmetric and antisymmetric modes. Fig. 2.2 shows the zero order symmetric mode and the zero order antisymmetric mode of a thin layer. The phase velocity of each modes is a function of frequency and it varies with the frequency during the propagation.

2.2.2 Position detection using piezoelectric actuator

In most common part feeders, the position detection of parts is currently carried out using a camera and an image processing system. As the piezoelectric actuator-based system can move parts to specific places [90], it will be interesting if the position detection could be done with only piezoelectric devices in order to make the part feeder free of camera, which could reduce the complexity of the system and avoid problems caused by camera base system (lighting
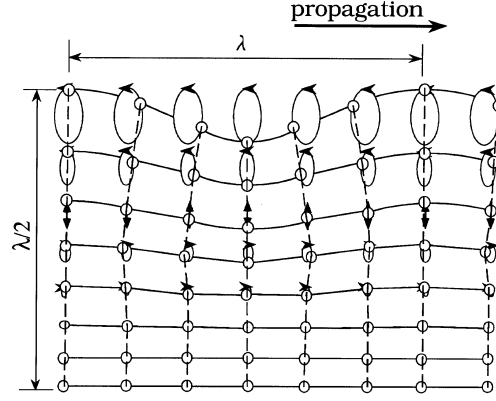
Figure 2.1 – Rayleigh wave in an elastic medium [59]

(a) Symmetric Lamb wave mode (S$_0$) (b) Antisymmetric Lamb wave mode (A$_0$)
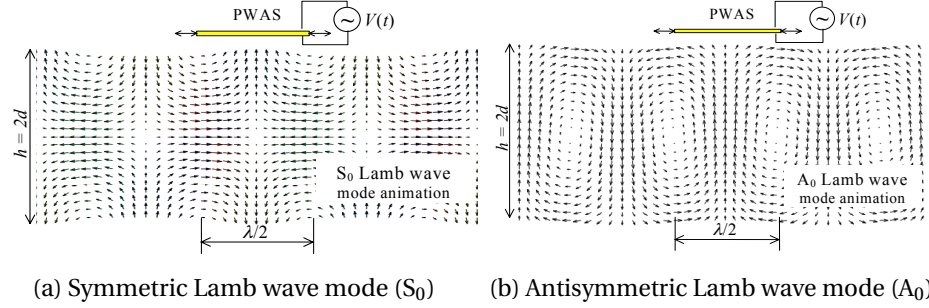
Figure 2.2 – Lamb wave modes detected by Piezoelectric Wafer Active Sensors (PWAS) [34]

problem, robot arm vision blocking problem). The position detection can be either active or passive. Through the active way, if a part is found on the working plate, a transducer can emit waves on the plate. The reflection of the waves due to the presence of the object can help determining its position. For passive waves, according to the common vibratory flexible part feeding system (as shown in Fig. 1.5), the parts drop on the working plate from a conveyor. From the contact point, acoustic waves will be emitted, which allows determining the source of the waves, thus the position of the part.

The active detection of objects on the surface of a plate normally uses Rayleigh wave. An early study employed single-phase array electrodes on a piezoelectric ZnO film to create surface waves on an aluminium single crystal block [40]. The generation and measurement of waves can also be made by bulk piezoelectric transducers. An example using such transducer with Poly-methyl methacrylate (PMMA) wedge is reported in [99] for the measurement of the acoustoelastic coefficients of a 316L stainless steel plate. The interdigital transducer (IDT) uses one pair of comb-like electrodes deposited on a piezoelectric substrate. Studies shows that it becomes more and more popular for creating surface acoustic waves [91][59]. Given an alternate voltage for the IDT, it will distort the substrate that can created Rayleigh wave.

Because the direction of propagation of Rayleigh wave can be well defined by the orientation of the electrodes, the position of a obstacle on the propagation path can be detected. This phenomenon has been used for a surface wave touch screen [86]. As shown in Fig. 2.3, two pairs of SAW transducers are placed at the corner of the screen for X and Y direction detection. The SAW mirrors are made on the edge of the screen with a 45° angle, which could let the travelling wave reflect and cover the whole surface. If an obstacle is on one path, its position can be determined depending on the travelling wave energy density and the delay detected by the receiver.
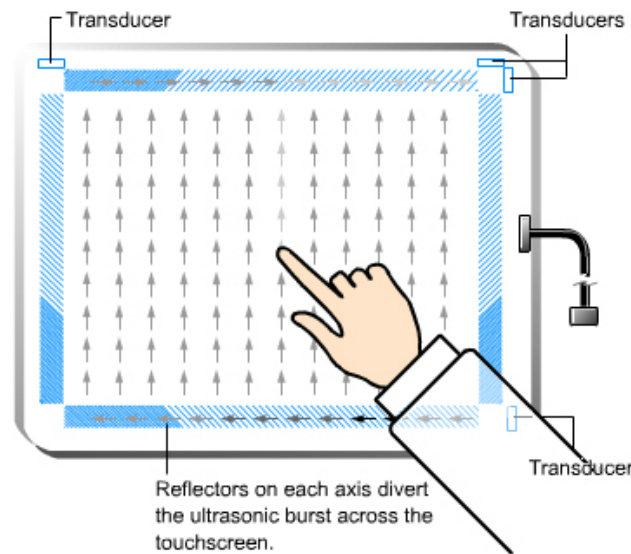
Figure 2.3 – Finger position detection using SAW (Rayleigh wave) [94]

For the passive detection, indeed, it is related to the acoustic emission source detection problem which is well studied in structure health monitoring. The objective of this field is mainly to find cracks inside the material [34]. In the case of pulse excitation, lamb waves are created and spread in all directions. Several methods based on signal temporal proprieties analysis can help find the acoustic emission source. The time-of-arrival (ToA) method is the most common one. As shown in Fig. 2.4, it measures the signal arrival time at at least three places and then the emission source position can be solved by their geometric relations [58]. Alternatively, it can be noticed that the acoustic emission wave contains two components: the asymmetric mode and the symmetric one. Their group velocities are slightly different from each other. According to the time-difference-of-arrival (TDoA) method, one can also calculate the acoustic emission source based on the difference of the arrival time of these waves[45][7]. Another method using time-reversal effect is reported in [29]. If the signal collected by the sensors can be resent in a time-reversal way, according to simulations, the position of maximum displacement on the plate is actually the position of the acoustic emission source. The advantage of this method is that it can detect more than one emission source simultaneously.
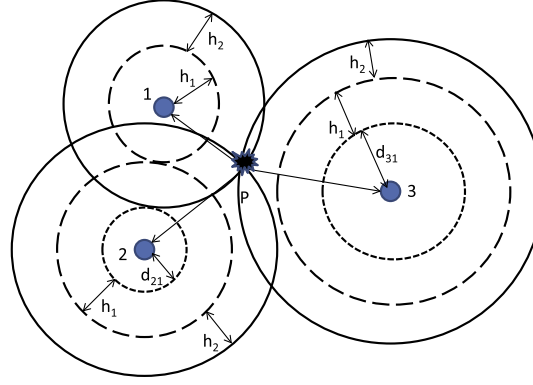
Figure 2.4 – Emission source detection using time-of-arrival method with three sensors [58]

According to the principle of ToA and TDoA methods, the lag detection is important to guarantee a good precision. One possible method is to compare the received signal with a referential elementary wave using the cross-correlation method [81]. This method extracts information of a given frequency from the original received signal. More complete analysis can also be done with other methods which transform the signal into time-frequency domain such as in [3], where the short-time Fourier transform has been used. In [38], the author chose the continuous wavelet transform for the analysis of the lag. The averaged frequency has been used to estimate the arrival time of the wave. The matching pursuit decomposition is a method which predefines a waveform dictionary based on Gabor functions [67] and can extract useful wave patterns from noise. It can be useful to separate overlapping multimodal reflections for when processing the wave signals [84]. The Hilbert-Huang transform is also reported in literature thanks to its advantage in varying frequency detection [95].

Small errors or noises will affect the precision of the position estimation. Some studies take into account the uncertainty of sensors and the system. The Extended Kalman Filter was discussed in the work of [73]. Statistical methods using Bayesian framework [30] and Gaussian process [41] have also been applied to estimate the distribution of the possible positions.

2.2.3 Wave creation

Despite the stationary waves, travelling waves or arbitrary waves are also interesting for the working plate to interact with the parts on it.

A metal bar is often used to study the one dimensional travelling wave in an elastic medium. The most intuitive solution is to put one actuator at one end of the bar to create waves and put another one at the other end to absorb the waves [39]. Due to the elliptical movement of the particle on the surface of the plate, objects can be moved to the opposite direction of the travelling wave. Miniaturisation has been reported thanks to the piezoelectric actuators [56]. The principle of creating travelling waves can also be the superposition of two standing

waves at the same frequency with 90° phase shift both in time and space domain [64][97]. However, it works only locally, because it does not exist eigenmodes which have the same eigenfrequency and the perfect phase shift everywhere on a bar. Another solution based on a ring-type structure has been proposed to solve this problem [42]. A well designed structure results in two orthogonal eigenmodes which can be used to create stable travelling waves, but the drawback is the bulky size of the structure.

The planar wave creation is similar to one dimensional waves. The basic concept is either to superpose two standing waves [93] or to absorb reflected waves [33]. As reported in [89], based on force distribution calculation, 32 actuators have been used to generate waves on a membrane. The time-reversal method can also be used to produce a pulse on a plate. Fig. 2.5 shows an example of creating a pulse excitation on a silicon wafer[31]. One transducer generates the original excitation. Another one detects the signal and records it. If the signal is replayed in a reversal way at the position of the second transducer, the original pulse excitation will be restored. In this way, the plate can interact with parts at a specific place on its surface.
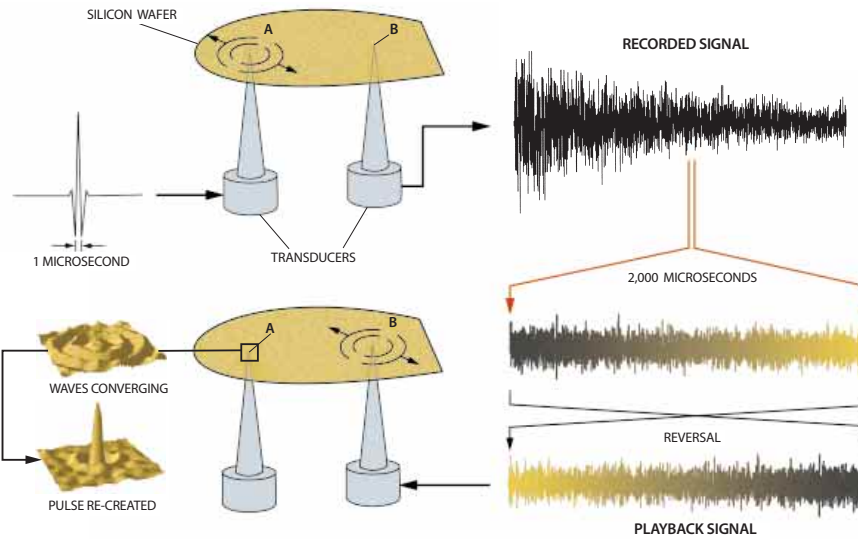
Figure 2.5 – Pulse creation using time-reversal method [31]

2.2.4 Comparison

The previous investigation shows the possible directions on how we can improve the working plate based on wave detection and wave generation using vibratory actuators. Summaries of these two subjects are given in Table 2.1 and Table 2.2. The major factors of different methods have been compared. The preferred ones are marked in green and the total score at the bottom is counted by the number of preferred factors.

The time-reversal method has the best score in both subjects. It requires minimum one bulk piezoelectric actuator and can complete multi-tasks. For the wave creation, although the only

Table 2.1 – Position detection comparison (Green: 1 point; yellow: 0.5 point)

Method	ToF	TDoF	Time-reversal	Reflector array
Wave type	Passive (Lamb wave)			Active (Rayleigh wave)
Actuator type	Bulk piezo-element			IDT
	Wedge transducer			Wedge transducer
Actuator number	≥3		≥ 1	≥ 4
Frequency	<100 kHz (Sensing)			>1 MHz (Emitter)
Multi-position detection	No		Yes	Yes
Special requirement	No		Simulation	Acoustic mirror
Score	3		3.5	2

Table 2.2 – Wave generation comparison (Green: 1 point; yellow: 0.5 point)

Method	Emitter-absorber	Eigenmodes superposition	Actuator matrix	Time-reversal
Wave type	Travelling wave			Pulse
Subtrate	Aluminium bar / rare for plate	Aluminium bar/plate	Membrane	Silicon plate
Actuator number	≥2	≥2	many	≥1
Available zone	Everywhere	Non homogeneous	Everywhere	Everywhere
Score	1.5	1	1	2

experiment was on a silicon plate, further studies can be carried out to adapt aluminium plate (material of the working plate).

2.3 Piezoelectric actuators

2.3.1 Piezoelectric effect

The piezoelectric effect is the electromechanical interaction between mechanical and electrical state in materials such as lead zirconate titanate (called PZT also). The direct effect corresponds to the internal generation of electrical charges resulting from an applied mechanical tensile or compressive forces (or stresses). Conversely, a mechanical strain appears when the ceramic is polarised by an external electrical field [88]. The constitutive equations to describe piezoelectricity are:

$$\mathbf{S} = \mathbf{s}^{\mathbf{E}}\mathbf{T} + \mathbf{d}^T\mathbf{E} \tag{2.1}$$

$$\mathbf{D} = \mathbf{d}\mathbf{T} + \epsilon^T\mathbf{E} \tag{2.2}$$

$$\tag{2.3}$$

where S is the strain vector, s^E is the elastic compliance matrix, T is the stress vector, d is the piezoelectric matrix, E is the electric field vector, D is the electric displacement field, ϵ is the permittivity[69].

2.3.2   Piezoelectric Ceramics

Two main kinds of piezoelectric ceramics are discussed in literature: the soft doped piezoelectric ceramics and the hard doped piezoelectric ceramics. Usually, the soft doped piezoelectric ceramics are suitable for sensing applications and low power transducers because of large piezoelectric constants and high relative permittivity. The hard doped piezoelectric ceramics are suitable for high power applications because of low dielectric constant, low mechanical losses and high electrical stresses[76].

2.3.3   Mono-layer and multi-layer

Mono-layer actuators are a single layer piezoelectric actuators made of bulk piezoelectric ceramics. Multi-layer piezoelectric actuators are composed of few piezoelectric layers for a total thickness of 2-3 mm. Single piezoelectric ceramics usually have low piezoelectric charge constants. To obtain a given electric field with the same total thickness of piezoelectric material, a mono-layer piezoelectric actuator needs a much higher voltage. Therefore, it needs a higher drive voltage to achieve the same displacement compared to multi-layer piezoelectric actuators.

2.3.4   Piezoelectric actuator equivalent circuit

The capacitance is a quantity dependent upon the material and its dimensions. As shown in Eq.2.4, the capacitance (in Farads) can be calculated by multiplying the relative dielectric constant ε_r by the permittivity of vacuum space ε_0 ($\varepsilon_0 = 8.9 \times 10^{-12}$ Fm^{-1}) and electrode surface area A, then divided by the thickness d separating the two electrodes.

$$C_p = \frac{\varepsilon_r \varepsilon_0 A}{d} \tag{2.4}$$

Piezoelectric actuators with many thin dielectric layers connected in parallel (multilayers) can have quite high capacitance [75]. Normally, manufacturers provide the capacitance as a reference. Meanwhile, it can also be determined using an impedance meter. By introducing a piezoelectric model, its electrical parameters can be better described.

According to the IEEE Standard on piezoelectricity [69], the impedance properties of unloaded piezoelectric ceramic near an isolated resonance can be represented by Van Dyke model [96] as shown in Fig. 2.6, where C_0 is the electrostatic capacitance, C_1, R_1 and L_1 are terms related to the self resonance. Indeed, the capacitor C_0 stands for its property in the non-resonant
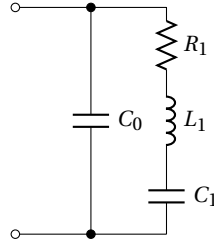
Figure 2.6 – Van Dyke model of an unloaded piezoelectric element

frequency range. The resonant frequency of a piezoelectric actuator itself is normally from several tens of kHz to hundreds of kHz. However, in practical applications, the actuator often works at a quite low frequency (below several kHz especially for mechanically coupled applications).

In certain cases, the simple C_0 parameter is not sufficient to model the piezoelectric actuator's behaviour which does not take into account the real part of its impedance. Several researches pointed out this problem and proposed a few equivalent circuits. Park introduced a frequency dependent resistor (in Fig. 2.7b) which follows a power-law function [77]. He found when it is in series with the capacitor C_0 the result fits well the measured data. Guan *et al.* proposed a circuit (in Fig. 2.7c) which combines the behaviour of the parallel model at low frequency and that of the series model at high frequency [37]. Later, Kim *et al.* mentioned a simplified model (in Fig. 2.7a) with a constant value resistor in series with the capacitor [54] but it only worked at a high frequency range (>10 kHz).

(a) Kim's model

(b) Park's model

(c) Guan's model
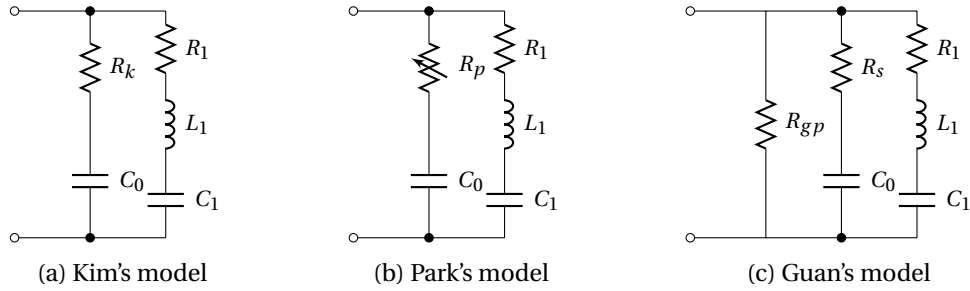
Figure 2.7 – Unloaded piezoelectric ceramic models

Within the resonant frequency range, there are several methods to fit the charateristic curve [96][57]. However, an accurate model inside the non-resonant frequency range is more interesting because the actuator works in a more stable way in this range and the resonance of the full system (piezoelectric actuators plus the dedicated mechanical part) is often present in this range.

In the mentioned articles, only models are proposed, but unfortunately, there is no discussion neither about the method to estimate the parameters nor on the quantitative comparison with

other methods. As a result, special attention should be paid when choosing the equivalent circuit of the piezoelectric actuator.

2.4 Drive

The piezoelectric actuator drive is the device which controls the movement of piezoelectric actuators. Different drives have been developed according to the type of the piezoelectric actuator such as bimorph actuators [52], multilayer actuators [63], mechanically amplified actuators [32][71]. In general, piezoelectric actuators require specific drive circuits with high-speed and high-voltage capabilities. These circuits can be implemented using voltage inverter, operational amplifiers [70] or bridge based inverter to meet specific requirements.

2.4.1 Voltage converter

Due to the nature of the piezoelectric actuator and in order to have a sufficient deformation, an important voltage is required from the power supply. The voltage converter can be used to solve this problem. The boost converter can achieve this task with a direct current (DC), low voltage power supply. Fig. 2.8a shows this circuit: The MOSFET S is used as a switch with a PWM control signal. Its "on" state ratio determines the ratio between input voltage V_{DC} and the output voltage for the piezoelectric actuator C.

Given an alternating current (AC) supply, the voltage multiplier can be used to have a more important voltage. But it requires an AC supply which varies between a negative value and a positive value. Supposing the minimal and the maximal voltages are $-V_{max}$ and V_{max}, thanks to the diodes which block negative current, the output voltage is equal to the number of stage times V_{max}. In the case of Fig. 2.8b, it has 4 stages, thus, one will find $4V_{max}$ at the output to supply the piezoelectric actuator.

The similar result can also be achieved by using a transformer. With a basic configuration, the input should be AC and the direct output is also AC with the same frequency as the input. One can also use a DC supply and a switch circuit (MOSFET for example) to replace the AC source so that the switching frequency can be variable according to the switch control. The output wave is normally sinusoidal while it is in resonance. If a DC output is required, a full-wave rectifier can be added to the second stage of the transformer.

Mixed solutions can also be found in articles. As shown in Fig. 2.9, the author combined a transformer and a boost converter to achieve a better voltage amplification and increase the power density [51]. In another work, the three methods above have been used to create the piezoelectric actuator drive in a small space [18].

The voltage converter can significantly amplify the voltage, however, if the load requires an important current, the power source should provide a extremely important current too, which makes this solution sometimes impossible to apply.

(a) boost converter

(b) Voltage multiplier
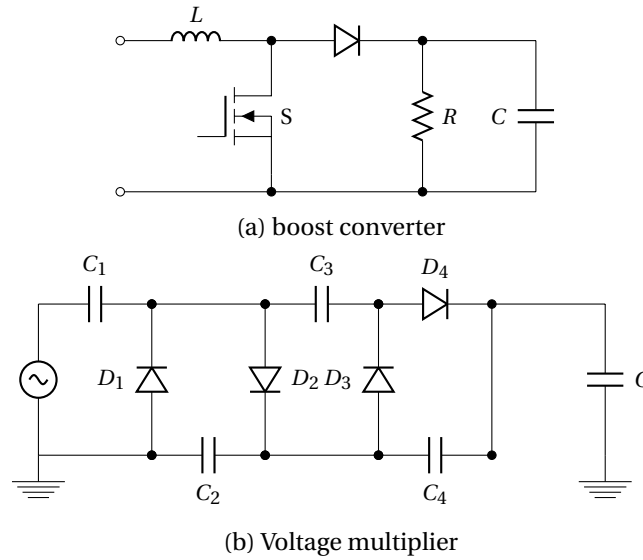
Figure 2.8 – Voltage converter circuits
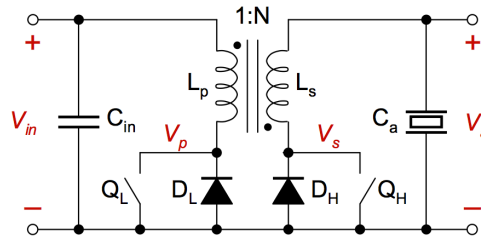
Figure 2.9 – Mixed converter with a transformer and a boost converter [51]

2.4.2 Amplifier drive (class-A/B)

The amplifier solution (class-A/B) is the simplest one because amplifiers are the easiest structures to integrate into an electrical circuit. Fig. 2.10 gives a typical schematic of an inverting amplifier drive [48]. The most commonly used implementation contains one or two amplifier stages. It depends on the bandwidth, the input source and output voltage requirements.

The advantages of amplifier-based solutions are the low signal distortion, good static performances, the high integration level, the simple structure and low electromagnetic interferences [72]. They can also adapt the synchronisation signal of our displacement measurement equipment. As a result, it is suitable for flexible tests. The amplifier and surrounded circuits are not complicated, but, a well designed cooling system is necessary due to the fact of driving a pure capacitive load. For example, the PA93 from APEX™ is a power amplifier which can fulfil the requirements for driving a piezoelectric actuator at above 150 V. It has a maximal power dissipation of 125 W while working at limit conditions [4]. A heat sink is necessary to guarantee the performance of the amplifier. Since the PA93 is of class-B [4], its theoretical
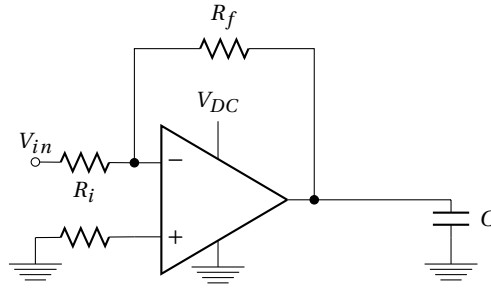
Figure 2.10 – Schematic of an amplifier drive

maximum power efficiency is 78.5% [92].

Otherwise, as the piezoelectric actuator is considered as a capacitive load, overshoot and oscillations may occur especially when using amplifier drives [13]. A number of considerations must be taken into account when selecting an appropriate circuit in order to keep the feedback system stable.

2.4.3 Bridge Drive

The bridge drive is an electronic circuit using transistors to convert DC to AC or DC. In order to obtain better performances around 150 V and a working frequency about several kHz, MOSFET is suitable for this application [12].

Fig. 2.11 shows the basic configuration of a half-bridge drive topology [48], the S_1 and S_2 are switches controlled by a PWM signal to generate square signals. The inductor and the piezoelectric load (C) constitute a second order filter, which can remove the high frequency components of the PWM. A hybrid bridge based converter is presented in [49]. A feedback system using a complex programmable logic device (CPLD) will take into account the voltage and the current of the load. Their drive could work at 200 V, 12 A and 500 Hz with an efficiency of 95%. However, due to the relative slow slew rate, it takes about 0.3 ms to climb up from 0 to 200 V. A half-bridge drive can only work in the positive range, while a H-bridge can work on both directions.

A more complicated configuration using a multi-level bridge is reported in [62]. The inverter topology in Fig. 2.13 consists of an hybrid three-level PWM inverter. The left leg of the inverter is composed of four MOSFETs (S_1 - S_4), supplied by a 105 kHz PWM, which is three times of the fundamental frequency. S5 and S6 of the right leg of the inverter operate only at the fundamental frequency. According to electrical simulations, a LLCC filter is added to the output of the bridge drive, which allows a working frequency range from 20 to 60 kHz [62].

An experimental inverter prototype of 1.5 kW power was built up to verify the operating principle. The output is 270 V (U_{Cp}) at a frequency of 35 kHz with a root mean square current

(RMS) of 4.2 A .

Kauczor *et al.* [53] discussed also the output filter design. A LC resonant filter, a LLCC resonant filter or a low-pass filter could be applied between the load and the drive. The corresponding schematics are presented in Fig. 2.12. The output transformer is needed to ensure an electrical insulation and the adjustment for the required level of the output voltage [53]. The LC filter is a second order band-pass filter whose resonant frequency is selected near the resonance frequency of the mechanical system of the transducer. The LLCC filter is a topology composed of two inductors, one capacitor and the piezoelectric load. The advantage of LLCC filters is that the system can work in a larger operating range around the system resonant frequency. The drawback is that high currents cause the inductors and the capacitors to be bulky, heavy and expensive. The PWM filter mentioned in Fig. 2.12 is a RC low-pass filter. Because the output of the H-bridge can be considered as a superposition of the harmonics and the fundamental, a RC low-pass filter could be applied by choosing properly the cutoff frequency. The last filter is mainly suitable for a higher frequency application. The proposed solution of [53] is valid for piezoelectric actuators with a high mechanical Q-factor (hard doped piezoelectric ceramics). It shows that the converter with a low-pass filter is the most suitable solution, because of its flexibility, dynamics and potential of miniaturisation.

2.4.4 Class-D amplifiers

The class-D amplifier is normally based on a half or full bridge converter which contains two or four transistors. The input signal, on/off for each transistor, is generated by the control logic. The output of the inverter is filtered by a low-pass filter and then applied to the piezoelectric actuator. The quality of the output signal depends on the method to modulate the input signal, the electrical characteristic of the circuit and the output circuit [1]. In order to generate the control signal, the most common way is to use a triangle wave carrier. By comparing the input signal level with the carrier, a fixed frequency PWM is generated and its duty cycle is thus equal to the ratio of the signal voltage level to triangle signal amplitude [20]. Σ-Δ Modulation is another possible way to generate the input signal [23]. The idea is to limit the integration of
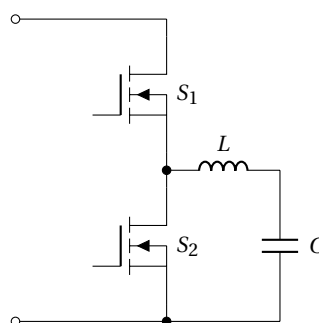
Figure 2.11 – Schematic of a half-bridge drive
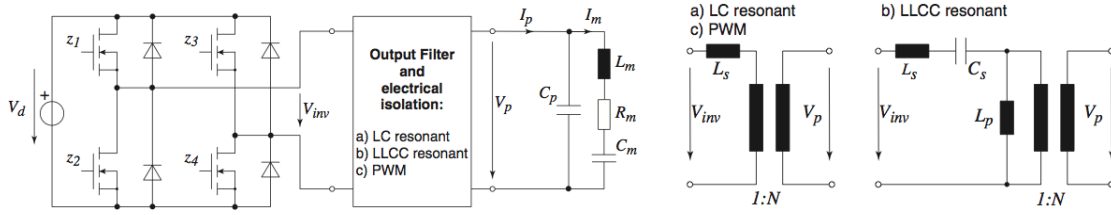
Figure 2.12 – Schematic of a H-bridge drive [53]
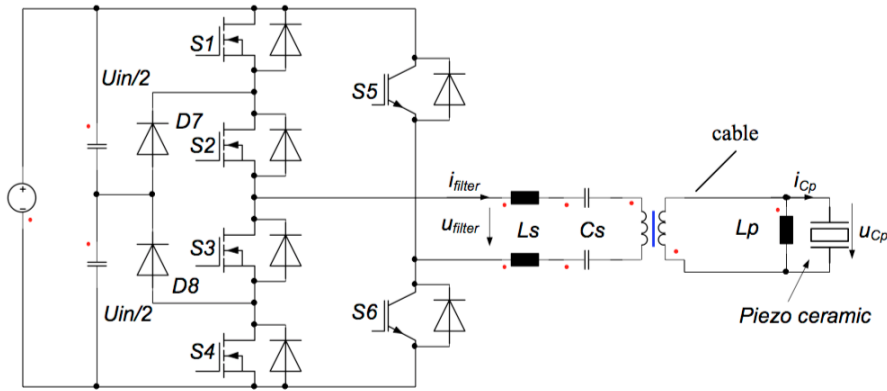
Figure 2.13 – Schematic of a three levels bridge drive [62]

the error between the output signal and the input signal. In case of open-loop, for high voltage and high frequency applications, important distortions appear because of the electric system properties such as the MOSFET response characteristic and the minimal pulse resolution. An example of such effect in a simulation can be found in [35]. For the objective of reducing distortions, closed-loop solutions are employed. Either current feedback or voltage feedback is possible [22][66].

In the class-D amplifier family, self-oscillating class-D amplifiers became a popular architecture frequently seen in audio amplifier designs [80][47]. It has some advantages compared to other configurations. On the one hand, because it avoids using a high precision triangle wave generator and a Σ-Δ modulator, it can reduce the complexity of the amplifier architecture. On the other hand, the variable frequency can solve the minimal pulse resolution problem when the signal is close to the maximal or the minimal values [82]. Furthermore, the self-oscillating class-D amplifier can be divided into two categories: hysteresis and delay based configurations [10]. Many articles about the audio self-oscillating class-D amplifier are destined for integrated circuit (IC) [79][60][65] where electric propagation delays are often ignored, thus, hysteretic design has been mainly applied. In contrary to their application, for high power and printed circuit board (PCB) based designs, the delay based configuration will be simpler and more interesting.

Table 2.3 – Driving technology comparison for piezoelectric actuator

	Power converter	Amplifier (class-A/B)	Bridge based converter			
			Other	Class-D		
				Periodic PWM	Software controled	Self-oscillating (Non periodic PWM)
Output power	Low	Low to medium	Low to high			
Output wave	Pulse/Sinusoidal	Arbitrary	Pulse/Sinusoidal	Arbitrary		
Frequency limits		Load capacity Output power		Components delay	Control unit timer Components delay	Components delay
Estimated Frequency range with 300uF load at 150 V	0 to 100 kHz	0 to 20 kHz	0 to 100 kHz	0 to 10 kHz	0 to 20 kHz	0 to 20 kHz
Complexity	Low	Low	Low	Low	High	Low

2.4.5   Comparison

In order to drive a capacitive load, the piezoelectric actuator drive can be built based on converter circuits, operational amplifiers or switching bridges.

- The converter allows to achieve a high voltage with a low power source, but the output current and output power are limited.

- The amplifier solution is a simple way to build a highly linear, low distortion drive and it works well with small signals generated by measurement equipments. Despite of the relative low efficiency, this is an ideal solution for piezoelectric tests and quick developments.

- The bridge drives have a high variety of topologies. In general, they are more efficient and cheaper than high power amplifier. They can work at a significant voltage range (up to 4 kV [25]). But the topology is more complicated, especially for the multi-level bridge drive and the filter design. The components should also be selected carefully in consideration of the high current and the high voltage.

Table 2.3 shows the comparison of the different driving methods. The red marks indicate the reasons why they are not suitable for our application compared to others. Finally, the amplifier and the self-oscillating class-D amplifier can be the candidates for our application. Nevertheless, due to the capacitive nature of the load, for an arbitrary signal, the system contains a lot of reactive power. The class-A/B amplifier should dissipate the power itself, while the class-D amplifier dissipates most of its power on the filter stage. As a result, the class-D amplifier is easier for the power dissipation design.

Relative publications to the chapter

- X. Liu, D. Shi, Y. Civet and Y. Perriard, "Modelling and optimal design of a ring-type structure for the generation of a traveling wave," *2013 International Conference on Electrical Machines and Systems (ICEMS)*, Busan, 2013, pp. 1286-1291.

3 System and modelling

Contents

This chapter focuses on the common theoretical aspects for both the wave detection and the wave creation. The plate motion equation is established according to the Kirchhoff's thin plate theory. Further development of the equation gives the response due to an excitation pulse. Damping ratios are also important parameters to be determined. An alternative method for its measurement is proposed, which is based on the piezoelectric actuator impedance measurement. Nevertheless, this method requires an accurate equivalent circuit of the piezoelectric actuator. New models are proposed and compared with other models by experiments. Finally, an application of the damping ratio measurement using the proposed method will be reported.

3.1 Introduction

The vibrating plate is the key element both for the wave detection and for the wave creation. They share several common points in the modelling. Thus the modelling of the vibrating plate will be presented in this chapter.

As damping effect cannot be ignored in practical applications, it is important to take it into account in the vibration equations. As the damping ratio varies with frequency, it is time consuming to measure the whole surface displacement for each eigenmode. However, the relation between the electric measurement of the piezoelectric actuator and the surface displacement can be established, providing an efficient and innovative method to deduce the damping ratio.

3.2 Vibration of a plate

The motion of a vibratory plate can be modelled by the Kirchhoff's plate theory [85]. The thickness of the plate is assumed to be small enough compared to the plate characteristic size and significant enough compared to the lateral deflection. Moreover, it consists of three assumptions:

i. Straight lines normal to the mid-surface remain straight after deformation

ii. The thickness of the plate does not experience elongation during deformation.

iii. Straight lines normal to the mid-surface rotate such a way that they remain normal to the mid-surface after deformation.

Considering a thin plate featuring uniform thickness h as shown in Fig. 3.1, in a Cartesian coordinate system, one can denote $\mathbf{u}(x, y, z) = (u_x, u_y, u_z)$ the displacement of a particle of the plate at position (x, y, z). Upon bending, the rotation angle is noted as θ_x for the x direction and θ_y for the y direction.
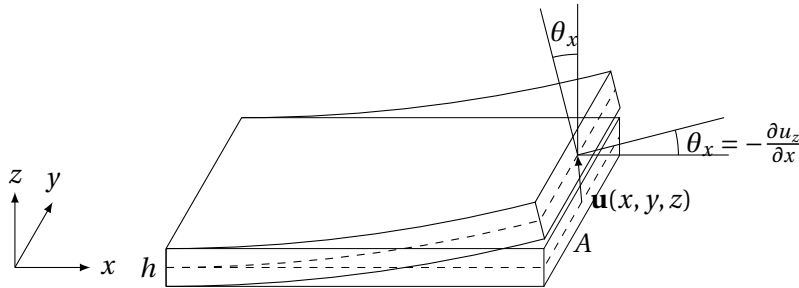
Figure 3.1 – Deformed thin plate which satisfies the Kirchhoff hypothesis

According to the Kirchhoff's plate assumptions, the rotation angles can be represented by

variation of the vertical displacement of the mid-surface as given in (3.1):

$$\theta_x = -\frac{\partial u_z}{\partial x}, \quad \theta_y = -\frac{\partial u_z}{\partial y} \tag{3.1}$$

Due to the small deflection, the rotation angle is also small. The particle displacement can then be obtained by approximated expressions. Because all the expressions depend on the vertical displacement, by convention, we denote $w(x, y)$ the vertical displacement of the mid-surface at the position (x, y). The displacement can then be expressed as in (3.2):

$$u_x \approx -z\theta_x = -z\frac{\partial u_z}{\partial x} = -z\frac{\partial w}{\partial x}, \quad u_y \approx -z\theta_y = -z\frac{\partial u_z}{\partial y} = -z\frac{\partial w}{\partial y}, \quad u_z = w(x, y) = w \tag{3.2}$$

The strains S associated with these displacements can be obtained from the elasticity equations:

$$
\begin{aligned}
S_{xx} &= \frac{\partial u_x}{\partial x} = -z\frac{\partial^2 w}{\partial x^2} \\
S_{yy} &= \frac{\partial u_y}{\partial y} = -z\frac{\partial^2 w}{\partial y^2} \\
S_{zz} &= \frac{\partial u_z}{\partial z} = \frac{\partial w}{\partial z} = 0 \\
2S_{xy} = 2S_{yx} &= \frac{\partial u_x}{\partial y} + \frac{\partial u_x}{\partial y} = -2z\frac{\partial^2 w}{\partial x \partial y} \\
2S_{yz} &= \frac{\partial u_y}{\partial z} + \frac{\partial u_z}{\partial y} = -\frac{\partial w}{\partial y} + \frac{\partial w}{\partial y} = 0 \\
2S_{zx} &= \frac{\partial u_z}{\partial x} + \frac{\partial u_x}{\partial z} = \frac{\partial w}{\partial x} - \frac{\partial w}{\partial x} = 0
\end{aligned}
\tag{3.3}
$$

In (3.3), all the strains having z components are zero. Only the components of xx, yy, xy and yx should be considered. Applying Hook's law for the thin plate, (3.4) shows the matrix form of plane stresses σ_{ij}. E_{ij} are Young's modulus.

$$
\begin{bmatrix} \sigma_{xx} \\ \sigma_{yy} \\ \sigma_{xy} \end{bmatrix} = \begin{bmatrix} E_{11} & E_{12} & E_{13} \\ E_{21} & E_{22} & E_{23} \\ E_{31} & E_{32} & E_{33} \end{bmatrix} \begin{bmatrix} S_x \\ S_y \\ 2S_{xy} \end{bmatrix} = -z \begin{bmatrix} E_{11} & E_{12} & E_{13} \\ E_{21} & E_{22} & E_{23} \\ E_{31} & E_{32} & E_{33} \end{bmatrix} \begin{bmatrix} \frac{\partial^2 w}{\partial x^2} \\ \frac{\partial^2 w}{\partial y^2} \\ 2\frac{\partial^2 w}{\partial x \partial y} \end{bmatrix} \tag{3.4}
$$

According to (3.4), the stress distribution is rotational symmetric with respect to the mid-surface as shown in Fig. 3.2a, which results in a moment on each surface of the small volume element.

Supposing each small volume element's size is $dx \times dy \times h$, the elementary moment M_{ij} can

(a) Normal stresses and shear stresses
(σ_{yx} not presented)

(b) Bending moments
(M_{yx} not presented)
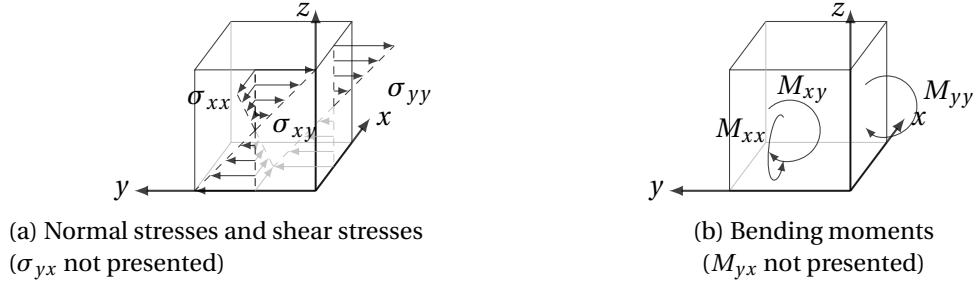
Figure 3.2 – Stress and bending moments illustration

be calculated by the integral over z: $M_{ij} = \int_{-\frac{h}{2}}^{\frac{h}{2}} -\sigma_{ij} dz$. Then we obtain:

$$
\begin{bmatrix} M_{xx} \\ M_{yy} \\ M_{xy} \end{bmatrix} = \frac{h^3}{12} \begin{bmatrix} E_{11} & E_{12} & E_{13} \\ E_{21} & E_{22} & E_{23} \\ E_{31} & E_{32} & E_{33} \end{bmatrix} \begin{bmatrix} \frac{\partial^2 w}{\partial x^2} \\ \frac{\partial^2 w}{\partial y^2} \\ 2\frac{\partial^2 w}{\partial x \partial y} \end{bmatrix}
\tag{3.5}
$$

For an isotropic material of elastic modulus E and Poisson's ratio ν, (3.5) becomes:

$$
\begin{bmatrix} M_{xx} \\ M_{yy} \\ M_{xy} \end{bmatrix} = D \begin{bmatrix} 1 & \nu & 0 \\ \nu & 1 & 0 \\ 0 & 0 & \frac{1}{2}(1-\nu) \end{bmatrix} \begin{bmatrix} \frac{\partial^2 w}{\partial x^2} \\ \frac{\partial^2 w}{\partial y^2} \\ 2\frac{\partial^2 w}{\partial x \partial y} \end{bmatrix}
\tag{3.6}
$$

where $D = \frac{1}{12}\frac{Eh^3}{1-\nu^2}$ which is the isotopic plate rigidity coefficient.

(a) Bending moments

(b) Shear forces on the surfaces
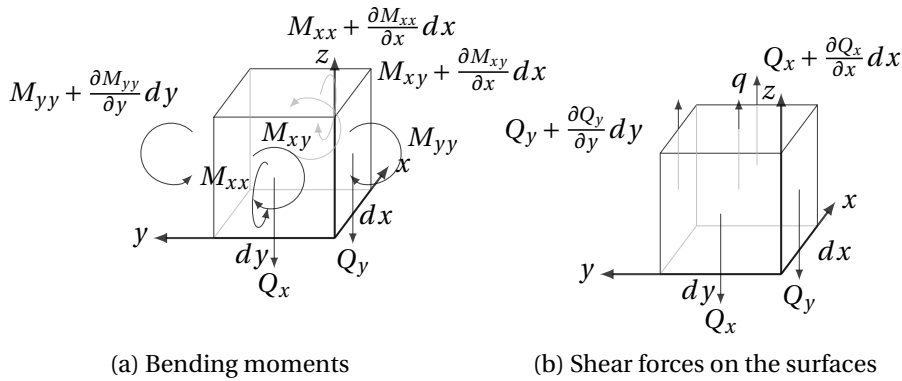
Figure 3.3 – Bending moments and shear forces on the surface of a small volume element

The shear forces (per unit length) on a small volume element are presented in Fig. 3.3b. The sum of Q in z direction is equal to the external force applied on it. Supposing that q is the force per unit area and applying the Newton's second law, the force equilibrium equation is

given in (3.7).

$$\frac{\partial Q_x}{\partial x} + \frac{\partial Q_y}{\partial y} + q = \rho h \frac{\partial w}{\partial t} \tag{3.7}$$

where ρ is the density of the material.

In order to calculate the shear force, one can use the moment equilibrium equation for a small volume element. As shown in Fig. 3.3a, for Q_y and Q_x, we have:

$$\frac{\partial M_{xx}}{\partial x} + \frac{\partial M_{yx}}{\partial y} = -Q_x, \quad \frac{\partial M_{xy}}{\partial x} + \frac{\partial M_{yy}}{\partial y} = -Q_y \tag{3.8}$$

Knowing that $M_{xy} = M_{yx}$ and taking (3.8) into (3.7), it can be obtained:

$$\frac{\partial^2 M_{xx}}{\partial x^2} + 2\frac{\partial M_{xy}}{\partial y \partial x} + \frac{\partial^2 M_{yy}}{\partial y^2} + \rho h \frac{\partial w}{\partial t} = q \tag{3.9}$$

According to (3.6), the moments can be replaced by functions of w. The final motion equation of a vibratory plate is obtained:

$$D\nabla^2\nabla^2 w + \rho h \frac{\partial^2 w}{\partial t^2} = q \tag{3.10}$$

where $\nabla^2\nabla^2$ is an operator defined as $\nabla^2\nabla^2 = \frac{\partial^4}{\partial x^4} + 2\frac{\partial^4}{\partial x^2 \partial y^2} + \frac{\partial^4}{\partial y^4}$.

3.3 Vibration created by an excitation pulse

Supposing a pulse force is applied at a point A on a thin plate as shown in Fig. 3.4, and point X being the position where the vibration is observed. It would be interesting to predict the vibration through the calculation.
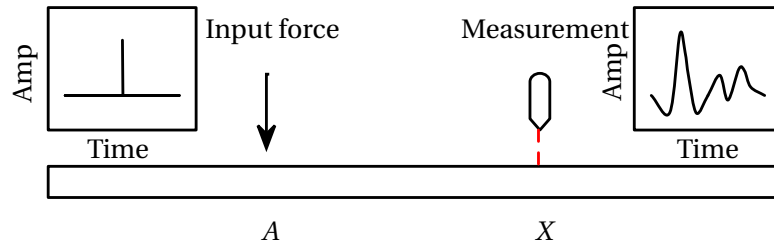
Figure 3.4 – Excitation at point A and detection at point X

According to the motion equation (3.10), one can replace q by a time-position dependent

29

function to adapt this case:

$$(D\nabla^2\nabla^2 + \rho h\frac{\partial^2}{\partial t^2})w(x,y,t) = F(x,y,t) \tag{3.11}$$

where $w(x,y,t)$ is the displacement at position (x,y) and at instant t, $F(x,y,t)$ is an excitation force function. As $F(x,y,t)$ is a pulse excitation, then it can be written in the form of $F(x,y,t) = \rho h F\delta(x-A_x)\delta(y-A_y)\delta(t)$, where F is a constant function and δ is a Dirac function.

In order to find a solution, we suppose $w(x,y,t)$ can be represented by the sum of separated variables as in (3.12):

$$w(x,y,t) = \sum_n \phi_n(t)\psi_n(x,y) \tag{3.12}$$

where $\phi_n(t)$ are the time-only dependent components. $\psi_n(x,y)$ are the spatial orthogonal eigenmodes of the plate which satisfy

$$\nabla^2\nabla^2\psi_n = \omega_n^2 \frac{\rho h}{D}\psi_n \tag{3.13}$$

where ω_n are the eigenfrequencies. Taking (3.12) and (3.13) into (3.11), it can be obtained:

$$\sum_n \rho h\psi_n(x,y)(\frac{\partial^2}{\partial t^2}\phi_n(t) + \omega_n^2\phi_n(t)) = \rho h F\delta(x-A_x)\delta(y-A_y)\delta(t) \tag{3.14}$$

For each $m \in \mathbb{Z}^+$, if we multiply by ψ_m on both side of the equation and calculate the integral on the spatial field, equation (3.14) becomes:

$$\iint \psi_m(x,y)\sum_n \psi_n(x,y)(\frac{\partial^2}{\partial t^2}\phi_n(t) + \omega_n^2\phi_n(t))dxdy = \iint \psi_m(x,y)\delta(x-A_x)\delta(y-A_y)F\delta(t)dxdy \tag{3.15}$$

As the ψ_n and ψ_m are orthogonal, we have $\iint \psi_m\psi_n dxdy = \delta_{mn}$ and $\iint \psi_m\delta(x-A)\delta(y-A_y)dxdy = \psi_m(A_x,A_y) = \psi_m(\mathbf{A})$. As a result, according to (3.15), for each $\phi_m(t)$, we can obtain its second order differential equation:

$$\frac{\partial^2}{\partial t^2}\phi_m(t) + \omega_m^2\phi_m(t) = F\psi_m(\mathbf{A})\delta(t) \tag{3.16}$$

The general solution of (3.16) is as follows:

$$\phi_m(t) = A(t)e^{i\omega_m t} + B(t)e^{-i\omega_m t} + Ce^{i\omega_m t} + De^{-i\omega_m t} \tag{3.17}$$

where $A(t)$ and $B(t)$ correspond to its particular solution. They are easy to be obtained with

the help of its Wronskian, thus:

$$A(t) = \frac{F\psi_m(\mathbf{A})}{2i\omega_m} H(t) \tag{3.18}$$

$$B(t) = -\frac{F\psi_m(\mathbf{A})}{2i\omega_m} H(t) \tag{3.19}$$

where $H(t)$ is the unit step function. Because the system is causal, $\psi_m(t)$ should be zero for all $t < 0$. Bringing (3.18) and (3.19) to (3.17), thus C and D should be zero to satisfy this condition. Finally, we obtain the following solution:

$$\phi_m(t) = \frac{F\psi_m(\mathbf{A})}{\omega_m} \sin(\omega_m t) H(t) \tag{3.20}$$

Taking the damping ratio ζ_m into consideration and supposing it is much smaller than one, then we can suppose the amplitude of the vibration decreases exponentially. Equation (3.20) can be rewritten as:

$$\phi_m(t) = \frac{F\psi_m(\mathbf{A})}{\omega_m} \sin(\omega_m t) e^{-\zeta_m \omega_m t} H(t) \tag{3.21}$$

The displacement at point $\mathbf{X}(x, y)$ due to an unity excitation pulse ($F = 1$) can be written as:

$$w_A(\mathbf{X}, t) = \sum_n \frac{\psi_n(\mathbf{A})\psi_n(\mathbf{X})}{\omega_n} \sin(\omega_n t) e^{-\zeta_n \omega_n t} H(t) \tag{3.22}$$

3.4 Damping ratio

The damping ratio is an important parameter for vibratory systems. It determines the duration and characteristics of a free vibration. According to [55], the quality factor Q (and the damping ratio ζ) can be determined by the displacement curve with the half-power bandwidth.
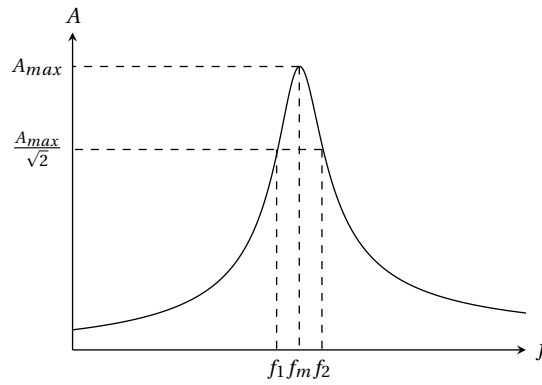
Figure 3.5 – Displacement curve

As shown in Fig. 3.5, supposing f_1 and f_2 are the frequencies where the vibration amplitude is 3 dB lower than the maximum amplitude ($\frac{A_{max}}{\sqrt{2}}$) and f_m is the frequency for maximum amplitude. The formula for the damping ratio is:

$$\zeta = \frac{1}{2Q} = \frac{f_2 - f_1}{2f_m} \tag{3.23}$$

Because the damping ratio is frequency-dependent, measurements should be carried out for each eigenmode. Traditional measurements can be performed by a direct displacement measurement of the plate surface, for example, with a laser doppler vibrometer. The disadvantage is that for each mode, it is necessary to relocate the measurement position on the plate, because the amplitude of vibration is maximal only at antinodes. The antinode position for one eigenmode could be a node for another eigenmode, where the amplitude is nearly zero. As a result, it will be interesting to obtain all damping ratios when performing a single measurement.

The modelling of the piezoelectrically actuated system shows that the relation between the impedance of the actuator and the vibration amplitude can be established. It allows to make only the impedance measurement instead of displacement measurements to calculate the damping ratio.

3.4.1 Power aspect modelling

A piezoelectrically actuated system electric equivalent circuit can be divided into a part representing piezoelectrical ceramic and a part representing the coupled mechanical system. The modelling of the two parts is necessary for the study of the power aspects. Applying the principle of the conservation of energy, the relation between piezoelectric equivalent circuit parameters and mechanical parameters can be obtained, which will lead to the relation between the impedance of the actuator and the displacement of the plate.

(a) Unmounted piezoelectric actuator

(b) Mounted piezoelectric actuator with coupled mechanical part
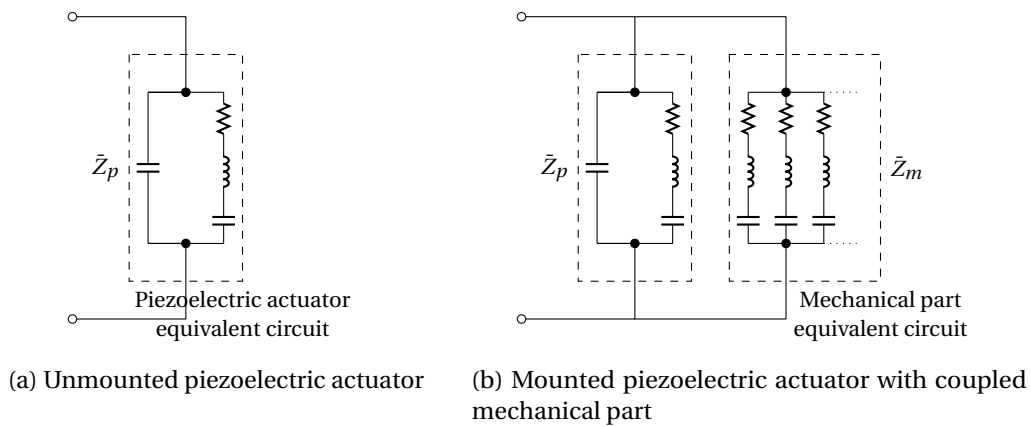
Figure 3.6 – Equivalent circuit for unmounted and mounted actuator

Supposing the power supply condition U is unchanged, in the free piezo (unmounted) case (Fig. 3.6a), the electrical power represents the power consumption of the actuator itself. When attached to the mechanical part, the electric power represents the total power consumption of both parts (Fig. 3.6b). Supposing the influence of the change of thermal conditions and deformation are negligible, the power consumption of the actuator is identical in both cases, and thus the power difference between the two cases is the power transferred to the mechanical part.

In the mounted case, we note $\bar{Z}_t$ as the total impedance of the load, thus $\bar{Z}_t = \bar{Z}_p \parallel \bar{Z}_m$. The power transferred to the mechanical part is:

$$P_t = \frac{1}{2}\left(\left|\frac{\hat{U}}{\bar{Z}_t}\right|^2 \Re(\bar{Z}_t) - \left|\frac{\hat{U}}{\bar{Z}_p}\right|^2 \Re(\bar{Z}_p)\right) \tag{3.24}$$

The piezoelectric actuator is powered by a sinusoidal signal. We suppose that the actuator can give a deformation proportionnal to the supply voltage, which means it can generate a perfect sinusoidal excitation for the mechanical part. When the system enters in steady state, the structure follows a sinusoidal vibration as well. The power consumption of the mechanical part is only due to the dissipation of energy within the material. By introducing the quality factor Q or the damping ratio ζ [36], this dissipation can be expressed as in (3.25):

$$P_d = \frac{2\pi f}{Q}E_t = 4\pi \zeta f E_t \tag{3.25}$$

where E_t is the total energy due to vibration.

According to the conservation of energy of the system, the power transferred to the mechanical part is equal to this dissipated power. Thus, (3.24) is equal to the (3.25). Then we have:

$$\frac{1}{2}\left(\left|\frac{\hat{U}}{\bar{Z}_t}\right|^2 \Re(\bar{Z}_t) - \left|\frac{\hat{U}}{\bar{Z}_p}\right|^2 \Re(\bar{Z}_p)\right) = 4\pi \zeta f E_t \tag{3.26}$$

3.4.2 Piezoelectric actuator

In order to develop the right part of the (3.25), the first task is to measure the piezoelectric actuator's impedance when unmounted. Then, we will compare it to the after-mounted measurement data.

Because the actuator has a relative large capacitance, its reactance value is much greater than its resistance value. The equivalent resistance measurement results are very sensitive to the noise. That is one of the reasons we prefer to choose a model to get a smooth curve to describe its property. Another reason is to avoid recording many redundant data. The detail of the modelling of the piezoelectric actuator will be presented in Section 3.5.

When observing the measured impedance values, in both mounted and unmounted cases, the imaginary part of impedance is much larger than their real part. Furthermore, their imaginary parts share nearly the same value. If we accept the hypothesis that $|\bar{Z}_t| \approx |\bar{Z}_p|$, equation (3.24) can be rewritten as:

$$P_t = \frac{1}{2} \left| \frac{\hat{U}}{\bar{Z}_t} \right|^2 (\Re(\bar{Z}_t) - \Re(\bar{Z}_p)) \tag{3.27}$$

In (3.27), the $\Re(\bar{Z}_t)$ becomes the only parameter that we need to determine.

3.4.3 Plate vibration amplitude

The piezoelectric actuators are used to excited the eigenmodes of the plate. According to (3.10), natural vibration modes of the plate are governed by the (3.28):

$$D\nabla^2\nabla^2 w + \rho h \frac{\partial^2 w}{\partial t^2} = 0 \tag{3.28}$$

The mode shape solution for one mode is given in the form of (3.29)

$$w(x, y) = \phi_n(t)\psi_n(x, y) = A\sin(\omega_n t + \beta_n)\psi_n(x, y) \tag{3.29}$$

where A is a constant for the amplitude of mode n. $\psi_n(x, y)$ is the midsurface displacement related to mode n.

Taking (3.29) into (3.2), we can obtain the displacement function of the particles of the plate at (x, y, z):

$$\mathbf{u}(x, y, z, t) = \begin{bmatrix} -z\frac{\partial w(x,y)}{\partial x} \\ -z\frac{\partial w(x,y)}{\partial y} \\ w(x, y) \end{bmatrix} = \phi_n(t) \begin{bmatrix} -z\frac{\partial \psi_n(x,y)}{\partial x} \\ -z\frac{\partial \psi_n(x,y)}{\partial y} \\ \psi_n(x, y) \end{bmatrix} \tag{3.30}$$

The velocity of each point can be represented by the following equation:

$$\mathbf{v}(x, y, z, t) = \frac{\partial \mathbf{u}(x, y, z, t)}{\partial t} = \frac{d\phi_n(t)}{dt} \begin{bmatrix} -z\frac{\partial \psi_n(x,y)}{\partial x} \\ -z\frac{\partial \psi_n(x,y)}{\partial y} \\ \psi_n(x, y) \end{bmatrix} = A\omega_n \cos(\omega_n t + \beta_n) \begin{bmatrix} -z\frac{\partial \psi_n(x,y)}{\partial x} \\ -z\frac{\partial \psi_n(x,y)}{\partial y} \\ \psi_n(x, y) \end{bmatrix} \tag{3.31}$$

The energy density depends on the potential and kinetic energy of each particle in the structure. Considering the non-deformed instant t_{nd}, similar to a spring, all the potential energy

transforms into kinetic energy. The energy density expression can be written as follows:

$$\varepsilon(x, y, z) = \frac{1}{2}\rho \mathbf{v}^2(x, y, z, t = t_{nd})$$ (3.32)

The total energy of the vibratory plate of an eigenmode is:

$$E_t = \iiint_{V_{plate}} \varepsilon(x, y, z)dxdydz = 2\rho\pi^2 f_n^2 A^2 \Psi_n$$ (3.33)

where $\Psi_n = \iiint_{V_{plate}} ((z\frac{\partial \psi_n(x,y)}{\partial x})^2 + (z\frac{\partial \psi_n(x,y)}{\partial y})^2 + \psi_n^2(x, y))dxdydz$ which depends only on the plate geometry. Thus, it is constant for each mode. Its exact value can be determined either by simulation or by experiments.

As the total energy is known, (3.25) can be used to calculate the dissipated power:

$$P_d = \frac{4\pi^3 \rho f_n^3 A^2 \Psi_n}{Q} = 8\pi^3 \rho\zeta f_n^3 A^2 \Psi_n$$ (3.34)

The developments for our specific application have been given and the rest is to combine them together via the conservation condition. Replacing (3.26) by (3.27) and (3.34), we can obtaine:

$$A = \left|\frac{\hat{U}}{\bar{Z}_t}\right| \sqrt{\frac{\Re(\bar{Z}_t) - \Re(\bar{Z}_p)}{16\pi^3 \rho\zeta f_n^3 \Psi_n}}$$ (3.35)

For one eigenmode, the damping ratio ζ and the eigenmode depending variable Ψ_n can be considered unchanged within a small interval. If the supply voltage amplitude is constant, it is easy to conclude that the square of vibration amplitude A^2 is proportional to $\Re(\bar{Z}_t) - \Re(\bar{Z}_p)$. According to the condition of (3.23), the frequencies f_1 and f_2 can be found while $\Re(\bar{Z}_t) - \Re(\bar{Z}_p)$ becomes half of its maximum value. Then, the damping ratio and the quality factor can be easily deduced.

Furthermore, if all the parameters are determined, the amplitude can then be predicted only by the knowing input voltage $\hat{U}$.

3.5 Piezoelectric actuator modelling

The amplitude expression obtained in the previous section requires to know the real part of $\bar{Z}_p$ for the calculation. The direct measurement in a large frequency range will contain a big data set and interpolation may be used to make it usable at any frequencies. Furthermore the measurement noise will also affect the accuracy if we pick up only one single measurement point at a time. Therefore, a piezoelectric actuator model can help to represent its value more

accurately, reduce the required memory space and calculation resources.

The coupled mechanical part resonance occurs in a low frequency range and the piezoelectric actuator's resonance occurs at a relative high frequency range. As a result, we are mainly interested in finding a more accurate model of the piezoelectric actuator among the non-resonant frequency range.

3.5.1 Parameters regression method

The parameters of an equivalent circuit can be determined by impedance analysis and the most common way is to study the magnitude-phase diagram. However, in non-resonant frequency range, noticing that a piezoelectric element is almost equivalent to a capacitor, the magnitude of impedance depends mainly on its imaginary part, but the real part is more useful for the vibration amplitude calculation. Supposing the equivalent circuit of non-resonant part takes the form of (3.36) whose resistance and reactance are independent with each other, one can study its real part and imaginary part respectively.

$$\bar{Z}(\omega, \mathbf{k}) = R(\omega, \mathbf{k}) + jX(\omega, \mathbf{k}) \tag{3.36}$$

where $\bar{Z}$ is the impedance, R is the resistance, X is the reactance, ω is the angular frequency and $\mathbf{k} = \{k_1, ..., k_q\}$ is a vector of parameters not depending on the frequency.

Supposing vector $\mathbf{R_m}$ and vector $\mathbf{X_m}$ are measured data of dimension $n \times 1$ at frequencies $\boldsymbol{\omega_m}$, the objective is to find a parametric function in ω and $k_1, ..., k_q$ which fits the data by the means of the least-square roots method. Then the problem for finding the resistance can be written as in (3.37) where a function written in bold letter $\mathbf{F}(\boldsymbol{\omega_m}, \mathbf{k})$ is defined as a vector function $[F(\omega_{m,1}, \mathbf{k})...F(\omega_{m,n}, \mathbf{k})]^T$ and $\mathbf{F}$ here could be replaced by $\mathbf{R}$, $\mathbf{X}$ or other functions depending on the context. The coefficients k_j for the function $R(\omega, \mathbf{k})$ (named $R(\omega)$ later) can be obtained by solving the system of equations formed by partial derivatives of (3.37). For the imaginary part, as it is usually equivalent to a capacitor, we can use a standard method to find its value [96].

$$\underset{k_1, ..., k_q}{\arg\min} (\mathbf{R_m} - \mathbf{R}(\boldsymbol{\omega_m}))^T (\mathbf{R_m} - \mathbf{R}(\boldsymbol{\omega_m})) \tag{3.37}$$

3.5.2 Novel piezoelectric actuator models

This section will introduce two new equivalent circuits in order find a best model to represent the piezoelectric actuator. Including the models mentioned in the state of the art (Section 2.3.4), all these equivalent models will be examined in the next subsection.

Park's model (Fig. 2.7b) used a power-law function. According to his experimental results [77], k_p is around -1, therefore, it can be naturally found to use an inversely proportional function in order to simplify the expression. Thus, one of the proposed equivalent models can

(a) Inversely proportional to frequency model of an unloaded piezoelectric element

(b) Inversely proportional to frequency model with a resistor in series of an unloaded piezoelectric element
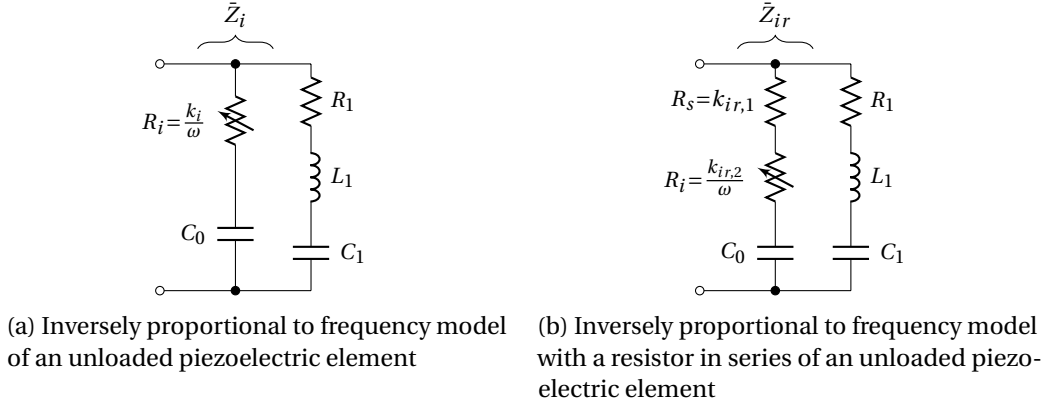
Figure 3.7 – Proposed unloaded piezoelectric ceramic models

be described by (3.38). The corresponding circuit is given in Fig. 3.7a.

$$\bar{Z}_i(\omega) = \frac{k_i}{\omega} - j\frac{1}{\omega C_0} \tag{3.38}$$

As we are mostly interested in the real part, the value of k_i should be evaluated. Applying the least-squares method given in (3.37), k_i can be expressed in (3.39).

$$k_i = \frac{\mathbf{R_m}^T \boldsymbol{\omega_m}^{\{-1\}}}{\boldsymbol{\omega_m}^{\{-1\}^T} \boldsymbol{\omega_m}^{\{-1\}}} \tag{3.39}$$

where $\boldsymbol{\omega}^{\{x\}} = [\omega_1^x ... \omega_n^x]^T$.

According to the concept of Guan's model and Kim's model, a small resistor can be added to the initial equivalent circuit to correctly represent the piezo within a high frequency range. By applying the same principle, the model in Fig. 3.7a can then be extended to Fig. 3.7b. Thus, the real part model becomes:

$$R_{ir}(\omega) = k_{ir,1} + \frac{k_{ir,2}}{\omega} \tag{3.40}$$

The parameter expressions are given in (3.41).

$$k_{ir,2} = \frac{\mathbf{V}_1^T \mathbf{R_m} \mathbf{V}_1^T \boldsymbol{\omega_m}^{\{-1\}} - n\mathbf{R_m}^T \boldsymbol{\omega_m}^{\{-1\}}}{\mathbf{V}_1^T \boldsymbol{\omega_m}^{\{-1\}} \mathbf{V}_1^T \boldsymbol{\omega_m}^{\{-1\}} - n\boldsymbol{\omega_m}^{\{-1\}^T} \boldsymbol{\omega_m}^{\{-1\}}} \tag{3.41a}$$

$$k_{ir,1} = \frac{\mathbf{V}_1^T \mathbf{R_m} - k_{ir,2}\mathbf{V}_1^T \boldsymbol{\omega_m}^{\{-1\}}}{n} \tag{3.41b}$$

where $\mathbf{V}_1 = [1 ... 1]^T$ is a vector of n constant elements.

3.6 Experimental results and discussion

3.6.1 Unmounted piezoelectric actuator measurements

Experiments have been carried out by measuring a commercial multilayer piezoelectric actuator (NAC2025 from Noliac) with an impedance analyser (Agilent 4294A). As its unloaded resonant frequency is above 250 kHz and in order to study its behaviour within a non-resonant frequency range, the measurement data are collected by sweeping the frequency from 100 Hz to 30 kHz with 4005 samples. On the instrument, the "resistance-reactance" mode was used and the equivalent capacitance could be quickly obtained and lead to $C_0 = 74.3$ nF. We will then focus on the real part.

Table 3.1 – Parameters of each model after regression using least-squares method applied on the first piezo sample. The expressions R as a function of parameters k for different models are given in Appendix A.

Model	Expression	Parameters	Equation	Value
Kim	$R_k = k_k$	k_k	(A.2)	1.21
Park	$R_p = k_{p,1}\omega^{k_{p,2}}$	$k_{p,1}$	(A.5b)	6.48×10^4
		$k_{p,2}$	(A.5a)	-1.08
	$R_{pl} = k_{pl,1}\omega^{k_{pl,2}}$	$k_{pl,1}$	(A.7)	1.22×10^4
		$k_{pl,2}$	(A.7)	-0.91
Guan	$R_g = k_{g,1}(1+\frac{k_{g,2}}{\omega^2})$	$k_{g,1}$	(A.12b)	0.8545
		$k_{g,2}$	(A.12a)	3.9×10^7
Inverse 1	$R_i = \frac{k_i}{\omega}$	k_i	(3.39)	3.60×10^4
Inverse 2	$R_{ir} = k_{ir,1} + \frac{k_{ir,2}}{\omega}$	$k_{ir,1}$	(3.41b)	-0.09
		$k_{ir,2}$	(3.41a)	3.62×10^4

Applying the formulas of different equivalent models introduced in Section 3.5 and in Appendix A, the parameters can be calculated using measurement data. Table 3.1 shows the resulting parameters values. For the Park's model, two methods have been adopted: an approximative method (noted Park log, with index pl) and an exact method (with index p). The latter does not have an explicit solution and should be solved numerically. The $k_{p,1}$ is about five times greater than $k_{pl,1}$. For the two proposed inversely proportional models, we find a very close value for both inversely proportional coefficient. However, in the model with a resistor in series, a negative resistance is found. Fortunately, its value is very small and nearly negligible, meaning it is not necessary to add a supplementary resistor in the equivalent model.

The regression curves are plotted in Fig. 3.8. For readability reason, curves are respectively zoomed in the low frequency range (0 to 2 kHz, head part) and in the high frequency range (18 to 20 kHz, tail part). Results shows that the Park's model and inversely proportional models fit better the measurement data. The comparison of its error and variance is given in Table

3.2. The experiment is also repeated for a second identical actuator in order to compare the reliability of these methods and different samples do not change too much the models' results. From the analysis of variance, the Park's model fits better the measured data, but it depends on how to estimate the parameters: if we transform it into a linear regression problem, it has almost the same performance as Guan's model. With the confirmation of previous result analysis, the two inversely proportional models have nearly the identical performance according to the results indicated in Table 3.2.

Table 3.2 – Comparison of error and variance of each model

Model	Sample	Variance	Error max	Error min	R^2
Kim	1st	12.42	1.14	-63.5	0
	2nd	12.01	1.09	-68.0	0
Park	1st	0.083	3.57	-3.13	0.993
	2nd	0.083	3.36	-8.05	0.992
Park log	1st	1.64	2.03	-28.9	0.865
	2nd	1.83	1.72	-35.2	0.846
Guan	1st	1.89	20.7	-9.66	0.848
	2nd	1.72	17.97	-10.11	0.857
Inverse 1	1st	0.15	4.1	-7.46	0.985
	2nd	0.17	4.08	-12.84	0.986
Inverse 2	1st	0.15	4.08	-7.09	0.988
	2nd	0.17	4.06	-12.4	0.986

The sensitivity analysis is used to study the coefficient variation with regard to the variation of measurement data set. In this case, two data set are applied: the low frequency range measurement data set (from 100 Hz to 10 kHz) and the high frequency range data set (from 10 kHz to 20 kHz).

(a) Head part

(b) Tail part
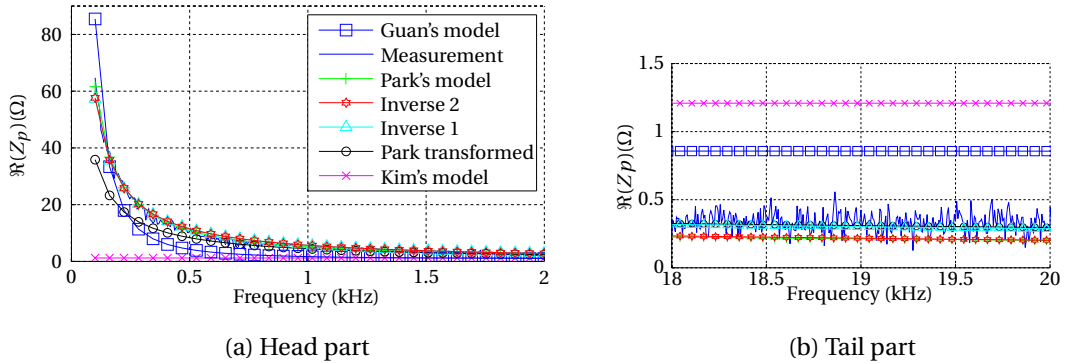
Figure 3.8 – Regression results of the models

Table 3.3 – Model sensitivity with reduced data sets of different frequency ranges

Model	Parameters	With low f set	Diff %	With high f set	Diff %
Kim	k_k	2.49	106%	0.38	-69%
Park	$k_{p,1}$	6.96×10^4	7.4%	290	-99.6%
	$k_{p,2}$	-1.09	0.93%	-0.58	-46%
	$k_{pl,1}$	4.2×10^4	-35%	139	-99%
	$k_{pl,2}$	-1.03	13%	-0.52	-43%
Guan	$k_{g,1}$	1.63	91%	0.27	-68%
	$k_{g,2}$	2.0×10^7	-49%	3.1×10^9	7958%
Inverse 1	k_i	3.60×10^4	0%	3.42×10^4	-4.8%
Inverse 2	$k_{ir,1}$	-0.26	192%	0.16	–
	$k_{ir,2}$	3.67×10^4	1.5%	2.0×10^4	-45%
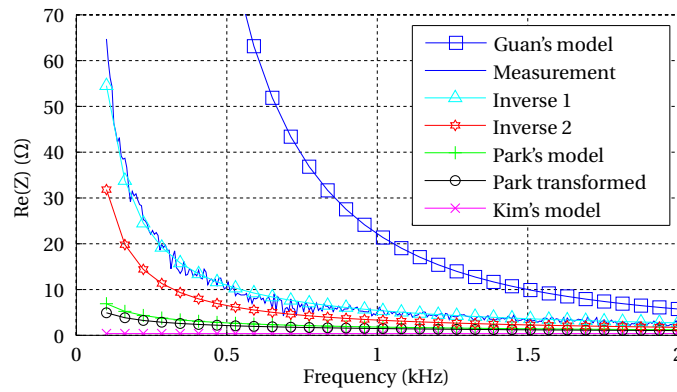
Figure 3.9 – Regression sensitivity test with a high frequency range data set

Results in Table 3.3 give the new estimated parameters and its relative difference compared to their values in Table 3.1. It shows that the proposed inversely proportional model is the most robust one, which means the model coefficient is nearly unchanged versus the change of data set and it can be extrapolated without lack of accuracy. The Park's model is not very sensitive to low frequency range data set, but it does not work properly for the case with the high frequency range data set. The other models are not suitable at all in term of sensitivity with different frequency ranges. Fig. 3.9 shows the extrapolation of each model in the low frequency range with only high frequency data to perform the regression. It can be noticed the inversely proportional model (in triangle) fits best the real data.

3.6.2 Plate damping ratio results

The inversely proportional model of piezoelectric actuators has been found to be the most suitable to present the real part of the actuator's impedance. According to (3.34), the square

of vibration amplitude is proportional to $\Re(\bar{Z}_t) - \Re(\bar{Z}_p)$. One can determine the half-power frequency with the curve of $\Re(\bar{Z}_t)$ and $\Re(\bar{Z}_p)$. Then the damping ratio can be obtained with (3.23).
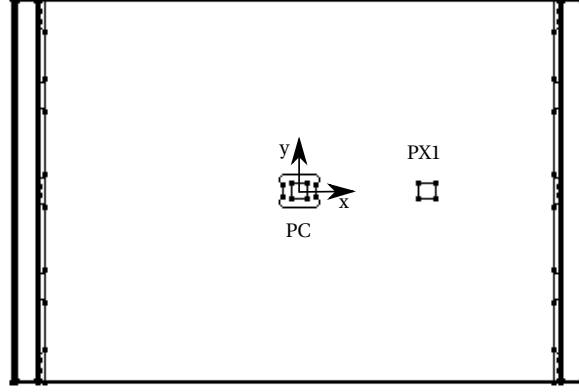
Figure 3.10 – A rectangular plate with two piezoelectric actuators (PC and PX1). The size of the plate is 160 x 120 x 5 mm^3. The size of piezoelectric actuators is 10 x 10 x 2 mm^3.
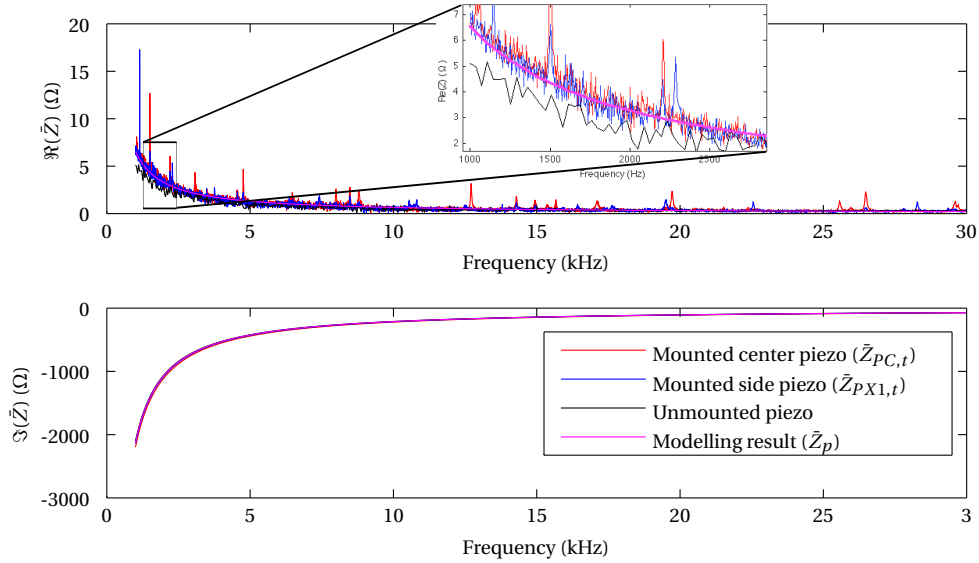
Figure 3.11 – Impedance of piezoelectric actuators in different conditions (mounted/unmounted/modelled)

The experiments have been carried out for a plate sizing 160 x 120 x 5 mm^3 with two identical piezoelectric actuators (PC and PX2 in Fig. 3.10) glued on one side and powered up with a 100 V sinusoidal signal. The experiment is firstly achieved with the method proposed. The

measurement of the impedance is given in Fig. 3.11. It can be found that eigenmodes appear at frequencies where peaks of $\Re(\bar{Z}_t)$ are present. Because the position of the piezoelectric actuator can be at the node of a mode, not every eigenmodes of the plate can be respectively excited by two actuators [90]. In order to compare the results and to study the effectiveness of the method, we have chosen two eigenmodes which can be created both by the actuators. Then an accurate measurement process, using a Doppler Laser Vibrator (CLV from Polytec™), have been performed. the comparison of the results is given in Table 3.4.

It can be noticed at 1500 Hz, the amplitude results give a maximum relative error of 4%. However, for the 4760 Hz mode, the relative error goes up to 25%. It is due to the influence of the next eigenmode nearby at 4820 Hz. Although, the result is not as accurate as the result obtained by the direct displacement measurement, it is still acceptable and can help to give an estimation of the system properties.

Table 3.4 – Estimated and measured plate damping ratios comparison

Frequency (Hz)	Piezo name	ζ_{est}	ζ_m	Error ($\Delta\zeta\%$)
1500	PC	4.76^{-3}	4.96×10^{-3}	-4%
	PX1	5.13^{-3}	5.21×10^{-3}	-1.5%
4760	PC	4.55^{-3}	4.13×10^{-3}	10%
	PX1	4.63^{-3}	3.70×10^{-3}	25%

3.7 Conclusion

The modelling of the vibratory plate is based on the Kirchhoff plate theory. The classical motion equation have been applied for the case with a pulse excitation. The response at another point of the plate has been calculated. The result depends on the eigenmode pattern, the eigenfrequency and the damping ratio. This expression provides a reference of the wave shape for the wave detection and is useful for the theoretical analysis of the wave creation.

Knowing the piezoelectric element equivalent circuit is important to predict the behaviour of a system. For our applications, the real part of its impedance within a non-resonanant frequency range is the most interesting one, therefore an accurate model is necessary. Five models have been reviewed in this chapter. Their analytical expressions are given with the estimation of parameters by using the least-squares method. The Park's model fits better the piezo measurement data and it has the lowest error variance compared to other models. However, sensitivity tests showed its parameters are not robust enough. A proposed inversely proportional model has a low variance and the best performance in sensitivity analysis. Moreover, this latter is possible to be solved with an analytical expression.

Using this accurate actuator impedance model and mechanical model, the vibration ampli-

tude can be determined analytically, which can be used to calculate the damping ratio. The advantage of this method is that it avoids using a bulky machine for the test. The efficiency of the test has been greatly improved, because only electrical measurements are sufficient to estimate the damping ratio/quality factor and the vibration amplitude.

Relative publications to the chapter

- X. Liu, Y. Civet and Y. Perriard, "Quality factor and vibration amplitude estimation of a piezoelectric-actuated system using impedance measurements," *2015 18th International Conference on Electrical Machines and Systems (ICEMS)*, Pattaya, 2015, pp. 1993-1996.

- X. Liu, Y. Civet and Y. Perriard, "Equivalent piezoelectric actuator circuits and comparison," *2014 IEEE/ASME International Conference on Advanced Intelligent Mechatronics*, Besançon, 2014, pp. 222-226.

4 Acoustic emission source position detection

Contents

This chapter presents the theoretical analysis of the time reversal effect used for position detection through a pulse excitation. Firstly, the modelling of interactions between a plate and a piezoelectric sensor glued on the bottom is introduced. Secondly, the reciprocal effect is studied for the creation of vibrations on the plate through a piezoelectric actuator. The two parts of modelling allow to find out expressions for a restored vibration amplitude via the time reversal method. Then, the study focuses on the calculation of the exact amplitude for each position using these expressions. An application on an ideal beam provides an example for the application of the theory. The calculation of the amplitude can help to establish a guideline for the detection of pulse excitation sources.

4.1 Introduction

The acoustic emission sources identification can help to detect part dropping positions on a working plate. According to the state of the art, the basic principle is to collect vibration signals, mirror and resend them to an actuator at the same position of the sensor. It is said a maximum amplitude will be restored at the original excitation position, but without any proof.

Indeed, in practice, one can find multiple peaks after applying the time reversal method. The questions are "How can we guarantee that maximum peak being always at the right excitation position?" and "is there any rule to determine the position of the other peaks?". These questions are crucial for the application of the time reversal method, because if a case exists where the restored peak cannot stand for the excitation position, a false detection information will be given.

Therefore, a theoretical analysis is necessary to study the properties of the results obtained by time reversal process. It can help to predict the details of the waveform and can describe the patterns of signals which can be used for the detection.

According to previous studies [29] and [31], the direct displacement was used as the vibration signal for the time reversal process. However, the study of a plate given in previous chapter (reference to (3.22)) shows the projection of displacement on an eigenmode is inversely proportional to its eigenfrequency, which will cause the loss of information for high frequency modes. In our application, piezoelectric sensor and actuator will be adopted. It will be interesting to study the influence of this configuration and to see whether it is a better choice for the time reversal process or more concretely, if it can cancel the negative effect of the inversely proportional coefficient. As a result, at the beginning of the chapter, the modelling of the interaction between the plate and the sensor/actuator will be introduced.

The expression of the obtained amplitude after time reversal process is a weighted sum of infinite eigenmodes. It becomes difficult to calculate the exact amplitude for all positions on a plate. This chapter will propose an innovative mathematical method to deal with the infinity problem. We will define the hypotheses and transform the eigenmodes to normalised ones. Then the distribution of eigenmode amplitude values will be used to calculate an averaged amplitude instead of adding them one by one. This method permits to obtain relative amplitudes on the plate for different positions.

The applications on an ideal beam will then be discussed in order to evaluate the theoretical modelling. After proving the hypothesis and calculations, we can find the time reversal process will give not only a pulse peak at original excitation position, but also three affiliate peaks elsewhere with a smaller amplitude. This result is then verified by a numerical simulation.

4.2 Piezoelectric sensor principle

In order to determine the position of an acoustic emission source, the vibrations measurement of a working plate is a key step to collect displacement information. As introduced in previous chapters, piezoelectric sensors will be used to perform this task. It will be interesting to know how the piezoelectric sensors interact with a plate. In this section, the modelling of the sensing mechanism will be presented, which can help to give the relation between the deformation and the generated electrical signal.

Compared to the size of a working plate, piezoelectric sensors are much smaller and thiner. When glued on a working plate, it can be considered as a small elementary segment on the surface of a working plate. Because of the size difference, we assume the deformation of the plate will not be influenced by the stress created by the sensor. The plate is also assumed to meet all Kirchhoff's plate assumptions.

Fig. 4.1 gives an illustration of the deformed plate in the xOz plane. As the piezoelectric sensor is an elementary segment, we designate its length by a, and horizontal deformation of the piezoelectric element is equal to the deformation of the plate bottom surface.
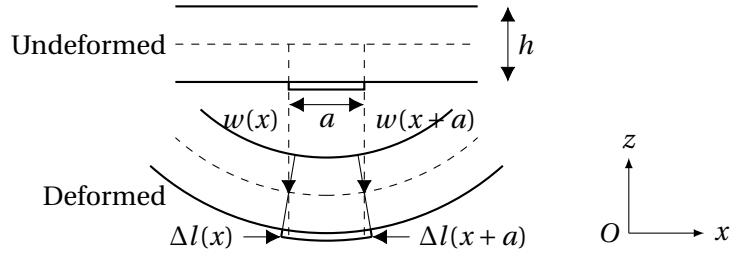
Figure 4.1 – Undeformed and deformed plate (section in plane xOz) with a piezoelectric sensor glued on the bottom surface

The distance between the middle plane and the bottom surface is $\frac{h}{2}$. According to (3.2), the displacement of the bottom surface at position x in direction x is:

$$\Delta l(x) = -\frac{h}{2}\frac{\partial w}{\partial x} \tag{4.1}$$

The strain S of the piezoelectric sensor glued at position x is then:

$$S(x) = \frac{\Delta l(x+a) - \Delta l(x)}{a} = -\frac{h}{2}\frac{\partial w(x+a) - \partial w(x)}{\partial x a} \approx -\frac{h}{2}\frac{\partial w^2(x)}{\partial x^2}\bigg|_{(a\to 0)} \tag{4.2}$$

In the y direction, the result is similar to (4.2). In the z direction, no stress is applied on the sensor. The deformation is only caused by Poisson's effect. Because of the small thickness, we suppose the shear strains in x and y directions can be ignored (very limited contribution for the calculation afterwards). The strain vector expression for a piezoelectric sensor at position

(x, y) on the bottom surface of a deformed plate becomes:

$$\mathbf{S}(x, y) = -\frac{h}{2}\begin{bmatrix} S_{xx} \\ S_{yy} \\ S_{zz} \\ S_{yz} \\ S_{zx} \\ S_{xy} \end{bmatrix} = -\frac{h}{2}\begin{bmatrix} \frac{\partial w^2(x,y)}{\partial x^2} \\ \frac{\partial w^2(x,y)}{\partial y^2} \\ -v(\frac{\partial w^2(x,y)}{\partial y^2} + \frac{\partial w^2(x,y)}{\partial x^2}) \\ 0 \\ 0 \\ 2\frac{\partial w^2(x,y)}{\partial x \partial y} \end{bmatrix} \tag{4.3}$$

where v is the Poisson's ratio.

As the piezoelectric element is used as a sensor, it is connected to a voltmeter which can be considered as an open circuit. Thus, the electric displacement field $\mathbf{D}$ is equal to 0. According to (2.2), the stress $\mathbf{T}$ can be expressed by the electric field $\mathbf{E}$:

$$\mathbf{T} = -\mathbf{d}^{-1}\epsilon^T\mathbf{E} \tag{4.4}$$

Bringing (4.4) to (2.1), we can finally obtain the relation between electric field and strain:

$$\mathbf{E} = (\mathbf{d}^T - \mathbf{d}^{-1}\epsilon^T)^{-1}\mathbf{S} = \mathbf{h}\mathbf{S} \tag{4.5}$$

For simplification purpose, we note $\mathbf{h} = (\mathbf{d}^T - \mathbf{d}^{-1}\epsilon^T)^{-1}$. The poling direction of the piezoelectric sensor is supposed to be parallel to z-axis. Then $\mathbf{d}$ and ϵ take the following forms [43]:

$$\mathbf{d} = \begin{bmatrix} 0 & 0 & 0 & 0 & d_{15} & 0 \\ 0 & 0 & 0 & d_{24} & 0 & 0 \\ d_{31} & d_{32} & d_{33} & 0 & 0 & 0 \end{bmatrix}, \quad \epsilon = \begin{bmatrix} \epsilon_{11} & 0 & 0 \\ 0 & \epsilon_{22} & 0 \\ 0 & 0 & \epsilon_{33} \end{bmatrix} \tag{4.6}$$

According to the definition [43], the $\mathbf{h}$ matrix should also be in the form of:

$$\mathbf{h} = \begin{bmatrix} 0 & 0 & 0 & 0 & h_{15} & 0 \\ 0 & 0 & 0 & h_{24} & 0 & 0 \\ h_{31} & h_{32} & h_{33} & 0 & 0 & 0 \end{bmatrix} \tag{4.7}$$

The electrodes are placed on the top and the bottom of the piezoelectric ceramic. Supposing the hight of the piezoelectric layer is d_p. The voltage difference between the electrodes is:

$$V_p = E_{zz}d_p = -\frac{hd_p}{2}\left[(h_{31} - vh_{33})\frac{\partial w^2(x, y)}{\partial x^2} + (h_{32} - vh_{33})\frac{\partial w^2(x, y)}{\partial y^2}\right] \tag{4.8}$$

If the actuator is isotropic in x and y-directions, we have $h_{31} = h_{32}$ and the voltage generated

is proportional to the spatial Laplacian of the displacement.

$$V_p = k_s \nabla^2 w(x, y) \tag{4.9}$$

where $k_s = -\frac{h d_p}{2}(h_{31} - \nu h_{33})$ and ∇^2 is the Laplace operator defined as $\nabla^2 = \frac{\partial^2}{\partial x^2} + \frac{\partial^2}{\partial y^2}$.

For the piezoelectric sensor, the electric voltage signal due to an unity excitation pulse at point A can be obtained by bringing (3.22) into (4.9):

$$V_p = k_s \sum_n \frac{\psi_n(\mathbf{A}) \nabla^2 \psi_n(\mathbf{P})}{\omega_n} \sin(\omega_n t) e^{-\zeta_n \omega_n t} H(t) \tag{4.10}$$

where $\mathbf{P} = (x_p, y_p)$ denotes the position of the piezoelectric sensor.

The sensing voltage expression is valid only if half wavelength of an eigenmode of the plate is larger than the size of the piezoelectric element. If not, the sign of $\Delta l(x)$ will change more than once inside the interval $[x, x + dx]$ where the sensor is present as shown in Fig. 4.1, which will cause the sensor partly compressed and partly stretched. The above modelling will no longer be valid. Normally, in that case, the voltage created by compressed parts and stretched parts will be mostly cancelled out. The result voltage becomes much smaller than the voltage obtained from (4.10).

4.3 Piezoelectric actuator principle

When applying a voltage, piezoelectric elements can be used to create vibrations. Using the time-reversal method, these vibrations can help to "restore" the original excitation pulse, which permits to identify the emission source position. Thus, it is necessary to carry out a modelling on the interaction between a piezoelectric actuator and a plate.

The piezoelectric element is supposed to be very small as described in the previous section. In x and y direction, the strain is assumed to be very small compared to the corresponding components of $\mathbf{s^E T}$ and $\mathbf{d}^T \mathbf{E}$, therefore, the influence caused by the deformation of a plate for the actuator is not considered.

Given a voltage V_p applied on the top electrode of the piezoelectric actuator and supposing the bottom electrode is connected to the ground potential, the electric field applied across the piezoelectric element is only in z direction so that $E_{zz} = \frac{V_p}{d_p}$:

$$\mathbf{T} = -\mathbf{s^{E^{-1}}} \mathbf{d}^T \mathbf{E} = -\mathbf{e}^T \mathbf{E} \tag{4.11}$$

where $\mathbf{e}^T = \mathbf{s^{E^{-1}}} \mathbf{d}^T$.

Because the piezoelectric actuator is glued on the bottom of the plate, it has no constraint generated from the plate in the z direction. The only interactions between the plate and the

actuator are T_{xx} and T_{yy}, which are proportional to the supply voltage (reference to (4.11)). Here we note k_e as the proportional coefficient and we have $T_{xx} = T_{yy} = k_e V_p$.

(a) Horizontal forces created by the piezoelectric actuator are equivalent to moments applied on the plate

(b) Equivalent perpendicular forces replacing the moments
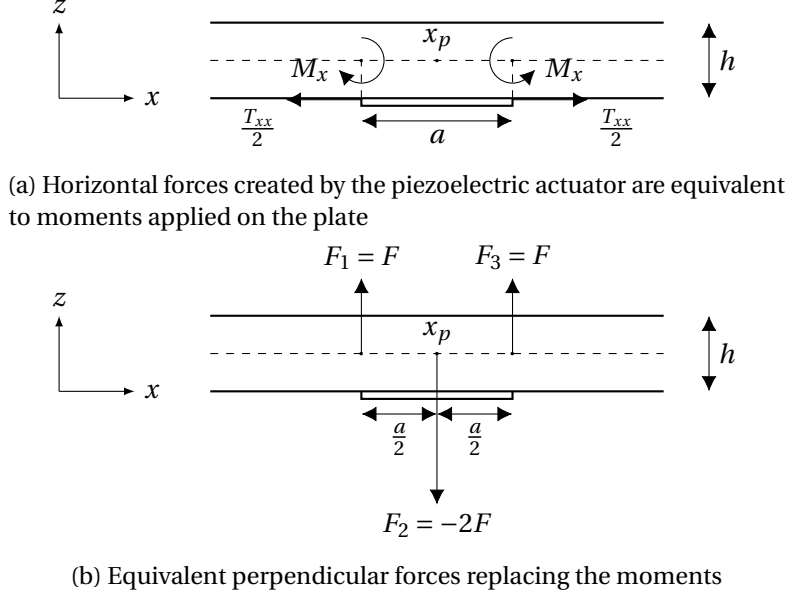
Figure 4.2 – Interaction between a piezoelectric actuator and a working plate in the xOz plane

The force created by the piezoelectric actuator applies also on the bottom of the plate. According to the Kirchhoff's assumptions, a surface point (x,y) rotates around the corresponding point on the middle line. For two dimensional case shown in Fig. 4.2a, the forces $\frac{T_{xx}}{2}$ on both ends of the piezoelectric element can be replaced by two equivalent moments at the middle line. The value of the equivalent moment is $M_x = \frac{T_{xx}h}{4}$.

Supposing the middle point of the piezoelectric actuator is x_p, the moments at $x_p - \frac{a}{2}$ and $x_p + \frac{a}{2}$ can also be replaced by the forces shown in Fig. 4.2b.

$$F = \frac{M_x}{\frac{a}{2}} = \frac{h}{2}\frac{T_{xx}}{a} = \frac{h}{2}\frac{k_e V_d}{a} \tag{4.12}$$

One can use a pulse voltage as the input signal for the actuator. Supposing $V_d(t) = V_0\delta(t)$, the three equivalent forces applied vertically on the plate are:

$$F_1(x,t) = \frac{h}{2}\frac{k_e V_0}{a}\delta(t)\delta(x - (x_p - \frac{a}{2})) \tag{4.13a}$$

$$F_2(x,t) = -2\frac{h}{2}\frac{k_e V_0}{a}\delta(t)\delta(x - x_p) \tag{4.13b}$$

$$F_3(x,t) = \frac{h}{2}\frac{k_e V_0}{a}\delta(t)\delta(x - (x_p + \frac{a}{2})) \tag{4.13c}$$

Each force in (4.13) will lead to a deformation on the plate indicated in (3.22). As the plate is

supposed to be made of a linear material, the total deformation becomes the sum of these deformations. The displacement along x-axis can then be written as:

$$
\begin{aligned}
w_p(x,t) =\; & \frac{k_f}{(\frac{a}{2})^2} V_0 \sum_n \frac{\psi_n(x_p - \frac{a}{2})\psi_n(x)}{\omega_n} \sin(\omega_n t) e^{-\zeta_n \omega_n t} H(t) \\
& - 2\frac{k_f}{(\frac{a}{2})^2} V_0 \sum_n \frac{\psi_n(x_p)\psi_n(x)}{\omega_n} \sin(\omega_n t) e^{-\zeta_n \omega_n t} H(t) \\
& + \frac{k_f}{(\frac{a}{2})^2} V_0 \sum_n \frac{\psi_n(x_p + \frac{a}{2})\psi_n(x)}{\omega_n} \sin(\omega_n t) e^{-\zeta_n \omega_n t} H(t) \\
=\; & k_f V_0 \sum_n \frac{[\psi_n(x_p + \frac{a}{2}) - \psi_n(x_p)] - [\psi_n(x_p) - \psi_n(x_p - \frac{a}{2})]}{(\frac{a}{2})^2} \frac{\psi_n(x)}{\omega_n} \sin(\omega_n t) e^{-\zeta_n \omega_n t} H(t) \\
\approx\; & k_f V_0 \sum_n \frac{\partial^2 \psi_n(x_p)}{\partial x^2} \frac{\psi_n(x)}{\omega_n} \sin(\omega_n t) e^{-\zeta_n \omega_n t} H(t) \Big|_{(a \to 0)}
\end{aligned}
\tag{4.14}
$$

where $k_f = \frac{k_e a}{8\rho}$ which is a coefficient depending on the plate density, the actuator's piezoelectric proprieties and its length. An approximation has been made in (4.14) under the condition that the size of the piezoelectric actuator should be smaller than the half spatial wavelength of the eigenmodes.

The analysis in the y direction is similar to the one in the x direction. In a three-dimensional case, one can notice the amplitude expression for each direction depends on the length of the actuator in the considered direction. A rectangular actuator can create a directional vibration thanks to a large ratio between its length and width. A square piezoelectric actuator, it will create a same displacing effect in both directions, the displacement under unity voltage ($V_0 = 1$) can be written as:

$$
w_p(\mathbf{X}, t) = k_f \sum_n \frac{\psi_n(\mathbf{X}) \nabla^2 \psi_n(\mathbf{P})}{\omega_n} \sin(\omega_n t) e^{-\zeta_n \omega_n t} H(t)
\tag{4.15}
$$

If an arbitrary voltage signal $V_d(t)$ is applied across the piezoelectric actuator, one can transform it into the sum of a series of Dirac functions: $V_d(t) = \int_{-\infty}^{\infty} V_d(\tau)\delta(t - \tau)d\tau$. According to the linearity behaviour of the system, the displacement due to V_d is given in (4.16).

$$
w(\mathbf{X}, t) = \int_{-\infty}^{\infty} V_d(\tau) w_p(\mathbf{X}, t - \tau)d\tau = w_p(\mathbf{X}, t) * V_d(t)
\tag{4.16}
$$

where $*$ is the convolution operator.

4.4 Time reversal process

According to the time reversal method presented in Section 2.2.2, an excitation pulse can be restored at the same place it is applied. Thus, this phenomenon can be used to detect the excitation position. Fig. 4.3 shows the basic operation principle. Given an excitation on a plate,

one can collect the vibration signal by a displacement sensor. Then a FEM (Finite Element Method) simulation can be conducted for the plate. In the simulation, the piezoelectric actuator powered up with the reversal signal will create vibrations on the plate. The displacement of surface nodes will be saved. Finally, the maximal value among all saved values corresponding to the position where the emission has occured.
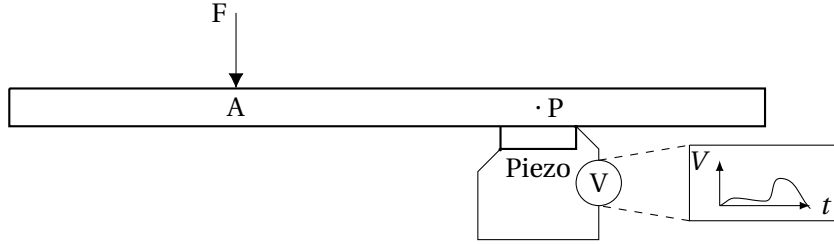
(a) An excitation pulse is applied at point A. A piezoelectric sensor is used to record the displacement information at point P.
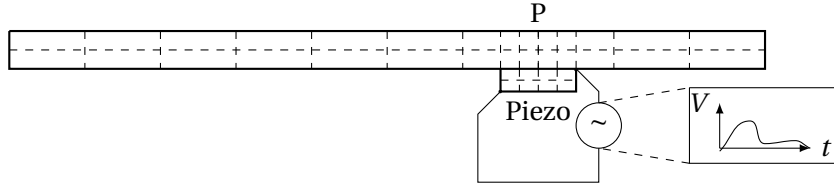
(b) The FEM model of the system is created. The reversed calculation of the signal obtained in previous step is applied on the piezoelectric actuator to simulate the plate vibration. The resulting surface displacement according to the simulation will be saved.

Figure 4.3 – Principle of detection process using the reversal effect

As mentioned in the state of the art, [29] and [31] discussed the modelling of the time reversal effect. They used directly the surface displacement (using a laser doppler vibrometer for example) to restore the original signal. The signal they obtained should be in form of (3.22), in which the amplitude of each mode is inversely proportional to its angular frequency. Due to this effect, high frequency components will be filtered out, resulting in a loss of accuracy when restoring the original signal. However, the use of piezoelectric sensors will overcome this problem, which can be demonstrated with an analytical study of the problem.

4.4.1 Mathematical development for the time reversal principle

In this section, we will establish the analytical model of the time reversal process using piezoelectric sensors in order to reveal its proprieties and application constraints.

According to the principle of time reversal process, the signal measured at point P by the piezoelectric sensor will be recorded during a period T. Then it will be mirrored and replayed as an input voltage at the same point P through a piezoelectric actuator. As we are waiting for the reproduction of the original signal at instant zero, the reversed signal should begin at instant $-T$. Equation (4.10) is the formula for the response at P due to a Dirac input force at A.

Here we note the measured voltage as follows:

$$V_{p,\mathbf{A}}(\mathbf{P},t) = k_s \sum_n \frac{\psi_n(\mathbf{A})\nabla^2\psi_n(\mathbf{P})}{\omega_n} \sin(\omega_n t) e^{-\zeta_n\omega_n t} H(t) \tag{4.17}$$

Supposing the reversed signal $V_{p,\mathbf{A}}^T(\mathbf{P},t)$ begins at $-T$, its expression is then:

$$V_{p,\mathbf{A}}^T(\mathbf{P},t) = V_{p,\mathbf{A}}(\mathbf{P},-t)H(t+T) \tag{4.18}$$

Then the reversed signal will be used as the voltage input for a piezoelectric actuator. Bringing (4.18) to (4.16), the resulting displacement can be written as:

$$w_{\mathbf{A},\mathbf{P}}(\mathbf{X},t) = w_p(\mathbf{X},t) * V_{p,\mathbf{A}}^T(\mathbf{P},t) \tag{4.19}$$

Taking (4.15), (4.17) and (4.18) into (4.19), we have:

$$w_{\mathbf{A},\mathbf{P}}(\mathbf{X},t) = \int_{-\infty}^{\infty} w_p(\mathbf{X},t-\tau) * V_{p,\mathbf{A}}^T(\mathbf{P},\tau)d\tau = \int_0^T w_p(\mathbf{X},t+\tau) * V_{p,\mathbf{A}}^T(\mathbf{P},-\tau)d\tau$$

$$= k_s k_f \sum_n \sum_m \frac{\psi_n(\mathbf{X})\nabla^2\psi_n(\mathbf{P})}{\omega_n} \frac{\psi_m(\mathbf{A})\nabla^2\psi_m(\mathbf{P})}{\omega_m} I_{nm} \tag{4.20}$$

where:

$$I_{nm} = \int_0^T \sin(\omega_n(t+\tau))\sin(\omega_m\tau)e^{-\zeta_n\omega_n(t+\tau)}e^{-\zeta_m\omega_m\tau}d\tau$$

$$= e^{-\zeta_n\omega_n t}\int_0^T \sin(\omega_n(t+\tau))\sin(\omega_m\tau)e^{-(\zeta_n\omega_n+\zeta_m\omega_m)\tau}d\tau$$

$$= \frac{e^{-\zeta_n\omega_n t}}{2}\left[e^{-(\zeta_n\omega_n+\zeta_m\omega_m)\tau}\left(\frac{(\omega_n-\omega_m)\sin(\omega_n t+(\omega_n-\omega_m)\tau)}{(\omega_n-\omega_m)^2+(\zeta_n\omega_n+\zeta_m\omega_m)^2}\right.\right.$$

$$-\frac{(\zeta_n\omega_n+\zeta_m\omega_m)\cos(\omega_n t+(\omega_n-\omega_m)\tau)}{(\omega_n-\omega_m)^2+(\zeta_n\omega_n+\zeta_m\omega_m)^2}$$

$$\left.\left.+\frac{(\zeta_n\omega_n+\zeta_m\omega_m)\cos(\omega_n t+(\omega_n+\omega_m)\tau)}{(\omega_n+\omega_m)^2+(\zeta_n\omega_n+\zeta_m\omega_m)^2} - \frac{(\omega_n+\omega_m)\sin(\omega_n t+(\omega_n+\omega_m)\tau)}{(\omega_n+\omega_m)^2+(\zeta_n\omega_n+\zeta_m\omega_m)^2}\right)\right]_0^T \tag{4.21}$$

For the cases where two modes have significant different frequencies, $\omega_n-\omega_m$ and $\omega_n+\omega_m$ are relatively great, thus $I_{nm} \approx 0$. Otherwise, if $\omega_n-\omega_m \ll \omega_n+\omega_m$, the last two terms of (4.21) can be ignored. Then I_{nm} becomes:

$$I_{nm} = \frac{e^{-\zeta_n\omega_n t}}{2}\left[e^{-(\zeta_n\omega_n+\zeta_m\omega_m)\tau}\left(\frac{\sin(\omega_n t+(\omega_n-\omega_m)\tau-\theta)}{\sqrt{(\omega_n-\omega_m)^2+(\zeta_n\omega_n+\zeta_m\omega_m)^2}}\right)\right]_0^T$$

$$= e^{-\zeta_n\omega_n t}\frac{e^{-(\zeta_n\omega_n+\zeta_m\omega_m)T}\sin(\omega_n t+(\omega_n-\omega_m)T-\theta)-\sin(\omega_n t-\theta)}{2\sqrt{(\omega_n-\omega_m)^2+(\zeta_n\omega_n+\zeta_m\omega_m)^2}} \tag{4.22}$$

where $\theta = \arcsin(\frac{(\zeta_n \omega_n + \zeta_m \omega_m)^2}{\sqrt{(\omega_n - \omega_m)^2 + (\zeta_n \omega_n + \zeta_m \omega_m)^2}})$. Considering the case when $T \to \infty$, the asymptotic value of I_{nm} can be found.

$$I_{nm}^{T\infty} = e^{-\zeta_n \omega_n t} \frac{\sin(\theta - \omega_n t)}{2\sqrt{(\omega_n - \omega_m)^2 + (\zeta_n \omega_n + \zeta_m \omega_m)^2}} \tag{4.23}$$

Noticing that the partial derivative of (4.23) with respect to $(\omega_n - \omega_m)$ is of the form $(\omega_n - \omega_m) \cdot f((\omega_n - \omega_m))$, it will be zero if $(\omega_n - \omega_m) = 0$. As a result, $I_{nm}^{T\infty}$ have their maximal values at diagonal (m=n). Then, if T is significant enough, it is natural to make an approximation of $w_{A,P}(X, t)$ using only I_{nn}.

$$w_{A,P}(X, t) \approx k_s k_f \sum_n \psi_n(X) \psi_n(A) \left(\frac{\nabla^2 \psi_n(P)}{\omega_n} \right)^2 \frac{1 - e^{-2\zeta_n \omega_n T}}{4\zeta_n \omega_n} \cos(\omega_n t) e^{-\zeta_n \omega_n t} \tag{4.24}$$

According to the expression of (4.24), the final displacement has a maximum at $t = 0$ which corresponds to the applied moment of the original pulse input. The total amplitude is related to the amplitude of eigenmodes at X, A and P which can be determined by the geometry of the object.

4.4.2 Spatial amplitude properties

The spatial eigenmode coefficients in (4.24) determine the maximal vibration amplitude at position X on the plate. It will be interesting to study the roles of these coefficients.

k_s and k_f are constant coefficients inherited from the coupling effect between the piezoelectric actuator and the plate introduced in Section 4.2 and Section 4.3. Once the material and the dimensions of the actuator is chosen, these coefficients become constant and they do not depend on the position of the sensor/actuator. The part $\frac{1 - e^{-2\zeta_n \omega_n T}}{4\zeta_n \omega_n}$ of (4.24) is related to the damping effect for each mode, normally it varies depending on the frequency. It depends also on the reversal signal duration and will attenuate the amplitude of each mode with different critical times. The detail effect of this term will be discussed in next chapter.

Now we consider an ideal case where the damping term for each frequency has the same numerical value. Thus one can move this term outside the sum and put it with the $k_s k_f$ coefficients. As a result, we can concentrate only on the spatial eigenmode part.

$$M_{A,P}(X) = \sum_n \psi_n(X) \psi_n(A) \left(\frac{\nabla^2 \psi_n(P)}{\omega_n} \right)^2 \tag{4.25}$$

Eigenmodes ψ_n form an orthogonal basis which can generate a Hilbert space $\mathcal{H}$ with an inner product defined as $< \psi_n, \psi_m > = \int_S \psi_n \psi_m ds$ where S is the surface of the plate. Given a pulse displacement $\delta(X - A)$ at position A, we can make a decomposition in the space $\mathcal{H}$ on this

orthogonal basis.

$$\delta(\mathbf{X}-\mathbf{A}) = \sum_n \int_S \delta(\mathbf{X}-\mathbf{A})\psi_n(\mathbf{X})\,ds\,\psi_n(\mathbf{X}) = \sum_n \psi_n(\mathbf{X})\psi_n(\mathbf{A}) \tag{4.26}$$

According to (4.26), at all positions where $\mathbf{X}$ is different from $\mathbf{A}$, we have $\sum_n \psi_n(\mathbf{A})\psi_n(\mathbf{X}) = 0$. If we compare (4.25) and (4.26), the only difference is $\left(\frac{\nabla^2\psi_n(\mathbf{P})}{\omega_n}\right)^2$. The latter plays the role of weighting term for different eigenmode components in (4.26).

Reduction of ω_n

For a Kirchhoff plate, ψ_n are solutions of (3.13). Its general solution form is a sum of sinusoidal functions and hyperbolic functions whose spatial angular frequency is $\beta = \sqrt[4]{\omega_n^2 \frac{\rho h}{D}}$. We note $\psi_n = \psi_{n,s} + \psi_{n,h}$, where $\psi_{n,s}$ is the sinusoidal part and $\psi_{n,h}$ is the hyperbolic part. The Laplacian of ψ_n can then be written as:

$$\nabla^2\psi_n = \nabla^2\psi_{n,s} + \nabla^2\psi_{n,h} = \omega_n\sqrt{\frac{\rho h}{D}}(-\psi_{n,s}+\psi_{n,h}) \tag{4.27}$$

Bringing (4.27) into (4.25), the expression of $M_{\mathbf{A},\mathbf{P}}(\mathbf{X})$ is indeed not explicitly depending on eigen-frequencies.

$$M_{\mathbf{A},\mathbf{P}}(\mathbf{X}) = \frac{\rho h}{D}\sum_n \psi_n(\mathbf{A})\psi_n(\mathbf{X})(\psi_{n,s}(\mathbf{P})-\psi_{n,h}(\mathbf{P}))^2 \tag{4.28}$$

This property shows the advantage of using piezoelectric sensors and actuators for the application of time reversal process. In contrary to other studies using directly vertical displacement information as input signal, our application using the Laplacian of the displacement can cancel the attenuation effect of eigenfrequencies.

Amplitude estimation

Due to the attenuation term, the amplitude of each eigenmodes will be weighted by the amplitude where the piezoelectric element is placed. We want to estimate the resulting amplitude in oder to evaluate the effect of this term. Because there are infinite eigenmodes whose sum results to an infinite value at position A, it is difficult to analyse the value of the amplitude.

In order to solve this problem, we have to create a new measure to evaluate the amplitude. As n can be considered great enough, a distribution of the eigenmodes' amplitude values could be adopted. First of all, we suppose ψ_n can satisfy following hypotheses:

i. For all $\mathbf{X}$, the value of $\psi_{n,s}(\mathbf{X}) \pm \psi_{n,h}(\mathbf{X})$ is almost bounded, which can be defined as $\exists M$, $\forall \varepsilon > 0$, $\exists N$, $\forall n > N$ such that $\psi_{n,s}(\mathbf{X}) \pm \psi_{n,h}(\mathbf{X}) \in [-M - \varepsilon, M + \varepsilon]$.

ii. Given a position X, supposing n_{m_1,m_2} is the number of eigenmodes whose value at position X is between m_1 and m_2 ($-M < m_1 < m_2 < M$), the series $\frac{n_{m_1,m_2}}{n}$ converges while n tends towards infinity.

iii. Given a position X, the series $\frac{n_{m_1,m_2}}{n}$ for $\psi_{n,s}(\mathbf{X}) + \psi_{n,h}(\mathbf{X})$ and $\psi_{n,s}(\mathbf{X}) - \psi_{n,h}(\mathbf{X})$ converge to the same value.

According to hypothesis i., we assume the value of $\psi_{n,s}(\mathbf{X}) \pm \psi_{n,h}(\mathbf{X})$ is between $-M$ and M, $M \in \mathbb{R}$. The amplitude of each eigenmode can be divided by M to obtain a normalised amplitude. Then we can define a function $\mathscr{D}_{\mathbf{X}}(x) : [-1, 1] \rightarrow \mathbb{R}$ which satisfies:

$$\mathscr{D}_X(x) = \left. \frac{n_{Mx,M(x+dx)}}{ndx} \right|_{dx \rightarrow 0} \tag{4.29}$$

Indeed, $\mathscr{D}_{\mathbf{X}}(x)$ is a distribution function of normalised amplitude. It is easy to see that the integration of $\mathscr{D}_{\mathbf{X}}(x)$ on the whole interval of $[-1, 1]$ tends to one. According to (4.26), the new amplitude at position A can be presented by the second order moment of the distribution $\mathscr{D}_{\mathbf{A}}(x)$:

$$w_{\mathbf{A}|_{\mathbf{A}}} = \int_{-1}^{1} x^2 \mathscr{D}_{\mathbf{A}}(x) dx \tag{4.30}$$

Given a n great enough, the amplitude obtained from (4.30) is equal to its original amplitude divided by nM.

Given a set of all eigenmodes who have a same amplitude yM at position A, they will spread apart at other positions. Supposing its distribution at position Y can also converge to a distribution function. We note this function as $\mathscr{D}_{\mathbf{X}|\mathbf{A}(y)}(X)$ and it can deduce the following relations:

$$\int_{-1}^{1} \mathscr{D}_{\mathbf{A}}(y) \mathscr{D}_{\mathbf{X}|\mathbf{A}(y)}(x) dy = \mathscr{D}_{\mathbf{X}}(x) \tag{4.31}$$

We call $\mathscr{D}_{\mathbf{X}|\mathbf{A}(y)}(x)$ the conditional distribution at position X for all eigenmodes passing by y at position A. The amplitude related to the expression in (4.26) can the be written as:

$$w_{\mathbf{X}|_{\mathbf{A}}} = \iint_{-1}^{1} xy \mathscr{D}_{\mathbf{A}}(y) \mathscr{D}_{\mathbf{X}|\mathbf{A}(y)}(x) dxdy \tag{4.32}$$

In order to introduce the attenuation term, we have to define a new conditional distribution $\mathscr{D}_{\mathbf{X}|\mathbf{A}(y),\mathbf{P}(p)}(x)$ for the eigenmodes passing both by normalised value y at position A and by p at position P. Thus, we can obtain a measure for the displacement taking into account the

attenuation term:

$$w_{\mathbf{X}|_{\mathbf{A}}^{\mathbf{P}}} = \iiint_{-1}^{1} xyp^2 \mathscr{D}_{\mathbf{A}}(y) \mathscr{D}_{\mathbf{P}|\mathbf{A}(y)}(p) \mathscr{D}_{\mathbf{X}|\mathbf{A}(y),\mathbf{P}(p)}(x) \, dy \, dp \, dx \qquad (4.33)$$

For example, the displacement at A can be noted as $w_{\mathbf{A}|_{\mathbf{A}}^{\mathbf{P}}}$. The conditional distribution of $\mathscr{D}_{\mathbf{A}|\mathbf{A}(y),\mathbf{P}(p)}(x)$ is equal to 1 if x is equal to y and to 0 if x is not equal to y, because, according to its definition, it represents all eigenmodes passing by y at A. Then, one can obtain:

$$\begin{aligned} w_{\mathbf{A}|_{\mathbf{A}}^{\mathbf{P}}} &= \iiint_{-1}^{1} xyp^2 \mathscr{D}_{\mathbf{A}}(y) \mathscr{D}_{\mathbf{P}|\mathbf{A}(y)}(p) \mathscr{D}_{\mathbf{A}|\mathbf{A}(y),\mathbf{P}(p)}(x) \, dy \, dp \, dx \\ &= \iint_{-1}^{1} y^2 p^2 \mathscr{D}_{\mathbf{A}}(y) \mathscr{D}_{\mathbf{P}|\mathbf{A}(y)}(p) \, dy \, dp \end{aligned} \qquad (4.34)$$

If the distribution function and conditional distribution function are obtained, one can calculate the averaged normalised amplitude analytically.

4.5 Case study: application on an ideal beam

There are three reasons why we choose an ideal beam as our case study target. The first reason is that it is sufficient to give a typical example to apply and to verify the theoretical analysis. The second reason is that in an ideal case, we have to treat an infinite number of eigenmodes. In reality, given certain calculation resources, the reduction of dimension allows us to achieve a better numerical approximation. The third reason is related to simulation constraints. According to the modelling of the interaction between a plate and a piezoelectric sensor, the minimal spatial wavelength of eigenmodes depends on the size of the piezoelectric element. In a FEM simulation, the mesh should be dense enough to guarantee the effectiveness of presenting these eigenmodes, which means once the size of the piezoelectric sensor is given, the number of nodes in a simulation is proportional to the surface of the plate. Due to the limit of memory and computation time, the use of a 3D beam becomes a reasonable choice for the FEM study.

In this case study, we will firstly give the eigenmode expressions and prove they can satisfy the hypotheses proposed in Section 4.4.2. Then, the estimation of amplitudes will show the result of amplitudes predicted by the mathematical approach. Finally, a brief guideline for the detection of the original pulse positions using the pattern obtained in previous steps will be given.

4.5.1 Eigenmodes of a beam

Given a normalised uniform beam of length $L = 1$ and height h, supposing it is under free vibration boundary conditions, according to [28], its eigenmodes are:

$$\psi_n(x) = \sinh(k_n x) + \sin(k_n x) + \frac{\sin(k_n) - \sinh(k_n)}{\cosh(k_n) - \cos(k_n)}(\cos(k_n x) + \cosh(k_n x)), \quad x \in [0, 1] \quad (4.35)$$

where k_n are the solutions of:

$$\cos(k_n)\cosh(k_n) = 1 \tag{4.36}$$

Because (4.36) is a transcendental equation, normally, its roots can be obtained only by numerical methods. However, we can still give approximate solutions thanks to its property. One can notice that $\cos(k_n) = \frac{1}{\cosh(k_n)}$. If we consider only positive solutions of k_n and we supposed k_n increases as its index n increases, $\frac{1}{\cosh(k_n)} = \frac{2}{e^{k_n} + e^{-k_n}}$ will tend to zero. Thus, the solution of (4.36) should be in form of $k_n = (n + \frac{1}{2})\pi + \mathcal{O}(e^{-\frac{n}{2}})$ where $\mathcal{O}$ is the big O notation. If approximate values $k'_n = (n + \frac{1}{2})$ are used instead of the exact solution k_n, for all $x \in [0, 1]$ we have:

$$\sin(k'_n x) = \sin(k_n x) + \mathcal{O}(e^{-\frac{n}{2}}) \tag{4.37a}$$
$$\cos(k'_n x) = \cos(k_n x) + \mathcal{O}(e^{-\frac{n}{2}}) \tag{4.37b}$$

4.5.2 Verification of the hypotheses

Almost bounded amplitude

In this section, the objective is to prove that the eigenmodes of a beam can satisfy the first hypothesis proposed in Section 4.4.2. Concretely, we will demonstrate that while $x \in (0, 1)$, $\exists M$, $\forall \varepsilon > 0$, $\exists N$, $\forall n > N$ such that $\psi_{n,s}(x) \pm \psi_{n,h}(x) \in [-M - \varepsilon, M + \varepsilon]$. Because of the free vibration boundary conditions, the amplitude at two ends of the beam (at x=0 and x=1) is always equal to 2. That is why we eliminate this two points from the range of x.

Proof. In order to prove $\psi_n(x)$ is almost bounded, we have to reformulate it and divide it into its sinusoidal part and its hyperbolical part.

$$\psi_n(x) = \psi_{n,s}(x) + \psi_{n,h}(x) \tag{4.38}$$

where

$$\psi_{n,s}(x) = \sin(k_n x) + \frac{\sin(k_n) - \sinh(k_n)}{\cosh(k_n) - \cos(k_n)}\cos(k_n x) \tag{4.39}$$

$$= \sqrt{1 + \left(\frac{\sin(k_n) - \sinh(k_n)}{\cosh(k_n) - \cos(k_n)}\right)^2}\sin(k_n x + \theta)$$

$$\psi_{n,h}(x) = \sinh(k_n x) + \frac{\sin(k_n) - \sinh(k_n)}{\cosh(k_n) - \cos(k_n)} \cosh(k_n x) \tag{4.40}$$

$$= \left(1 + \frac{\sin(k_n) - \sinh(k_n)}{\cosh(k_n) - \cos(k_n)} \sqrt{1 + \frac{1}{\sinh^2(k_n x)}}\right) \sinh(k_n x)$$

Then, we can write the coefficients containing k_n with big O notation. The common term of these two coefficients is:

$$\frac{\sin(k_n) - \sinh(k_n)}{\cosh(k_n) - \cos(k_n)} = \frac{\sin(k_n) - \sinh(k_n)}{\cosh(k_n) - \frac{1}{\cosh(k_n)}} = \frac{\sin(k_n)\cosh(k_n)}{\sinh^2(k_n)} - \frac{\cosh(k_n)}{\sinh(k_n)} \tag{4.41}$$

$$= \mathcal{O}(e^{-n}) - (1 + \mathcal{O}(e^{-2n}))$$

The results of related coefficients are given as follows:

$$\sqrt{1 + \left(\frac{\sin(k_n) - \sinh(k_n)}{\cosh(k_n) - \cos(k_n)}\right)^2} = \sqrt{2 + \mathcal{O}(e^{-n})} = \sqrt{2} + \mathcal{O}(e^{-n}) \tag{4.42}$$

$$1 + \frac{\sin(k_n) - \sinh(k_n)}{\cosh(k_n) - \cos(k_n)} \sqrt{1 + \frac{1}{\sinh^2(k_n x)}} = 1 + [-1 + \mathcal{O}(e^{-n})][1 + \mathcal{O}(e^{-2nx})] \tag{4.43}$$

$$= \mathcal{O}(e^{-n}) + \mathcal{O}(e^{-2nx})$$

In (4.40), the governing asymptotic function of $\sinh(k_n x)$ is $\mathcal{O}(e^{nx})$. It can be multiplied by the coefficient given in (4.43) to obtain the corresponding result for the hyperbolical part.

$$\psi_{n,h}(x) = (\mathcal{O}(e^{-n}) + \mathcal{O}(e^{-2nx}))\mathcal{O}(e^{nx}) = \mathcal{O}(e^{-n(1-x)}) + \mathcal{O}(e^{-nx}) \tag{4.44}$$

On the one hand, according to the definition of big O notation, for $\psi_{n,h}(x)$, $\exists M_1, M_2, N_1$ and N_2, $\forall n > \max(N_1, N_2)$, there is $|\psi_{n,h}(x)| < M_1 e^{-n(1-x)} + M_2 e^{-nx}$. If $n > \max(\frac{\log \frac{\varepsilon}{4M_1}}{1-x}, \frac{\log \frac{\varepsilon}{4M_2}}{x})$, we have $|\psi_{n,h}(x)| < \frac{\varepsilon}{2}$.

On the other hand, for $\psi_{n,h}(x)$, $\exists M_3$ and N_3, $\forall n > N_3$, there is $|\psi_{n,s}(x)| < \sqrt{2} + M_3 e^{-n}$. If $n > \log \frac{\varepsilon}{2M_3}$, we have $|\psi_{n,s}(x)| < \sqrt{2} + \frac{\varepsilon}{2}$.

Then we can combine these two parts, for any $\varepsilon > 0$, $\forall n > \max(N_1, N_2, N_3, \frac{\log \frac{\varepsilon}{4M_1}}{1-x}, \frac{\log \frac{\varepsilon}{4M_2}}{x}, \log \frac{\varepsilon}{2M_3})$, we have $|\psi_{n,s}(x) \pm \psi_{n,s}(x)| \le |\psi_{n,s}(x)| + |\psi_{n,h}(x)| < \sqrt{2} + \varepsilon$. As a result, the bound M is equal to $\sqrt{2}$ and the hypothesis i. is satisfied. $\square$

Convergence of $\frac{n_{m_1,m_2}}{n}$ and $\mathscr{D}_\mathbf{X}(x)$

We will use the previous asymptotic results to prove hypotheses ii. and iii.. As x is a real number on $(0,1)$, firstly, we will analyse the case while x is a rational number. Then the other case while $x \in (0,1) \cap \mathbb{R} \setminus \mathbb{Q}$ will be studied.

Proof. Case one: while $x \in (0,1) \cap \mathbb{Q}$, we note $x = \frac{a}{b}$ and $a, b \in \mathbb{Z}$. In (4.39), the phase parameter θ is equal to $\arctan\left(\frac{\sin(k_n)-\sinh(k_n)}{\cosh(k_n)-\cos(k_n)}\right)$. Its value can be obtained by Taylor's expansion around -1. Thus, it becomes $\theta = \arctan(-1 + \mathcal{O}(e^{-n})) = -\frac{\pi}{4} + \mathcal{O}(e^{-n})$.

Taking into account (4.37a) and (4.37b) and replacing k_n by k'_n, (4.39) becomes:

$$\psi_{n,s}(x) = (\sqrt{2} + \mathcal{O}(e^{-n})) \sin\left(\left[(n+\frac{1}{2})\pi + \mathcal{O}(e^{-\frac{n}{2}})\right] x - \frac{\pi}{4} + \mathcal{O}(e^{-n})\right) \tag{4.45}$$

$$= \sqrt{2} \sin\left((n+\frac{1}{2})\pi x - \frac{\pi}{4}\right) + \mathcal{O}(e^{-\frac{n}{2}})$$

Because x is in form of $\frac{a}{b}$, $\sin((n+\frac{1}{2})\pi\frac{a}{b} - \frac{\pi}{4})$ is periodic as a function of n with a period of $2b$. According to (4.45), $\forall \varepsilon > 0, \exists N_4, \forall n > N_4, |\psi_{n,s}(x) - \sin(((n \mod 2b) + \frac{1}{2})\pi\frac{a}{b} - \frac{\pi}{4})| < \frac{\varepsilon}{2}$. According to (4.44), $\exists N_5, \forall n > N_5$, there is $|\psi_{n,h}(x)| < \frac{\varepsilon}{2}$. As a result, at position $x = \frac{a}{b}$, $\exists N_4, N_5, \forall n > \max(N_4, N_5)$, we have:

$$\left|\psi_{n,s}(x = \frac{a}{b}) \pm \psi_{n,h}(x = \frac{a}{b}) - \sin\left(((n \mod 2b) + \frac{1}{2})\pi\frac{a}{b} - \frac{\pi}{4}\right)\right| < \varepsilon \tag{4.46}$$

Thus, within a given interval $[m - \varepsilon, m + \varepsilon]$, $\frac{n_{m-\varepsilon,m+\varepsilon}}{n}$ tends either to a fixed value while $m = \sin((i+\frac{1}{2})\pi\frac{a}{b} - \frac{\pi}{4}), i \in [\![1, 2b]\!]$ or to 0 for the m elsewise and it is valid both for $\psi_{n,s}(x) + \psi_{n,h}(x)$ and $\psi_{n,s}(x) - \psi_{n,h}(x)$.

The distribution of $x \in \mathbb{Q}$ can also be deduced:

$$\mathscr{D}_{\mathbf{X} = \frac{a}{b} \in \mathbb{Q}}(x) = \begin{cases} \frac{1}{2b} \quad \text{or} \quad \frac{1}{b} & x = \sin((i+\frac{1}{2})\pi\frac{a}{b} - \frac{\pi}{4}), i \in [\![1, 2b]\!] \\ 0 & \text{Elsewise} \end{cases} \tag{4.47}$$

Because a sinusoidal function is not monotonic within one period, it is possible that $\exists i_1 \neq i_2$ and they satisfy $\sin((i_1 + \frac{1}{2})\pi\frac{a}{b} - \frac{\pi}{4}) = \sin((i_2 + \frac{1}{2})\pi\frac{a}{b} - \frac{\pi}{4})$. The value of the distribution at that position should be replaced by $\frac{1}{b}$ instead of $\frac{1}{2b}$.

Case two: while $x \in (0,1) \cap R \setminus \mathbb{Q}$, $(n + \frac{1}{2})\pi x$ are the points on the real axis with equal distance between them. We make a projection from $\mathbb{R}$ to $[0, 2\pi]$ by subtracting a multiplication of 2π to construct a new number set $S = \{(n+\frac{1}{2})\pi x - 2p\pi - \frac{\pi}{4} | n \in \mathbb{Z}, p = \lfloor \frac{(n+\frac{1}{2})x}{2} - \frac{\pi}{4} \rfloor\}$ where $\lfloor x \rfloor$ is the floor function which takes the greatest integer less or equal to x. Thanks to its linearity, if there are two elements $s_1, s_2 \in S$ and noting $\Delta s = s_2 - s_1$, $\forall s_3 \in S$, if $s_3 + \Delta s \in [0, 2\pi]$, it also belongs to S. Then it can also be proved that if there are two segments with a same length on $[0, 2\pi]$, a bijection can be established between elements in S on these two intervals. It implies one can

use the length of the interval as a measure for the number of elements inside this interval.

In order to verify the hypothesis ii., given m_1 and m_2, we have

$$m_1 \leq \sqrt{2}\sin\left((n+\frac{1}{2})\pi x - \frac{\pi}{4}\right) + \mathcal{O}(e^{-\frac{n}{2}}) \leq m_2 \tag{4.48}$$

$$\frac{m_1}{\sqrt{2}} + \mathcal{O}(e^{-\frac{n}{2}}) \leq \sin\left((n+\frac{1}{2})\pi x - \frac{\pi}{4} - 2p\pi\right) \leq \frac{m_2}{\sqrt{2}} + \mathcal{O}(e^{-\frac{n}{2}}) \tag{4.49}$$

$$\arcsin(\frac{m_1}{\sqrt{2}}) + \mathcal{O}(e^{-\frac{n}{2}}) \leq s \leq \arcsin(\frac{m_2}{\sqrt{2}}) + \mathcal{O}(e^{-\frac{n}{2}}), s \in S \tag{4.50}$$

The result given by (4.50) presents only the case while $0 < \arcsin(\frac{m_2}{\sqrt{2}}) < \arcsin(\frac{m_2}{\sqrt{2}}) < \frac{\pi}{2}$ and we can obtain similar results for other monotonic intervals on $[\frac{\pi}{2}, \frac{3\pi}{2}]$ and $[\frac{3\pi}{2}, 2\pi]$. When combining all these solutions, due to the symmetry of the sinusoidal function, the total length of the interval satisfying (4.48) is $2\left(\arcsin(\frac{m_2}{\sqrt{2}}) - \arcsin(\frac{m_1}{\sqrt{2}})\right) + \mathcal{O}(e^{-\frac{n}{2}})$. And finally, $\frac{n_{m_1,m_2}}{n} = \frac{\left(\arcsin(\frac{m_2}{\sqrt{2}}) - \arcsin(\frac{m_1}{\sqrt{2}})\right) + \mathcal{O}(e^{-\frac{n}{2}})}{\pi}$. Similar to previous results, the hyperbolical part is $\mathcal{O}(e^{-n(1-x)}) + \mathcal{O}(e^{-nx})$, which is less than any $\frac{\varepsilon}{2} > 0$ while n is great enough. Thus, $\forall \varepsilon > 0, \exists N_6, \forall n > N_6$,

$$\left| \frac{n_{m_1,m_2}}{n} - \frac{\left(\arcsin(\frac{m_2}{\sqrt{2}}) - \arcsin(\frac{m_1}{\sqrt{2}})\right)}{\pi} \right| < \varepsilon \tag{4.51}$$

According to the definition of $\mathscr{D}_{\mathbf{X}}(x)$ in (4.29). Its value can be obtained by calculating the derivative of $\arcsin(x)$:

$$\mathscr{D}_{\mathbf{X} \in (0,1) \cap \mathbb{R} \setminus \mathbb{Q}}(x) = \frac{\arcsin(x+dx) - \arcsin(x)}{\pi dx} = \frac{1}{\pi\sqrt{1-x^2}} \tag{4.52}$$

Until now, the convergence of $\frac{n_{m_1,m_2}}{n}$ is proved for all $x \in (0,1)$ on $\mathbb{R}$ for both $\psi_{n,s}(x) \pm \psi_{n,h}(x)$.

□

The form of $\mathscr{D}_{\mathbf{X}}(x)$ depends on the nature of the position X, but we still want to have an uniform representation of $\mathscr{D}_{\mathbf{X}}(x)$. We will prove in an integration $\int_{-1}^{1} f(x)\mathscr{D}_{\mathbf{X}=\frac{a}{b} \in (0,1) \cap \mathbb{Q}}(x)dx$ can be replaced by $\int_{-1}^{1} f(x)\frac{1}{\pi\sqrt{1-x^2}}dx$ while $b \to \infty$.

Proof. According to (4.47), as $\mathscr{D}_{\mathbf{X}}(x)$ is a discrete distribution, one can also discretise the integration.

$$\int_{-1}^{1} f(x)\mathscr{D}_{\mathbf{X}=\frac{a}{b} \in (0,1) \cap \mathbb{Q}}(x)dx = \sum_{n=1}^{2b} f(x_n)\frac{1}{2b}\Big|_{x_n=\sin(\frac{n}{b}\pi + \frac{\pi}{2b} - \frac{\pi}{4})} \tag{4.53}$$

Now, replacing $\frac{1}{b}$ by $\frac{\Delta y}{\pi}$ and noting $y_n = n\Delta y$, y_n takes values form 0 to 2π. As it covers an

entire period of a sin function, while $\Delta y = \frac{1}{b} \to 0$, its value is equal to 2 times the value on one monotonic interval of the sin function.

$$
\begin{aligned}
\int_{-1}^{1} f(x) \mathscr{D}_{\mathbf{X} = \frac{a}{b} \in (0,1) \cap \mathbb{Q}}(x) dx &= \sum_{n=1}^{2b} f(\sin(y_n + \frac{1}{2}\Delta y - \frac{\pi}{4})) \frac{\Delta y}{2\pi} \\
&\xlongequal{\Delta y \to 0} \frac{1}{2\pi} \int_{0}^{2\pi} f(\sin(y - \frac{\pi}{4})) dy \\
&= \frac{1}{\pi} \int_{\frac{3\pi}{4}}^{\frac{7\pi}{4}} f(\sin(y - \frac{\pi}{4})) dy \\
&\xlongequal{x = \sin(y - \frac{\pi}{4})} \frac{1}{\pi} \int_{-1}^{1} f(x) d(\arcsin(x) + \frac{\pi}{4}) \\
&= \int_{-1}^{1} f(x) \frac{1}{\pi \sqrt{1 - x^2}} dx
\end{aligned}
\tag{4.54}
$$

As a result, $\mathscr{D}_{\mathbf{X}}(x) = \frac{1}{\pi \sqrt{1-x^2}}$ can be used to calculate the approximate value when it is used in an integration. $\qquad \square$

4.5.3 Conditional distributions

The normalised vibration amplitude formula for the time-reversal method is given by (4.33). The position where the pulse excitation applies is noted as A and the position of the piezo-electric sensor is noted as P. In order to calculate the normalised amplitude, we have to first calculate the conditional distributions.

Conditional distribution $\mathscr{D}_{\mathbf{X}|\mathbf{A}(y)}(x)$

The conditional distribution presents the value distribution of eigenmodes which have a certain value at an other position. For example, $\mathscr{D}_{\mathbf{X}|\mathbf{A}(y)}(x)$ is the distribution of $\psi_{n'}(\mathbf{X})$ for all n' such that the normalised value of $\psi_{n'}(\mathbf{A})$ is equal to y.

According to (4.45) and (4.44), while n is great enough, as proved previously, the error terms in big O will be inferior to a certain level. For simplicity reasons, we will ignore these terms in the following analysis. The normalised (in the meaning of distribution analysis) eigenmodes are:

$$
\bar{\psi}_n(x) = \sin\left((n + \frac{1}{2})\pi x - \frac{\pi}{4}\right)
\tag{4.55}
$$

Noting x_A the position of point A, x_X the position of X and $\Delta x = x_X - x_A$. Because at x_A, $\sin\left((n + \frac{1}{2})\pi x_A - \frac{\pi}{4}\right) = y$, its cosine form has equal probability to be $\pm\sqrt{1 - y^2}$. Let $\theta = \arcsin(y)$, the term inside the sin function: $(n + \frac{1}{2})\pi x_A - \frac{\pi}{4}$ is either equal to $\theta + 2k\pi$ or $\pi - \theta + 2k\pi$

where $k \in \mathbb{Z}$. The normalised amplitude at position X can be written in:

$$\bar{\psi}_n(x_X) = \sin\left((n+\frac{1}{2})\pi(x_A + \Delta x) - \frac{\pi}{4}\right) = \begin{cases} \sin\left((n+\frac{1}{2})\pi\Delta x + \theta\right) \\ \sin\left((n+\frac{1}{2})\pi\Delta x + \pi - \theta\right) \end{cases} \tag{4.56}$$

$\psi_n(x_X)$ has an equal probability to take one of the above expressions. The development of each expression to calculate its value distribution is similar to the method used in the proof of convergence of $\frac{n_{m_1,m_2}}{n}$ and $\mathscr{D}_{\mathbf{X}}(x)$. It is necessary to discuss the cases whether Δx is a rational number or not and it will deduce the same result. Finally, combining the two possibilities and taking into account only the integration approximation form, we have:

$$\mathscr{D}_{\mathbf{X}|\mathbf{A}(y)}(x) = \frac{1}{\pi\sqrt{1-x^2}} \tag{4.57}$$

Conditional distribution $\mathscr{D}_{\mathbf{X}|\mathbf{A}(y),\mathbf{P}(p)}(x)$

The index $\mathbf{A}(y), \mathbf{P}(p)$ means the eigenmodes have a normalised amplitude of y at position A and a normalised amplitude of p at position P. Noting $s_n(x) = (n+\frac{1}{2})\pi x - \frac{\pi}{4}$, according to (4.55), the conditions for the conditional distribution can be translated into the following equations:

$$\sin\left((n+\frac{1}{2})\pi x_A - \frac{\pi}{4}\right) = \sin(s_n(x_A)) = y, \quad \cos(s_n(x_A)) = \pm\sqrt{1-y^2} \tag{4.58a}$$

$$\sin\left((n+\frac{1}{2})\pi x_P - \frac{\pi}{4}\right) = \sin(s_n(x_P)) = p, \quad \cos(s_n(x_P)) = \pm\sqrt{1-p^2} \tag{4.58b}$$

The cos value for these positions has equal probability to take the sign $+$ or $-$.

In order to study the value distribution at position X, the dependency between $s_n(x_A)$, $s_n(x_P)$ and $s_n(x_X)$ is important. If $s_n(x_X)$ can be presented by a linear combination of $s_n(x_A)$ and $s_n(x_P)$ the amplitude value will depend only on y and p. Otherwise, one must introduce a new parameter Δx to describe its position related to a known point, which will drop into the same case when we analysed $\mathscr{D}_{\mathbf{X}|\mathbf{A}(y)}(x)$. The distribution function can be represented as (4.59) if it presents in an integration form.

$$\mathscr{D}_{\mathbf{X}\notin\{aA+bP|a,b\in\mathbb{Z}\}|\mathbf{A}(y),\mathbf{P}(p)}(x) = \frac{1}{\pi\sqrt{1-x^2}} \tag{4.59}$$

For the case where $s_n(x_X)$ can be presented by $as_n(x_A) \pm bs_n(x_P)$, we have:

$$\psi_{\mathbf{X},a,\pm b} = \sin(as_n(x_A) \pm bs_n(x_P)) \tag{4.60}$$

$$= \sin(as_n(x_A))\cos(bs_n(x_P)) \pm \sin(bs_n(x_P))\cos(as_n(x_A))$$

$$= \begin{cases}
(-1)^{\frac{a-1}{2}} T_a(\sin(s_n(x_A)))(-1)^{\frac{b-1}{2}}\cos(s_n(x_P))U_{b-1}(\sin(s_n(x_P))) \\
\qquad \pm (-1)^{\frac{b-1}{n}} T_b(\sin(s_n(x_P)))(-1)^{\frac{a-1}{2}}\cos(s_n(x_A))U_{a-1}(\sin(s_n(x_A))) \\
\qquad\qquad\qquad\qquad\qquad\qquad \text{for } a \text{ odd and } b \text{ odd} \\[4pt]
(-1)^{\frac{a}{2}-1}\cos(s_n(x_A))U_{a-1}(\sin(s_n(x_A)))(-1)^{\frac{b}{2}} T_b(\sin(s_n(x_P))) \\
\qquad \pm (-1)^{\frac{b}{2}-1}\cos(s_n(x_P))U_{b-1}(\sin(s_n(x_P)))(-1)^{\frac{a}{n}} T_a(\sin(s_n(x_A))) \\
\qquad\qquad\qquad\qquad\qquad\qquad \text{for } a \text{ even and } b \text{ even} \\[4pt]
(-1)^{\frac{a-1}{2}} T_a(\sin(s_n(x_A)))(-1)^{\frac{b}{2}} T_b(\sin(s_n(x_P))) \\
\pm (-1)^{\frac{b}{2}-1}\cos(s_n(x_P))U_{b-1}(\sin(s_n(x_P)))(-1)^{\frac{a-1}{2}}\cos(s_n(x_A))U_{a-1}(\sin(s_n(x_A))) \\
\qquad\qquad\qquad\qquad\qquad\qquad \text{for } a \text{ odd and } b \text{ even} \\[4pt]
(-1)^{\frac{a}{2}-1}\cos(s_n(x_A))U_{a-1}(\sin(s_n(x_A)))(-1)^{\frac{b-1}{2}}\cos(s_n(x_P))U_{b-1}(\sin(s_n(x_P))) \\
\qquad \pm (-1)^{\frac{b-1}{n}} T_b(\sin(s_n(x_P)))(-1)^{\frac{a}{n}} T_a(\sin(s_n(x_A))) \\
\qquad\qquad\qquad\qquad\qquad\qquad \text{for } a \text{ even and } b \text{ odd}
\end{cases}$$

where T_n is a Chebyshev polynomial of the first kind and U_n is a Chebyshev polynomial of the second kind.

As given in (4.58) the cos values of $x_n(X_A)$ and $x_n(X_P)$ have equal probability to be positive or negative. In (4.60), $\psi_{\mathbf{X},a,\pm b}$ has equal chance for different values. For example, if a is odd and b is odd, we have:

$$\mathscr{D}_{\mathbf{X}\in\{aA+bP|a\text{ odd},b\text{ odd}\}|\mathbf{A}(y),\mathbf{P}(p)}(x) \tag{4.61}$$

$$= \begin{cases}
\frac{1}{4} & x = (-1)^{\frac{a-1}{2}} T_a(y)(-1)^{\frac{b-1}{2}}\sqrt{1+p^2}U_{b-1}(p) \pm (-1)^{\frac{b-1}{n}} T_b(p)(-1)^{\frac{a-1}{2}}\sqrt{1-y^2}U_{a-1}(y) \\
\frac{1}{4} & x = (-1)^{\frac{a-1}{2}} T_a(y)(-1)^{\frac{b-1}{2}}\sqrt{1+p^2}U_{b-1}(p) \mp (-1)^{\frac{b-1}{n}} T_b(p)(-1)^{\frac{a-1}{2}}\sqrt{1-y^2}U_{a-1}(y) \\
\frac{1}{4} & x = (-1)^{-\frac{a-1}{2}} T_a(y)(-1)^{\frac{b-1}{2}}\sqrt{1+p^2}U_{b-1}(p) \pm (-1)^{\frac{b-1}{n}} T_b(p)(-1)^{\frac{a-1}{2}}\sqrt{1-y^2}U_{a-1}(y) \\
\frac{1}{4} & x = (-1)^{-\frac{a-1}{2}} T_a(y)(-1)^{\frac{b-1}{2}}\sqrt{1+p^2}U_{b-1}(p) \mp (-1)^{\frac{b-1}{n}} T_b(p)(-1)^{\frac{a-1}{2}}\sqrt{1-y^2}U_{a-1}(y)
\end{cases}$$

Expression (4.61) is symmetric about the axis $x = 0$, thus it is an even function. The same case applies for a and b having the same parity. If a is odd and b is even, the distribution is no longer symmetric about $x = 0$, like the expression given in (4.62) which is symmetric about $x = (-1)^{\frac{a-1}{2}} T_a(y)(-1)^{\frac{b}{2}} T_b(p)$.

$$\mathscr{D}_{\mathbf{X}\in\{aA+bP|a\text{ odd},b\text{ even}\}|\mathbf{A}(y),\mathbf{P}(p)}(x) \tag{4.62}$$

$$= \begin{cases}
\frac{1}{2} & x = (-1)^{\frac{a-1}{2}} T_a(y)(-1)^{\frac{b}{2}} T_b(p) \pm (-1)^{\frac{b}{2}-1}\sqrt{1-p^2}U_{b-1}(p)(-1)^{\frac{b-1}{2}}\sqrt{1-y^2}U_{b-1}(y) \\
\frac{1}{2} & x = (-1)^{\frac{a-1}{2}} T_a(y)(-1)^{\frac{b}{2}} T_b(p) \mp (-1)^{\frac{b}{2}-1}\sqrt{1-p^2}U_{b-1}(p)(-1)^{\frac{b-1}{2}}\sqrt{1-y^2}U_{b-1}(y)
\end{cases}$$

A similar result can be obtained while a is even and b is odd.

4.5.4 Normalised amplitude

Once all expressions of distribution are obtained, the amplitude can be easily calculated according to (4.33).

Firstly, the most interesting point is at position A, where the excitation pulse applies. We can directly apply (4.34) with (4.54) and (4.57).

$$w_{\mathbf{A}|_{\mathbf{A}}^{\mathbf{P}}} = \iint_{-1}^{1} y^2 p^2 \mathscr{D}_{\mathbf{A}}(y)\mathscr{D}_{\mathbf{P}|\mathbf{A}(y)}(p)dydp = \iint_{-1}^{1} y^2 p^2 \frac{1}{\pi\sqrt{1-y^2}}\frac{1}{\pi\sqrt{1-p^2}}dydp \qquad (4.63)$$

$$= \int_{-1}^{1} \frac{y^2}{\pi\sqrt{1-y^2}}dy \int_{-1}^{1} \frac{p^2}{\pi\sqrt{1-p^2}}dp = \frac{1}{4}$$

The normalised amplitude using time reversal method at position A is $\frac{1}{4}$.

Secondly, we will calculate positions which do not meet the linear combination condition for A and P such that $\mathbf{X} \notin \{aA + bP | a, b \in \mathbb{Z}\}$. According to (4.54), (4.57) and (4.59), the normalised amplitude (4.33) becomes:

$$w_{\mathbf{X}\notin\{aA+bP|a,b\in\mathbb{Z}\}|_{\mathbf{A}}^{\mathbf{P}}} = \iiint_{-1}^{1} xyp^2 \mathscr{D}_{\mathbf{A}}(y)\mathscr{D}_{\mathbf{P}|\mathbf{A}(y)}(p)\mathscr{D}_{\mathbf{X}\notin\{aA+bP|a,b\in\mathbb{Z}\}|\mathbf{A}(y),\mathbf{P}(p)}(x)dydpdx$$

$$(4.64)$$

$$= \iiint_{-1}^{1} xyp^2 \frac{1}{\pi\sqrt{1-y^2}}\frac{1}{\pi\sqrt{1-p^2}}\frac{1}{\pi\sqrt{1-x^2}}dydpdx$$

$$= \int_{-1}^{1} \frac{y}{\pi\sqrt{1-y^2}}dy \int_{-1}^{1} \frac{p^2}{\pi\sqrt{1-p^2}}dp \int_{-1}^{1} \frac{x}{\pi\sqrt{1-x^2}}dx$$

$$= 0$$

which implies zero displacement at these positions.

Thirdly, we consider the case where $\mathbf{X} \in \{aA + bP | a, b \in \mathbb{Z}\}$ and a and b are both even or both odd.

$$w_{\mathbf{X}\in\{aA+bP|a,b \text{ same parity}\}|_{\mathbf{A}}^{\mathbf{P}}} \qquad (4.65)$$

$$= \iiint_{-1}^{1} xyp^2 \mathscr{D}_{\mathbf{A}}(y)\mathscr{D}_{\mathbf{P}|\mathbf{A}(y)}(p)\mathscr{D}_{\mathbf{X}\in\{aA+bP|a,b \text{ same parity}\}|\mathbf{A}(y),\mathbf{P}(p)}(x)dydpdx$$

$$= \iint_{-1}^{1} \frac{y}{\pi\sqrt{1-y^2}}\frac{p^2}{\pi\sqrt{1-p^2}} \int_{-1}^{1} x\mathscr{D}_{\mathbf{X}\in\{aA+bP|a,b \text{ same parity}\}|\mathbf{A}(y),\mathbf{P}(p)}(x)dxdydp$$

$$= 0$$

As discussed for (4.61), if a and b have the same parity, (4.60) will give an even function $\mathscr{D}(x)$.

65

$x\mathscr{D}(x)$ is odd and its integration on $[1,1]$ is 0, therefore, the amplitude is 0.

Fourthly, if a is odd and b is even. The distribution function $\mathscr{D}(x)$ shown in (4.62) is now symmetric to $x = (-1)^{\frac{a-1}{2}} T_a(y)(-1)^{\frac{b}{2}} T_b(p)$.

$$\int_{-1}^{1} x\mathscr{D}_{\mathbf{X}\in\{aA+bP|a\,\mathrm{odd},b\,\mathrm{even}\}|\mathbf{A}(y),\mathbf{P}(p)}(x) \tag{4.66}$$

$$=\frac{1}{2}\left((-1)^{\frac{a-1}{2}} T_a(y)(-1)^{\frac{b}{2}} T_b(p) \pm (-1)^{\frac{b}{2}-1}\sqrt{1-p^2}U_{b-1}(p)(-1)^{\frac{b-1}{2}}\sqrt{1-y^2}U_{b-1}(y)\right)$$

$$+\frac{1}{2}\left((-1)^{\frac{a-1}{2}} T_a(y)(-1)^{\frac{b}{2}} T_b(p) \mp (-1)^{\frac{b}{2}-1}\sqrt{1-p^2}U_{b-1}(p)(-1)^{\frac{b-1}{2}}\sqrt{1-y^2}U_{b-1}(y)\right)$$

$$=(-1)^{\frac{a-1}{2}} T_a(y)(-1)^{\frac{b}{2}} T_b(p)$$

The normalised amplitude is then:

$$w_{\mathbf{X}\in\{aA+bP|a\,\mathrm{odd},b\,\mathrm{even}\}|_{\mathbf{A}}^{\mathbf{P}}} \tag{4.67}$$

$$=\iint_{-1}^{1}\frac{y}{\pi\sqrt{1-y^2}}\frac{p^2}{\pi\sqrt{1-p^2}}\int_{-1}^{1} x\mathscr{D}_{\mathbf{X}\in\{aA+bP|a\,\mathrm{odd},b\,\mathrm{even}\}|\mathbf{A}(y),\mathbf{P}(p)}(x)dxdydp$$

$$=\iint_{-1}^{1}\frac{y}{\pi\sqrt{1-y^2}}\frac{p^2}{\pi\sqrt{1-p^2}}(-1)^{\frac{a-1}{2}} T_a(y)(-1)^{\frac{b}{2}} T_b(p)dydp$$

According to [68], y and p^2 can be written in Chebyshev polynomials of the first kind.

$$y = T_1(y) \tag{4.68a}$$

$$p^2 = \frac{1}{2}(2p^2 - 1 + 1) = \frac{1}{2}(T_2(p) + T_0(p)) \tag{4.68b}$$

Noticing their orthogonality properties, the Chebyshev polynomials of the first kind satisfy the following relation [68]:

$$\int_{-1}^{1}\frac{T_n(x)T_m(x)}{\sqrt{1-x^2}}dx = \begin{cases} 0 & n \neq m \\ \pi & n = m = 0 \\ \frac{\pi}{2} & n = m \neq 0 \end{cases} \tag{4.69}$$

Taking (4.68) into (4.67):

$$w_{\mathbf{X}\in\{aA+bP\,|\,a\ \text{odd},b\ \text{even}\}|_{\mathbf{A}}^{\mathbf{P}}} \tag{4.70}$$

$$= \int_{-1}^{1} (-1)^{\frac{a-1}{2}} \frac{T_1(y)\,T_a(y)}{\pi\sqrt{1-y^2}}\,dy \int_{-1}^{1} (-1)^{\frac{b}{2}} \frac{\frac{1}{2}(T_2(p)+T_0(p))\,T_b(p)}{\pi\sqrt{1-p^2}}\,dp$$

According to the orthogonality of the Chebyshev polynomials, the above normalised amplitude is not equal to zero only if $a = \pm1$ and $b = 0$ or ±2.

- If $a = 1$ and $b = 0$ which means $x_X = x_A$, it is the same as the first case for (4.63). Moreover, according to (4.69) and (4.70), $w_{\mathbf{X}\in\{1A+0P\}|_{\mathbf{A}}^{\mathbf{P}}} = \frac{1}{2} \times \frac{1}{2} = \frac{1}{4}$, which is coherent to previous result.

- If $a = -1$ and $b = 0$, because of the constant term $-\frac{\pi}{4}$ appearing in $s_n(x)$, there is no position X on $[0,1]$ which can guarantee for all n there is the relation $\sin(s_n(x_X)) = \sin(-s_n(x_A))$. However, the expression could be established if $\sin(s_n(x_X)+\pi) = -\sin(s_n(x_A))$. It is related to the second derivative of the amplitude of eigenmodes at position X. The second derivative of eigenmodes can be presented by $\frac{d^2\bar\psi_n(x)}{dx^2} = -k_n'^{\,2}\sin(k_n'x - \frac{\pi}{4})$. As the symmetric point of its conditional distribution function is not at zero. It will take a significant value, which is coherent to the fact that at x_A there is a peak value for the amplitude.

- If $a = -1$ and $b = 2$, $x_X = 2x_P - x_A$, which is the reflection symmetric position of A to P. According to the definition, $\psi_{\mathbf{X},-a,b} = -\psi_{\mathbf{X},a,-b}$. Its amplitude is then $w_{\mathbf{X}\in\{-1A+2P\}|_{\mathbf{A}}^{\mathbf{P}}} = -\frac{1}{2} \times (-1)\frac{1}{4} = \frac{1}{8}$.

- If $a = 1$ and $b = -2$, it is similar to the case while $a = -1$. It corresponds to the second derivative at $x_X = 2x_P - x_A$, which is not zero due to the peak at this position.

- If $a = 1$ and $b = 2$, similar to previous analysis, there is no $s_n(x_X) = s_n(x_A) + 2s_n(x_P)$ for all n. However, it can be reformulated to $\sin(s_n(x_A) + 2s_n(x_P)) = \sin(s_n(x_X) + \frac{\pi}{2}) = \cos(s_n(x_X))$. It corresponds to the first derivative of $\bar\psi_n(x)$ at $x_X = x_A + 2x_P$ and it has a non-zero value at this position.

  Indeed, since $\sin(s_n(x_X)) = \cos(s_n(x_A) + 2s_n(x_P))$, the normalised amplitude value at $x_X = x_A + 2x_P$ can be calculated using the cosine version of (4.60), which can be proved to be always zero for the amplitude obtained by the integration with distribution functions.

- If $a = -1$ and $b = -2$, it is related to the third derivative of $\bar\psi_n(x)$ at $x_X = x_A + 2x_P$.

- Because x_P and x_A are defined on $[0, 1]$, $2x_P - x_A$ can be inferior to zero, one can calculate the amplitude at $x_{X'} = -(2x_P - x_A)$ such that $\sin(-(2s_n(x_P) - s_n(x_A))) = \sin(s_n(x_{X'}) + \frac{\pi}{2}) = \cos(s_n(x_{X'}))$. Similar to the case of $a = 1$ and $b = 2$, it will give a non zero result for the first order derivative of $\sin(s_n(x_{X'}))$.

- Otherwise, if $x_X = x_A + 2x_P > 0$, $x_{X''} = 2 - (x_A + 2x_P)$ can be studied in order to let $x_{X'}$ remain in the range of $[0, 1]$. Then, we have $-\sin(2s_n(x_P) + s_n(x_A)) = \sin(2n\pi - (2(n - \frac{1}{2})\pi x_P + (n - \frac{1}{2})\pi x_A - \frac{3}{4})) = \sin(2n\pi - \pi - (n - \frac{1}{2})\pi(2x_P + x_A) - \frac{1}{4}) = \sin(s_n(x_{X''}))$ and a peak of $\frac{1}{4}$ will be found at that position.

Fifthly, if a is even and b is odd, we will find an expression similar to (4.70). Because a is even, $a \neq 1$. According to the orthogonality, the integration containing $T_1(y)T_a(y)$ on [-1,1] is aways equal to zero. Thus the amplitude in this case is always zero.

In brief, the above analysis gives a theoretical calculation of the normalised amplitude on an ideal beam obtained by the time reversal method. The amplitude is nearly zero everywhere except at three positions:

1. At $x_X = x_A$, the normalised amplitude is $\frac{1}{8}$

2. At $x_{X'} = 2x_P - x_A \in [0, 1]$, the normalised amplitude is $\frac{1}{4}$ or at $x_{X'} = -2x_P + x_A \in [0, 1]$, the normalised amplitude is zero, but its first order derivative is not zero, which leads to a positive peak and a negative peak around this position.

3. At $x_{X''} = x_A + 2x_P \in [0, 1]$, the normalised amplitude is zero, but the first order derivative at that position is not zero, which leads to a positive peak and a negative peak around this position or $x_{X''} = 2 - (x_A + 2x_P) \in [0, 1]$ the normalised amplitude is $\frac{1}{4}$

4.5.5 Numerical application

Although the theoretical analysis considers the case while n tends to infinity, a numerical application with limited n can still give approximate results to help to visualise the maximum vibration amplitude of an ideal beam.

The first experiment is provided with the first 360 eigenmodes of an ideal beam of length $L = 1$. Supposing the piezoelectric sensor is positioned at $x_P = 0.25$ and the excitation pulse is applied at position $x_A = 0.4$. The result is obtained by directly summing (4.35) and then dividing by a normalisation factor. According to the theoretical results of the time reversal method for a beam, we should find a maximal pulse at $x_{X_1} = x_A = 0.4$, its normalised amplitude is equal to $\frac{1}{4}$. A second pulse at $x_{X_2} = 2x_P - x_A = 0.1$ of $\frac{1}{8}$. And at $x_{X_3} = 2x_P + x_A = 0.9$, we will observe a zero point with two peak values around it.

The result is given in Fig. 4.4, because n is limited, there are variations of amplitude and they are more important around peaks. The numerical value gives the same value (four decimal numbers) as the value predicted by the theoretical analysis.

Let's suppose the beam's length is 25 times greater than the size of the piezoelectric sensor. Section 4.2 presented that the vibration-to-voltage relation is available only if the half wavelength
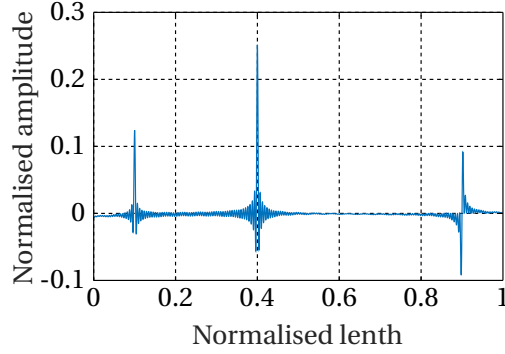
Figure 4.4 – Theoretical time reversal result with 360 eigenmodes. $x_A = 0.4$, $x_P = 0.25$

is greater than the size of the piezoelectric element.

$$\frac{\lambda}{2} \approx \frac{\pi}{k'_n} = \frac{\pi}{(n - \frac{1}{2})\pi} > \frac{1}{25} \tag{4.71}$$

Above inequality (4.71) gives the relation between the wavenumber and the size multiplier. The maximum eigenmode number n is 25.
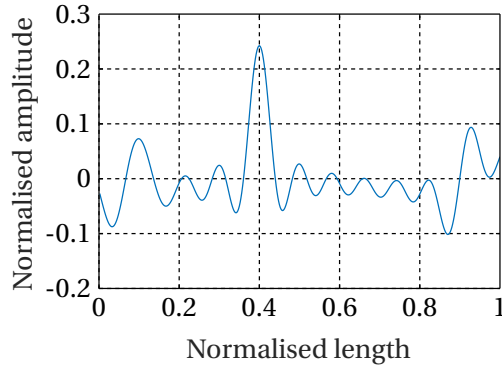
Figure 4.5 – Theoretical time reversal result with 25 eigenmodes. $x_A = 0.4$, $x_P = 0.25$

As shown in Fig. 4.5, if n is small, all components of high frequency are eliminated. The restored excitation pulse becomes much larger. At x_{X_3} the distance of two opposite peak is also equal to the shortest wavelength. The amplitude of the main peaks (at x_{X_1}) is 0.241, and the amplitude of the associated peak (at x_{X_2}) becomes 0.073. One can observe the amplitude decreases due to the reduction of the number of eigenmodes used for the calculation.

Supposing the position of the piezoelectric sensor is fixed at $x_P = 0.25$, we can obtain the time reversal results by repeating the experiments for different excitation pulse positions. Fig. 4.6 presents the numerical results as a function of the position of excitation pulses with 25 eigenmodes.
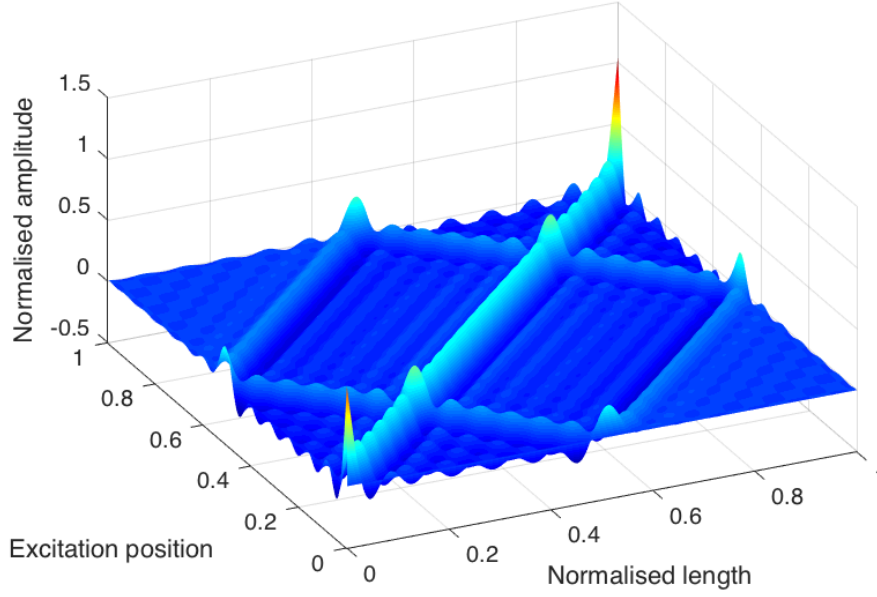
Figure 4.6 – Theoretical time reversal result with a sensor at $x_P = 0.25$

The diagonal peaks shows the time reversal method can restore the excitation at right positions. Lines which form a rectangle in the graph are related to $l_1(x_A) = 2x_P + x_A$, $l_2(x_A) = 2 - (2x_P + x_A)$, $l_3(x_A) = 2x_P - x_A$ and $l_3(x_A) = -(2x_P - x_A)$.

At position $x_A = x_P$, the main restored pulse is coincident with the associated pulse. Theoretically, its amplitude becomes $\frac{3}{8}$ and in this graph it is 0.360. The difference is also due to the reduction of the number of eigenmodes.

4.5.6 Guidelines for the excitation pulse position detection of a beam

As predicted by the theoretical analysis, while using the time reversal method to find out excitation pulse positions, simulations result in multiple peaks. Normally, it is sufficient to check the maximum peak, but, in case of multiple excitation sources, it is necessary to consider all the peaks information.

Examining the source position requires firstly the following parameters: position of the piezo x_P and size of the piezoelectric element a. In case of single excitation source, supposing a maximal value is found at position x_M, then x_M is the position of the original excitation. Of course, there will be associated peaks but with less important amplitudes.

In case of multiple excitations at the same time, supposing we detected multiple local maximal at positions $x_1 ... x_n$. The positions of excitation should satisfy that a linear combination of the excitation pulse responses (shown in Fig. 4.6) can restore these peaks (or in the meaning of least mean squares).

4.6 Conclusion

The whole process of using the time reversal method has been studied analytically in this chapter. The interactive relation between a plate and piezoelectric sensor/actuator has been modelled, which introduced a second spatial derivative term to the amplitude result and will reduce the angular frequency on the denominator. The fact of using piezoelectric actuators allows having a response more similar to the original response. Thus it is a better way for the application of the time reversal method compared to previous methods using directly the measured displacement.

Then a mathematical method has been proposed to solve the problem of calculating the amplitude on the plate. If the eigenmodes can satisfy all hypotheses, a distribution of the eigenmode amplitude values can be found out for each position. With these distributions, it is easy to calculate the average normalised amplitude at each position.

An application of the proposed method has been given for an ideal beam as an example. The calculation has been detailed for each step: solution of eigenmodes, verification of hypotheses, calculation of distribution functions and finally amplitudes of each position. The results have shown that for an ideal beam, the restored amplitude by the time reversal method will theoretically have four peaks on the beam. The greatest one is exactly at the same position where the original excitation is applied. An associated one is of half amplitude of the main peak and its position is at $x_{X_2} = 2x_P - x_A$ where x_P is the position of the piezoelectric element and x_A is the position of original excitation. If $2x_P - x_A < 0$, at $x_{X_2} = -(2x_P - x_A)$, two peaks will be found around this position.Similarly, two peaks will be found around the positions $x_{X_3} = 2x_P + x_A$ or one peak at $x_{X_3} = 2 - (2x_P + x_A)$. At the end, a short guideline is given for the detection of the excitation position on a beam based on the pattern of amplitudes.

Relative publications to the chapter

- X. Liu, Y. Civet and Y. Perriard, "Piezoelectric tactile device feedback generator using acoustic time reversal method," *2016 19th International Conference on Electrical Machines and Systems (ICEMS)*, Chiba, 2016, pp. 1-5.

5 Pulse generation on a beam

Contents

This chapter discusses the necessary steps for creating a spatial pulse vibration on a beam as example. Firstly, the peak on the beam according to time reversal method can be modelled by two functions. It allows the theoretical analysis for the reduction of associated peaks. Then, it can be proved that with one or multiple piezoelectric actuator and if their positions can satisfy certain conditions, all the associated peaks can be cancelled out. An optimised actuator arrangement can be then realised. Finally, The damping factor is taken into account. The amplitude coefficient should be adjusted mode by mode in order to restore a perfect pulse vibration.

5.1   Introduction

An ideal generated pulse should be in form of a Dirac function, which can be used then to construct any arbitrary functions. According to the response of an excitation pulse using the time reversal method, one can obtain a vibration with one main peak and several associated peaks. It is sufficient to detect the source position, but not enough for the pulse creation. This is why we should find a method to remove all associated peaks to make the time reversal method applicable for the wave creation.

The idea to improve a time reversal response is to combine multiple responses in order to cancel out the associated peaks. In the previous chapter, we only have demonstrated the existence (positions) of the peaks. If we want to remove them by themselves, it is necessary to represent them mathematically. Fortunately, the function of the peaks can be found in form of a Sinc function, which permits to analytically study where and how to combine different responses to cancel out associated peaks.

The position of the piezoelectric actuator is also proved to be important for the creation of pulses on a beam. The general rule can be obtained form the position solution of associated peaks. The arrangement of multiple piezoelectric actuator will also be intruduced.

As noticed in (4.24), the final amplitude not only depends on eigenmodes related terms but also on a damping term. All the analytical results are obtained while there is only eigenmodes related terms. Thus it is necessary to weight all damping term to a "unitary one" for each mode. The detail will be given at the end of this chapter.

5.2   Amplitude pattern and approximate function

According to Section 4.5.4, the time reversal result of an excitation pulse on a beam contains a main peak and several associated peaks. As a single peak is primarily preferred in applications, the idea to improve the time reversal result is to use a combination of these time reversal responses to cancel out associated peaks. According to Fig. 4.4 and Fig. 4.5, the number of eigenmodes plays an important role for the "variation" of the amplitude obtained. It can be also noticed that for the position where the first oder derivative is non-zero, the distance between that position and its closest peak depends on the number of eigenmodes. In oder to remove them correctly, the first thing is to find out mathematical expressions in function of the number of eigenmodes for these peaks.

According to Appendix B, it can be demonstrated that given an integer n, the first $n-1$ terms of the projection of $\frac{\sin(k_n(x-x_A))}{\pi(x-x_A)}$ on the basis generated by eigenmodes of a beam are almost equal to the first $n-1$ terms of the projection of $\delta(x-x_A)$ on the same basis. Its nth projection is half of the nth projection of the delta function. Its projections with index above n is equal to zero. Thus, given a limited number of eigenmodes to reconstruct an excitation pulse, the result vibration amplitude can be approximated by a Sinc function.

According to this result, one can guess the function for the peak with the presence of a piezoelectric sensor can also be approximated by a Sinc function, but with a normalised amplitude of $\frac{1}{4}$ for the main peak and $\frac{1}{8}$ for the associated peaks. The function of the main peak at $x_{X_1} = x_A$ can be then written as:

$$w_{1,\mathbf{A}}(x) = \frac{\sin(k_n(x - x_{X_1}))}{4k_n(x - x_{X_1})} \tag{5.1}$$

Similarly, for the associated peaks at positions $x_{X_2} = 2x_P - x_A$ and $x_{X_3} = 2 - (2x_P + x_A)$ (while they are on $[0,1]$), the approximate function can be written as:

$$w_{2,\mathbf{A}}(x) = \frac{\sin(k_n(x - x_{X_2}))}{8k_n(x - x_{X_2})} \tag{5.2}$$

$$w_{3,\mathbf{A}}(x) = \frac{\sin(k_n(x - x_{X_3}))}{8k_n(x - x_{X_3})} \tag{5.3}$$

For the associated peaks at positions $x_{X_2} = -(2x_P - x_A)$ and $x_{X_3} = 2x_P + x_A$, we can theoretically find a zero amplitude at that positions with a non zero first-order derivative. The latter implies two opposite peaks around this position. It should be a locally odd function for presenting these peaks. Inspired by the approximate form of the peaks given in (5.1), we find out a function which is able to describe this pattern:

$$w_{2,\mathbf{A}}(x) = -\frac{1 - \cos(k_n(x - x_{X_2}))}{8k_n(x - x_{X_2})} \tag{5.4}$$

$$w_{3,\mathbf{A}}(x) = \frac{1 - \cos(k_n(x - x_{X_3}))}{8k_n(x - x_{X_3})} \tag{5.5}$$

Given n, the approximate function of the normalised amplitude using time reversal method can be presented by the sum of $w_{1,A}(x)$, $w_{2,A}(x)$ and $w_{3,A}(x)$

$$w_{\mathbf{X}|_{\mathbf{A}}^{\mathbf{P}}} \approx w_{1,\mathbf{A}}(x) + w_{2,\mathbf{A}}(x) + w_{3,\mathbf{A}}(x) \tag{5.6}$$

The comparison of the approximate function and the sum of eigenmodes is given in Fig. 5.1. The approximate form can indeed represent the sum of eigenmodes. The peaks of the two functions are almost superimposed. These two examples only showed the results at specific positions, however, because the approximate functions are found by chance, the errors for all possible cases should be examined.

The relative error is plotted in Fig. 5.2. According to the hypothesis for the approximation function presented in Section 4.5.4, the hyperbolical part of the eigenmode expression was ignored. This could explain the important relative errors at two ends of the beam in Fig. 5.2a. As the number of eigemodes increases, the relative error becomes smaller. Fig. 5.2b is a zoom of

(a) The number of eigenmodes is 360

(b) The number of eigenmodes is 25
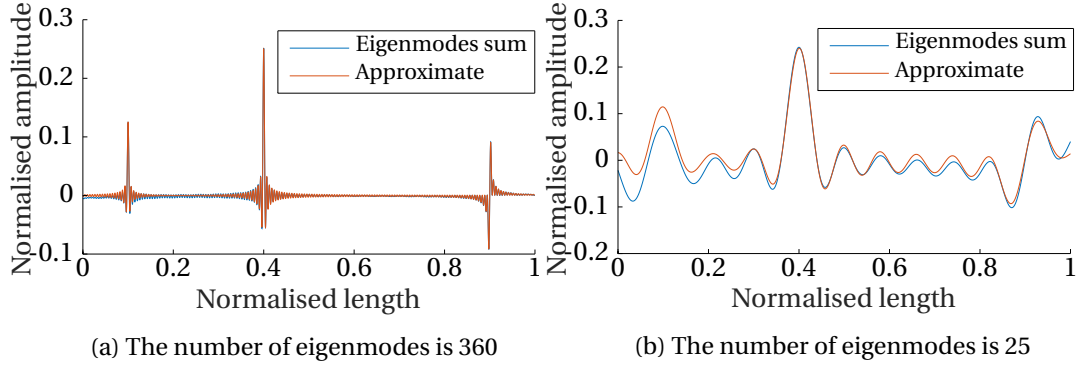
Figure 5.1 – Comparison of theoretical time reversal result with limited number of eigenmodes and its approximate form. $x_A = 0.4, x_P = 0.25$

(a) Eigenmodes number from 5 to 60 and normalised position from 0.01 to 0.99

(b) Eigenmodes number from 20 to 40 and normalised position from 0.1 to 0.9
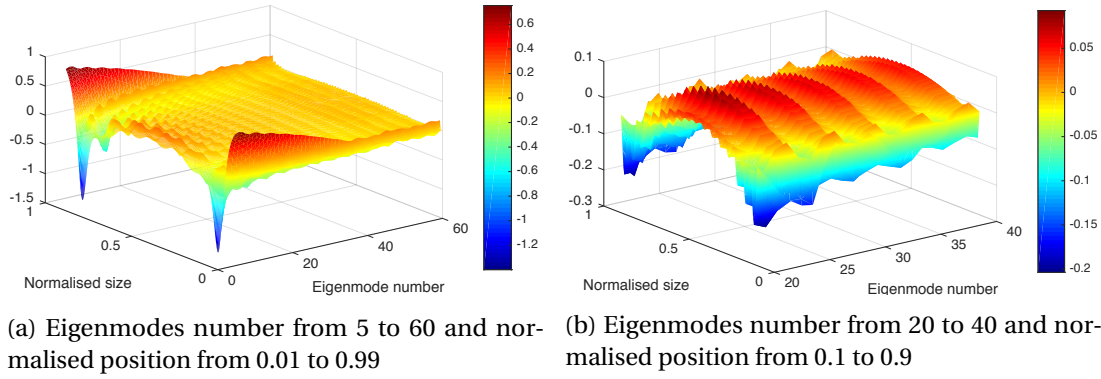
Figure 5.2 – Amplitude relative error between the sum of eigenmodes and the approximate function $x_P = 0.25$

the central part. We can notice firstly the relative error at a same normalised position decreases as n increases. Secondly, the relative error is periodic. For $n = 4k + 1, k \in \mathbb{Z}$. The relative error between the eigenmodes sum and the approximate function has a local minimum value.
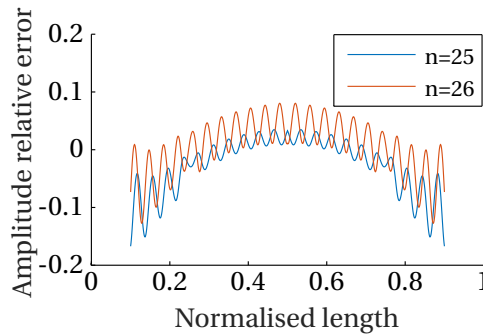
Figure 5.3 – Relative error in function of normalised length for $n = 25$ and $n = 26$

In order to have a better result, we need an approximate function which has less error possible.

Despite of the global trends of the relative error, locally, the choice of n is also important for the effectiveness of the approximation function. As shown in Fig. 5.3, relative errors in function of normalised length for two neighbour n are plotted. One can notice that it is much smaller for $n = 25$ compared to the result of $n = 26$, although 26 is greater than 25. As n depends mainly on the geometry of the beam and the size of the piezoelectric actuator as introduced in Section 4.2, it can lead an optimisation for the size of the structure when applying the above approximate function.

According to (4.71), we have chosen a geometry which implies $n = 25$. It can guarantee an relative error around 5% at the middle of the beam and about 15% at $x = 0.1$.

5.3 Cancellation of associated peaks

The associated peaks can be classified in two categories: the first kind is a simple peak which can be described by (5.2) and (5.3); the second kind is one pair of opposite peaks which can be represented by (5.4) and (5.5). In this section, cancellation methods for the removal of these two kinds of peaks will be firstly presented. Then, the case using one piezoelectric actuator to remove all associated peaks will be introduced. Finally, the case using multiple piezoelectric actuators will be also discussed.

5.3.1 Cancellation of first kind of associated peaks

Because the first kind of associated peaks and the main peak share the same function type for their approximate functions, one can introduce another excitation pulse response whose maximal peak takes place at the same position as this associated peak.

At position x_{X_2}, if there is a first kind of associated peaks, the normalised excitation pulse response needed to cancel this peak is then:

$$w_{\mathbf{X}|_{\mathbf{X}_2}^{\mathbf{P}}} \approx w_{1,\mathbf{X}_2}(x) + w_{2,\mathbf{X}_2}(x) + w_{3,\mathbf{X}_2}(x) \tag{5.7}$$

where

$$w_{1,\mathbf{X}_2}(x) = \frac{\sin(k_n(x - x_{X_{21}}))}{4k_n(x - x_{X_{21}})} \qquad x_{X_{21}} = x_{X_2} \tag{5.8a}$$

$$w_{2,\mathbf{X}_2}(x) = \begin{cases} \frac{\sin(k_n(x-x_{X_{22}}))}{8k_n(x-x_{X_{22}})} & \text{if } x_{X_{22}} = 2x_P - x_{X_2} \in [0,1] \\ -\frac{1-\cos(k_n(x-x_{X_{22}}))}{8k_n(x-x_{X_{22}})} & \text{if } x_{X_{22}} = -(2x_P - x_{X_2}) \in [0,1] \end{cases} \tag{5.8b}$$

$$w_{3,\mathbf{X}_2}(x) = \begin{cases} \frac{1-\cos(k_n(x-x_{X_{23}}))}{8k_n(x-x_{X_{23}})} & \text{if } x_{X_{23}} = 2x_P + x_{X_2} \in [0,1] \\ \frac{\sin(k_n(x-x_{X_{23}}))}{8k_n(x-x_{X_{23}})} & \text{if } x_{X_{23}} = 2 - (2x_P + x_{X_2}) \in [0,1] \end{cases} \tag{5.8c}$$

Because the amplitude of the associated peak at x_{X_2} is half of the main normalised peak, one

can simply use the following expression to cancel out this associated peak.

$$w(x) = w_{\mathbf{X}|_{\mathbf{A}}^{\mathbf{P}}} - \frac{1}{2} w_{\mathbf{X}|_{\mathbf{X_2}}^{\mathbf{P}}} \tag{5.9}$$

An example is given in Fig. 5.4 with a piezoelectric actuator at $x_P = 0.25$ and an excitation pulse response at $x_A = 0.4$. At $x = 0.1$, the first kind of peak is fully cancelled as shown in yellow line. The extra effect is the introduction of smaller associated peaks due to $w_{2,\mathbf{X_2}}(x)$ and $w_{3,\mathbf{X_2}}(x)$. The former is related to the red associated peak at 0.4 in Fig. 5.4. As we have:

$$x_{X_{22}} = 2x_P - x_{X_2} = 2x_P - (2x_P - x_A) = x_A \tag{5.10}$$

this peak takes place at exactly the same position as the original main peak with an relative amplitude of $\frac{1}{4}$ compared to the original one. Another smaller associated peak corresponding to $w_{3,\mathbf{X_2}}(x)$ is a second kind of peaks created at $x_{X_{23}} = 0.6$.
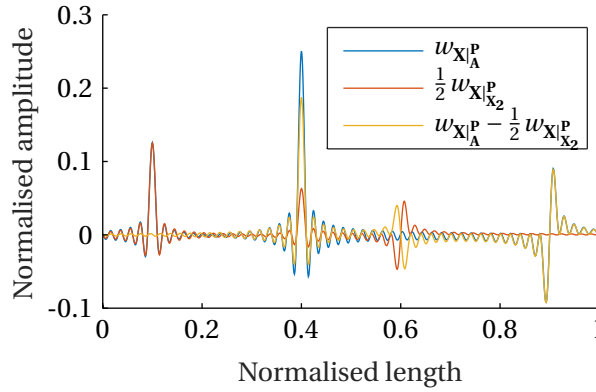
Figure 5.4 – Cancellation of the associated peak at $x_{X_2} = 0.1$

If there is a first kind of associated peak at position $x_{X_3} = 2 - (2x_P + x_{X_A})$, we can find a similar result that $x_{X_{33}} = 2 - (2x_P + x_{X_3})2 - (2x_P + 2 - (2x_P + x_{X_A})) = x_A$. This result shows that once we compensate a first kind of associated peak with an excitation pulse response, the cost is always a reduction of the main peak by $\frac{1}{4}$ of its amplitude and the introduction of other smaller amplitude associated peaks.

5.3.2 Cancellation of second kind of associated peaks

The second kind of peaks consists of a pair of opposite peaks described by the functions (5.4) and (5.5). The general form of these expressions is given in (5.11) and a particular result is just a zoomed and shifted version of it.

$$f_c(x) = \frac{1 - \cos(k_n x)}{k_n x} \tag{5.11}$$

Because it is an odd function, two opposite Sinc functions can be used to cancel out its peaks. Supposing the shift of the Sinc function is s and the scale factor is a. The function of these two opposite Sinc functions can be written as:

$$f_s(x, a, s) = a\left(\frac{\sin(k_n(x - s))}{k_n(x - s)} - \frac{\sin(k_n(x + s))}{k_n(x + s)}\right) \tag{5.12}$$

Then the problem becomes to an optimisation problem to find best parameters a and s which minimise the following objective function:

$$\underset{a,s}{\arg\min} \int_{-\infty}^{\infty} (f_c(x) - f_s(x, a, s))^2 dx \tag{5.13}$$

The optimised values of a and s can be obtained by applying the Quasi-Newton method to (5.13), the local minimal values closest to $s = 0$ (which means no shift) are $(a, s) = (0.61, 2.59)$ under $k_n = 1$ as shown in Fig. 5.5. If $k_n \neq 1$, the shift value becomes $s = \frac{2.59}{k_n}$ and the scale value is always $a = 0.61$.
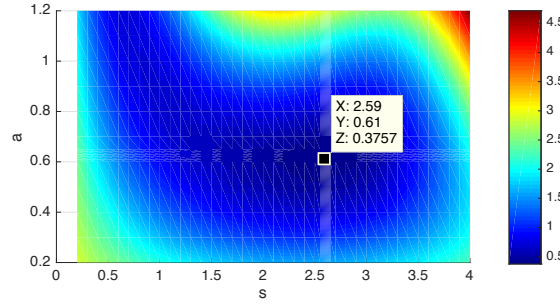
Figure 5.5 – Plot of the objective function $\int_{-\infty}^{\infty} (f_c(x) - f_s(x, a, s))^2 dx$ (while $k_n = 1$) around a local minimum value (s>0 and closest to s =0)

As a result, the normalised excitation pulse response needed is (if x_{X_3} has a second kind of associated peaks):

$$w_{\mathbf{X}|_{\mathbf{X}_{3,\pm}}^{\mathbf{P}}} = w_{\mathbf{X}|_{\mathbf{X}_{3,-}}^{\mathbf{P}}} - w_{\mathbf{X}|_{\mathbf{X}_{3,+}}^{\mathbf{P}}} \tag{5.14}$$

where $w_{\mathbf{X}|_{\mathbf{X}_{3,-}}^{\mathbf{P}}}$ stands for the response where its main peak is found at $x_{X_3} - s$ and $w_{\mathbf{X}|_{\mathbf{X}_{3,+}}^{\mathbf{P}}}$ for the one with a main peak at $x_{X_3} + s$. They both have three components similar to (5.8).

The suppression of the second kind of peaks is to minus (5.14) multiplied by its scale coefficient.

$$w(x) = w_{\mathbf{X}|_{\mathbf{A}}^{\mathbf{P}}} - \frac{0.61}{2} w_{\mathbf{X}|_{\mathbf{X}_{3,\pm}}^{\mathbf{P}}} \tag{5.15}$$

Similar to the previous results for the cancellation of the first kind of associated peaks. Extra ef-

fects are the introduction of the other smaller associated peaks due to $w_{2,\mathbf{X}_{3,\pm}}(x)$ and $w_{3,\mathbf{X}_{3,\pm}}(x)$. One pair of the introduced peaks (second kind) can also be proved to be superposed with the main peak. For example,

$$x_{X_{32,\pm}}(x) = -(2x_P - x_{X_{3,\pm}}) = -(2x_P - (2x_P - x_A \pm \frac{s}{k_n})) = x_A \mp \frac{s}{k_n} \tag{5.16}$$

The distance between these introduced peaks and the main peak is equal to $\frac{s}{k_n}$. According to (5.11), the relative reduction coefficient for the main peak can be then calculated by:

$$2\frac{a}{4}\frac{1 - \cos(k_n s)}{k_n s} = 2 \times \frac{0.61}{4} \times \frac{1 - \cos(2.59)}{2.59} = 0.218 \tag{5.17}$$

which indicates that the compensation of the second kind peak will reduce the main peak by 0.218 of its amplitude.

5.3.3 Cancellation with a single piezoelectric actuator

In previous subsections, the methods to cancel the first kind and second kind of associated peaks has been respectively presented. The analysis shows it will not only remove the associated peaks but also reduce the main peak and create other smaller associated peaks. In this section, we will demonstrate if a piezoelectric actuator is put at some specific places, the smaller associated peaks will disappear due to the superposition of themselves.

Considering the case while at the position x_{X_2}, it has a first kind of peaks and at x_{X_3}, it has a second kind of peaks, as $x_{X_{22}}$ and $x_{X_{32}}$ will always equal to x_A (according to (5.10) and (5.16)), we are interested in $x_{X_{23}}$ and $x_{X_{33}}$.

$$x_{X_{23}} = \begin{cases} 2x_P + x_{X_2} = 4x_P - x_A & \text{if it is in } [0,1] \\ 2 - (2x_P + x_{X_2}) = 2 - 4x_P + x_A & \text{if it is in } [0,1] \end{cases} \tag{5.18a}$$

$$x_{X_{33,\pm}} = \begin{cases} 2x_P + x_{X_{3,\pm}} = 4x_P + x_A \pm \frac{s}{k_n} & \text{if it is in } [0,1] \\ 2 - (2x_P + x_{X_{3,\pm}}) = 2 - 4x_P - x_A \mp \frac{s}{k_n} & \text{if it is in } [0,1] \end{cases} \tag{5.18b}$$

According to (5.18a) and (5.18b), they can cancel each other only if $4x_P = 2 - 4x_P$. The solution is then $x_P = 0.25$. It can also be verified that at $x_{X_{23}}$, it will take the first kind of peaks and at $x_{X_{33,\pm}}$, it is a sum of two opposite second kind of peaks. They will cancel out each other at the position $1 - x_A$.

The same result can be found while at x_{X_2} it has a second kind of peaks and at x_{X_3} it has a first kind of peaks. Indeed $x_P = 0.25$ is a special position, because it can be deduced that the value of $2x_P \pm x_A = 0.5 \pm x_A$ is either in $[0,1]$ or out of $[0,1]$ for any x_A. It has always an associated peak of first kind and another one of second kind.

Fig. 5.6 shows the theoretical result using approximate form for the cancellation of the asso-

(a) Original response result and the result with cancellation of associated peak

(b) Responses used to cancel the associated peaks
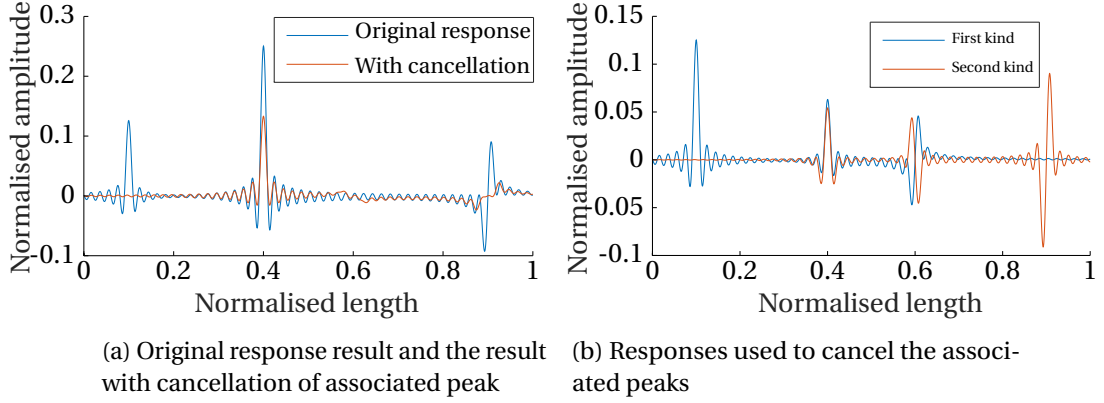
Figure 5.6 – Cancellation of associated peaks with one piezoelectric actuator at $x_P = 0.25$. The calculation is based on the approximate form of the surface amplitude with $n = 100$ and $x_A = 0.4$.

ciated peaks. The most important associated peaks are completely removed. The excitation pulse is given at $x_A = 0.4$ and the smaller associated peaks cancel each other at $1 - x_A = 0.6$ as predicted. For the amplitude aspect, without the cancellation, the amplitude of the second greatest peak is half of the one of the main peak, and after the removal of associated peaks, the second greatest peak amplitude is about 18% of the one of the main peak, although the amplitude of the main peak is also reduced by $\frac{1}{4} + 0.218 = 46.8\%$ compared to the original one.

(a) Number of eigenmodes $n = 100$

(b) Number of eigenmodes is $n = 25$
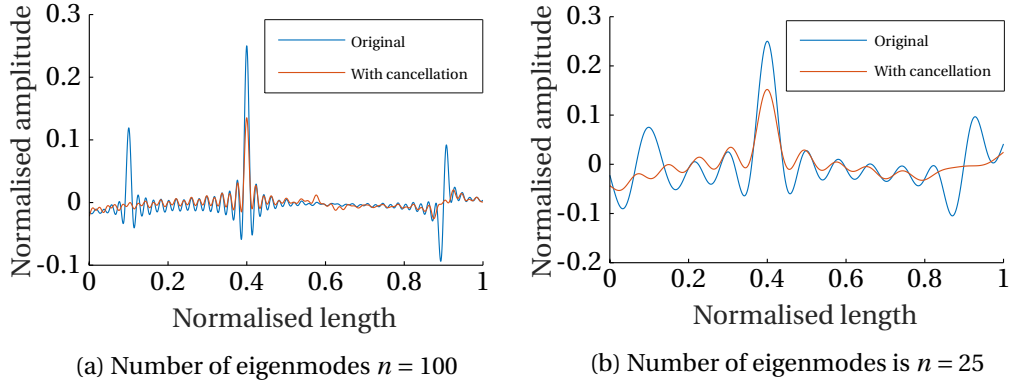
Figure 5.7 – Results obtained by adding directly the eigenmodes to restore the responses and the effect of cancellation of associated peaks using only eigenmodes sum. $x_P = 0.25, x_A = 0.4$

The approximate form of the amplitude helps to provide the analytical relationship between a main response and the responses which cancel out the associated peaks. In practice, we will use directly the eigenmodes to restore an excitation pulse. Fig. 5.7 gives the results by summing eigenmodes using the coefficients obtained in Section 5.3.2. These results show the effectiveness of this method for different number of eigenmodes used.

Moreover, due to the symmetry of the beam, $x = 0.75$ can be another position that all the associated peaks can be removed by only one piezoelectric actuator. In brief, with one piezoelectric actuator glued at $x = 0.25$ or $x = 0.75$, a pulse at any position on a beam (except the two extreme points) can be created using a combination of four excitation pulse responses.

5.3.4 Cancellation with multiple piezoelectric actuators

Sometimes, an important amplitude is required, but it cannot be achieved by only one piezoelectric actuator. Multiple piezoelectric actuators should be used in this case. In previous subsection, $x_P = 0.25$ and $x_P = 0.75$ are the only positions which allow to cancel out all the associated peak with only one actuator. In this subsection, the method to create a pure pulse using multiple actuators will be discussed.

According to (5.18), one can notice if $x_{X_{23}}$ and $x_{X_{33}}$ correspond to the responses created by different piezoelectric actuators, they can cancel each other only if $4x_{P_1} = 2 - 4x_{P_2}$. Then we have:

$$x_{P_1} = 2 \times 0.25 - x_{P_2} \tag{5.19}$$

which means there should be two piezoelectric actuators symmetrically placed around the position 0.25. It can be proved by the same way given in Section 5.3.3 that the small associated peaks created by one piezoelectric actuator take place at the same positions as the small associated peaks created by another one.

(a) Comparison between the superposed responses with and without cancellation

(b) Single piezo responses without cancellation
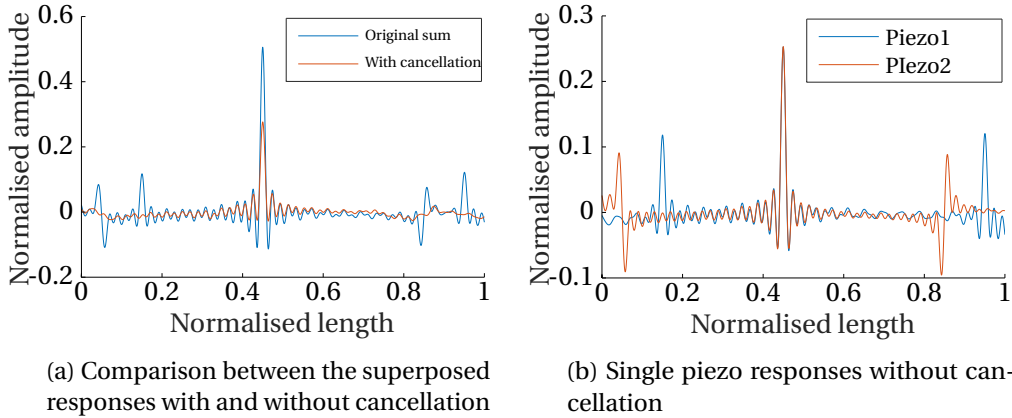
Figure 5.8 – Cancellation of associated peaks using two piezoelectric actuators at $x_{P_1} = 0.3$ and $x_{P_2} = 0.2$ given a pulse at position $x_A = 0.45$ calculated with 100 eigenmodes.

An example using two piezoelectric actuators is given in Fig. 5.8. As $x_{P_1} = 0.3$ and $x_{P_2} = 0.2$ can satisfy the condition (5.19), their associated peaks can be cancelled by applying the introduced method and their smaller associated peaks will be cancelled by themselves. The final peak amplitude is 0.276 and the reduction ratio is 44.8% which is close to the theoretical value

46.8%. The second greatest peak is 0.565, which is about 20.5% to the main peaks.

Compared to the single piezoelectric actuator case, the position of the second greatest peak and its relative amplitude does not change. It is always the peak closest to the main peak. However, at positions of second kind of associated peaks, the relative amplitude decreases. Thus, with multiple piezoelectric actuators, the main peak can have a more important amplitude and its waveform function remains the same as the one created by single piezoelectric actuator. At other positions, the relative amplitude (relative to the main peak amplitude) is closer to zero, which leads to a better spatial pulse quality on the beam.

According to the symmetry of the beam, two piezoelectric actuators which have same distance to $x = 0.75$ can also cancel out all associated peaks. As a result, the arrangement of the piezoelectric actuators for the creation of a pulse on the beam should respect the above conditions: they can be placed either at $x = 0.25$ and 0.75 or at two positions symmetric with regard to these two points.

5.4   Damping effect

According to the expression of (4.24), the damping term appeared in the amplitude expression can be extracted as follows:

$$f_{d,n}(T) = \frac{1 - e^{-2\zeta_n \omega_n T}}{4\zeta_n \omega_n} \tag{5.20}$$

This coefficient tends to a constant value while the reversal period T increases. While $T \to \infty$, function (5.20) will reach a saturation level. In general, the greater the term $\zeta_n \omega_n$ is, the faster it reaches to saturation value. As the final result is a sum of all eigenmodes multiplied by its damping coefficient, the reversal period for the saturation of the total displacement depends on the eigenmode with lowest $\zeta_n \omega_n$. Which means the amplitude of reconstructed pulse will increase in function of T, but if T is great enough, a greater T will not result a significant increase of amplitude.

Normally, we have to choose a value of T that all eigenmodes almost reach its saturation in order to have a best efficiency for the creation of a pulse vibration. Once T is chosen, for a concrete application, all the damping coefficients can be obtained by (5.20). Then we can introduce a weight modifier coefficient:

$$m_n = \frac{\sum_{i=1}^{N} f_{d,i}(T)}{N f_{d,n}(T)} \tag{5.21}$$

where N stands for the maximal number of eigenmodes.

If this term is added to (4.24), it becomes:

$$w_{m,\mathbf{A},\mathbf{P}}(\mathbf{X}, t) = k_s k_f \sum_n m_n \psi_n(\mathbf{X}) \psi_n(\mathbf{A}) \left(\frac{\nabla^2 \psi_n(\mathbf{P})}{\omega_n} \right)^2 \frac{1 - e^{-2\zeta_n \omega_n T}}{4\zeta_n \omega_n} \cos(\omega_n t) e^{-\zeta_n \omega_n t} \quad (5.22)$$

$$= k_s k_f \frac{\sum_{i=1}^{N} f_{d,i}(T)}{N} \sum_n \psi_n(\mathbf{X}) \psi_n(\mathbf{A}) \left(\frac{\nabla^2 \psi_n(\mathbf{P})}{\omega_n} \right)^2 \cos(\omega_n t) e^{-\zeta_n \omega_n t}$$

The summing term in (5.22) is then free of damping terms and it will finally give a same result as the one in theoretical analysis for the generation of a pulse.

5.5 Conclusion

Two functions have been found to represent the main peak and two kinds of associated peaks. The error analysis has been done numerically by enumerating the response on different points on a beam. With the help of these functions, one can deduce that the first kind of peaks can be removed by a main peak with $\frac{1}{2}$ amplitude. A second kind of peaks can be removed by two opposite main peaks with a shift of $\pm \frac{2.59}{k_n}$ and with $\frac{0.61}{2}$ of its amplitude.

If piezoelectric actuators are correctly placed, the smaller associated peaks created by the compensation responses can be cancelled out by each other. In the case of a single piezoelectric actuator configuration, one can put the actuator either at $x_P = 0.25$ or at $x_P = 0.75$. For multiple actuators arrangement, they should be placed symmetrically with regard to these two positions.

The last thing to consider for the reconstruction of a pulse vibration on a beam is the damping term. Its theoretical expression shows its amplitude depends on the time reversal duration T. It should be long enough to have a greater amplitude, but due to the saturation effect, it is meaningless to choose a very great T while all modes almost reach their saturation. Once T is chosen, one can compensate the damping term by a weight modifier, which permits to guarantee a response expression equivalent to the one obtained in the theoretical analysis.

6 Drive and modelling

Contents

This chapter presents the modelling of the self-oscillating class-D amplifier used as a drive for piezoelectric actuators. Firstly, the modelling of the amplifier is given. Theoretical studies are made for the first order and the second order configurations. Secondly, a modelling of the non-periodic PWM is achieved, which can be used to analytically study the output signal of the drive and to help the design of the output filter. Thirdly, according to the theoretical analysis, a design is given to meet all the requirements for the application on a piezo-excited vibrating plate.

6.1 Introduction

According to the state of the art for the piezoelectric actuator driving technologies introduced in Section 2.4.5, the self-oscillating class-D amplifier is the best solution to generate arbitrary signals for piezoelectric actuators for our application. With a variable frequency range between 100 Hz and 20 kHz and with a maximal voltage of 150 V, it can reach nearly the limit of switching components. The self-oscillating class-D amplifier has two common topologies: first order and second order. Their typical schematics are given in Fig. 6.1. In order to determine the parameters in the circuit, a modelling will be made, which will deduce a stability criteria depending on these parameters.

The output signal of a self-oscillating class-D amplifier is a non-periodic PWM signal. The calculation of its frequency spectrum is important for the design of the output filter. Theoretical studies have been carried out mainly on periodic PWM signals [2] but not on non-periodic PWM signals. Thus it would be interesting to develop a theoretical representation of non-periodic PWM signals in order to study theoretical properties of its frequency spectrum and to determine the cutoff frequency for the output low-pass filter.
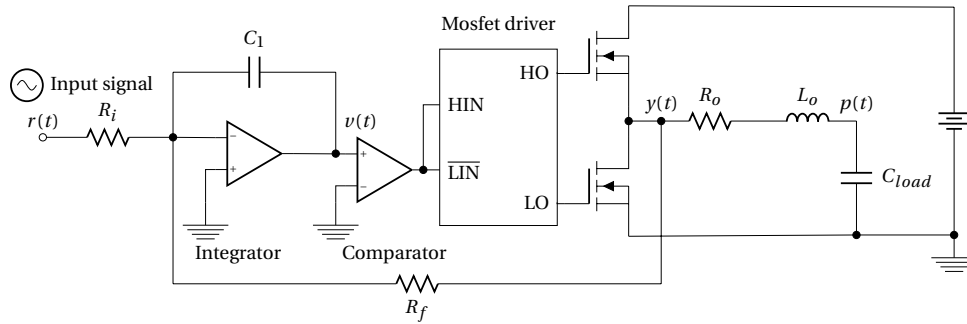
(a) First order schematic
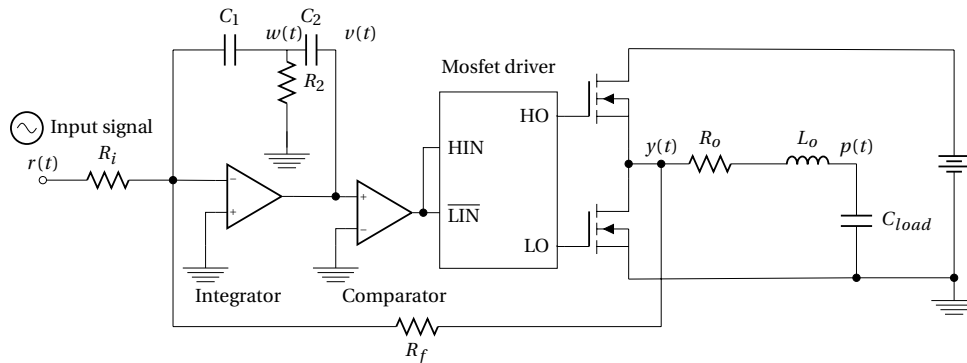
(b) Second order schematic

Figure 6.1 – Class-D self-oscillating amplifier schematics
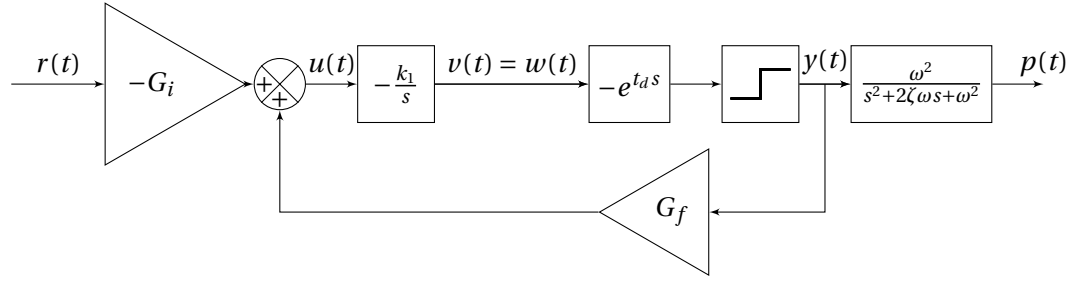
(a) First order block diagram
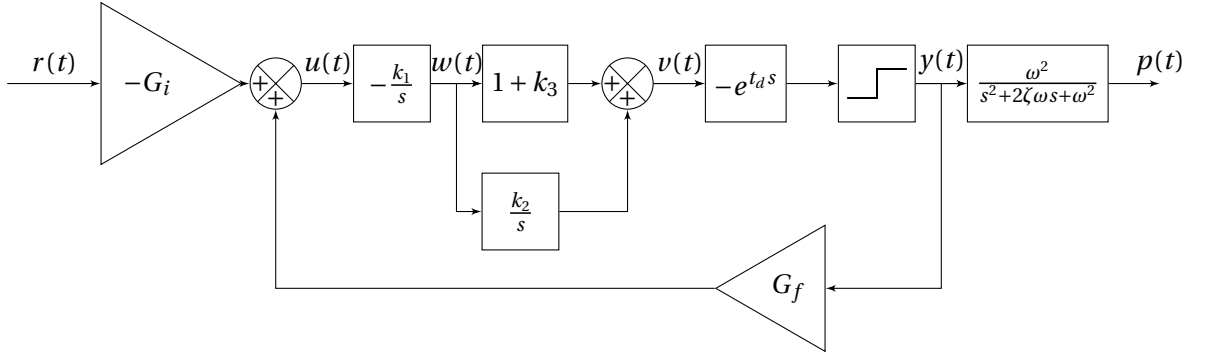
(b) Second order block diagram

Figure 6.2 – Class-D self-oscillating amplifier block diagrams

6.2 Self-oscillating class-D amplifiers

As presented in the previous section, Fig. 6.1 gives a general self-oscillating class-D amplifier description. Firstly, the error between the input signal and the feedback signal is integrated. One can note there are two different versions of the integrating part: a first order circuit (Fig. 6.1a) and a second order circuit (Fig. 6.1b). Then the comparator examines the sign of the integrated result and gives the control signals to the MOSFET drivers. After a certain delay caused by electronic components, the output is changed. Its equivalent block diagram is given in Fig. 6.2. Because the self-oscillating amplifier has a 180° phase shift, we use $r(t)$ to present the reference signal. The governing equations of the system can be written as follows:

$$u(t) = G_f y(t) - G_i r(t) \tag{6.1}$$

$$w(t) = -k_1 \int u(t) dt + A \tag{6.2}$$

$$v_f(t) = w(t) \qquad\qquad \text{first order} \tag{6.3}$$

$$v_s(t) = k_2 \int w(t) dt + (1 + k_3) w(t) + B \qquad\qquad \text{second order} \tag{6.4}$$

$$y(t) = \begin{cases} Y & \text{if} \quad v_i(t - t_d) > 0 \quad i \in \{s, f\} \\ 0 & \text{if} \quad v_i(t - t_d) \leq 0 \quad i \in \{s, f\} \end{cases} \tag{6.5}$$
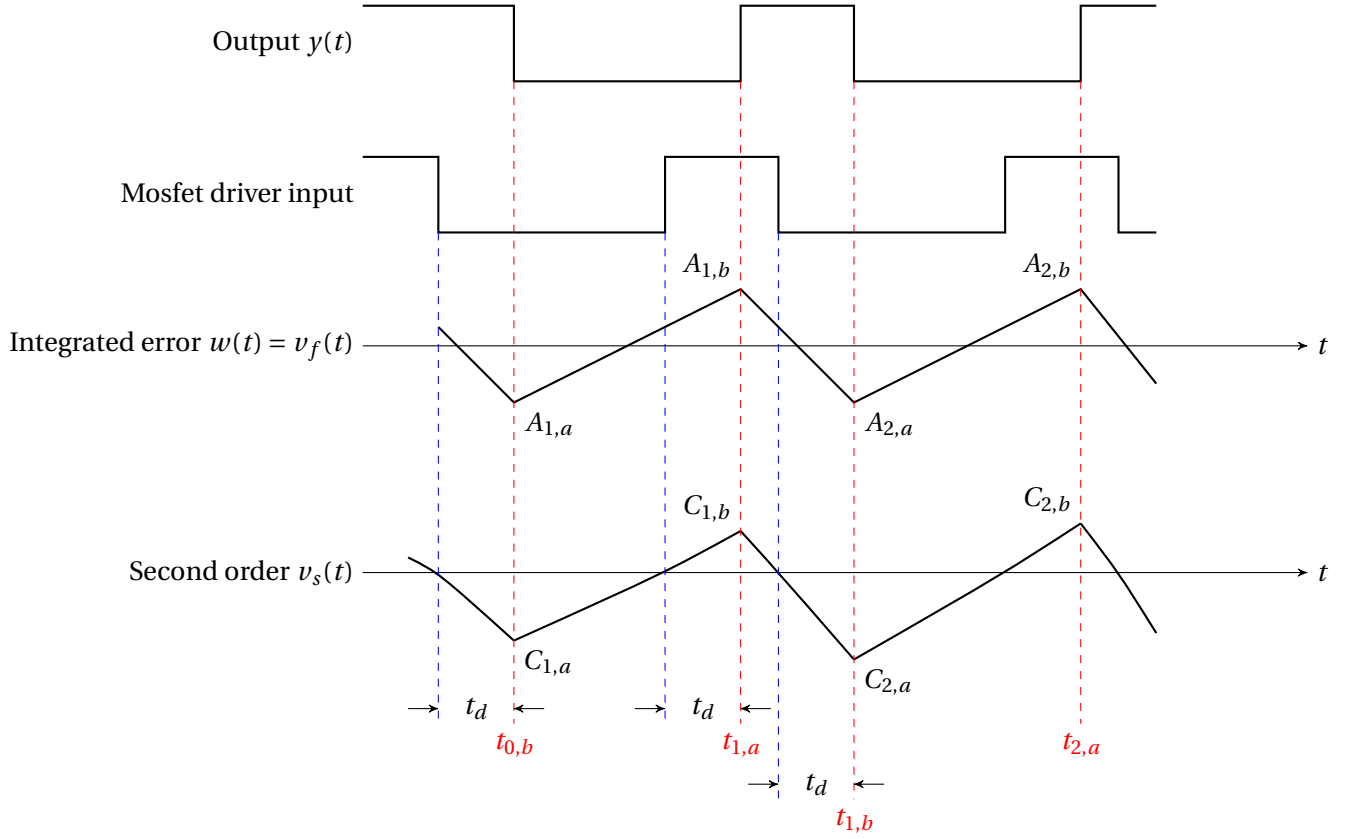
Figure 6.3 – Second order class-D self-oscillating amplifier signals view

where (6.3) represents a first order system. Equation (6.4) is the expression if the second order component is taken into consideration. A and B are constants which depend on initial conditions. t_d represents the total system delay. k_1, k_2, G_f , G_i are all positive parameters.

The switching frequency is typically several hundreds of kilohertz which is much higher than the reference signal frequency. It can be assumed in a short instance (several switching periods), the value of $r(t) = r > 0$ is constant. Moreover, we use two indices a and b to represent the "off" and "on" period for $y(t)$. Supposing time from $t_{0,b}$ to $t_{1,a}$, $y(t)$ is off and from $t_{1,a}$ to $t_{1,b}$, $y(t)$ is on, then, from $t_{1,b}$ to $t_{2,a}$, $y(t)$ goes off again and so on. Thus, the input signal $u(t)$ can be written as:

$$u_a = u(t) = G_f \cdot 0 - G_i r < 0 \quad \text{where} \quad t_{n-1,b} < t < t_{n,a} \tag{6.6}$$

$$u_b = u(t) = G_f Y - G_i r > 0 \quad \text{where} \quad t_{n,a} < t < t_{n,b} \tag{6.7}$$

In order to simplify the notation for each on and off periods, we note $v_{f,n,a}(t)$ and $v_{f,n,b}(t)$ as

the new variables by displacing the origin for each n:

$$v_{f,n,a}(t) = v(t + t_{n-1,b}) \qquad\qquad 0 < t < t_{n,a} - t_{n-1,b} \qquad (6.8)$$

$$v_{f,n,b}(t) = v(t + t_{n,a}) \qquad\qquad 0 < t < t_{n,b} - t_{n,a} \qquad (6.9)$$

For the first order system according to (6.2),(6.3) and (6.8):

$$v_{f,n,a}(t) = -u_a k_1 t + A_{n,a} \qquad (6.10)$$

$$v_{f,n,b}(t) = -u_b k_1 t + A_{n,b} \qquad (6.11)$$

with continuity and switching conditions:

$$A_{n,b} = v_{f,n,a}(T_{n,a}) = -u_a k_1 T_{n,a} + A_{n,a} \quad \text{where} \quad T_{n,a} = t_{n,a} - t_{n-1,b} \qquad (6.12)$$

$$A_{n+1,a} = v_{f,n,b}(T_{n,b}) = -u_b k_1 T_{n,b} + A_{n,b} \quad \text{where} \quad T_{n,b} = t_{n,b} - t_{n,a} \qquad (6.13)$$

$$v_{f,n,a}(T_{n,a} - t_d) = 0 \qquad (6.14)$$

$$v_{f,n,b}(T_{n,b} - t_d) = 0 \qquad (6.15)$$

Similar to the first order system, with the notation $w_{n,a}$, $w_{n,b}$, $v_{s,n,a}$, $v_{s,n,b}$ for new displaced variables as shown in Fig. 6.3, the equations for the second order system are:

$$w_{n,a}(t) = -u_a k_1 t + A_{n,a} \qquad (6.16)$$

$$w_{n,b}(t) = -u_b k_1 t + A_{n,b} \qquad (6.17)$$

$$v_{s,n,a}(t) = -\frac{u_a k_1 k_2}{2} t^2 + (k_2 A_{n,a} - (1 + k_3) k_1 u_a) t + C_{n,a} \qquad (6.18)$$

$$v_{s,n,b}(t) = -\frac{u_b k_1 k_2}{2} t^2 + (k_2 A_{n,b} - (1 + k_3) k_1 u_b) t + C_{n,b} \qquad (6.19)$$

where $C_{n,a} = (1 + k_3) A_{n,a} + B_{n,a}$ and $C_{n,b} = (1 + k_3) A_{n,b} + B_{n,b}$ are constants and an example of the signals is given in Fig. 6.3. The switching conditions are also similar to previous ones:

$$A_{n,b} = w_{n,a}(T_{n,a}) \qquad (6.20)$$

$$A_{n+1,a} = w_{n,b}(T_{n,b}) \qquad (6.21)$$

$$C_{n,b} = v_{s,n,a}(T_{n,a}) \qquad (6.22)$$

$$C_{n+1,a} = v_{s,n,b}(T_{n,b}) \qquad (6.23)$$

$$v_{s,n,a}(T_{n,a} - t_d) = 0 \qquad (6.24)$$

$$v_{s,n,b}(T_{n,b} - t_d) = 0 \qquad (6.25)$$

Until now, all necessary equations have been established with which the system can be studied and analysed.

6.3 System properties

The first order is very simple. Many articles give the solution [80][10]. Contrarily, the solution for the second order system is not obvious. Cox *et al.* [26] tried to mathematically analyse the periodic modulation of second order class-D amplifier, but it merely appears difficult for a fixed frequency case. Some related works about fixed frequency PWM class-D amplifiers mentioned that the second order system would always introduce a higher distortion due to the contributions of DC errors [98][60]. While for phase-shift self-oscillating topologies, experiments show that a second order system will lead to less distortion [82][61]. In this section, firstly, we will demonstrate the existence of solutions and give the stability criteria of the second order system. Secondly, based on the analytical result, the different roles of system parameters will be discussed.

6.3.1 Iterative expressions

The first step is to solve (6.25) which can be transformed into a quadratic equation with $t_r = T_{n,a} - t_d$ as in (6.26). Because it is in the interval where $y(t)$ has been turned off at $t_{n-1,b}$, from (6.5) and (6.23), it can be seen that $C_{n,a} < 0$, which ensures the discriminant of (6.26) to be greater than 0 and thus it has two different roots.

$$-\frac{u_a k_1 k_2}{2} t_r^2 + (k_2 A_{n,a} - (1 + k_3) k_1 u_a) t_r + C_{n,a} = 0 \tag{6.26}$$

Only the smallest positive root of (6.26) can meet the condition (6.5). Thus, the solution is:

$$t_r = \frac{k_2 A_{n,a} - (1 + k_3) k_1 u_a - \sqrt{(k_2 A_{n,a} - (1 + k_3) k_1 u_a)^2 + 2 u_a k_1 k_2 C_{n,a}}}{u_a k_1 k_2} \tag{6.27}$$

Bringing $T_{n,a} = t_r + t_d$ into (6.20) and (6.21), expressions without time variable can be then found as follows:

$$A_{n,b} = \frac{\sqrt{\Delta_{n,a}}}{k_2} + \frac{1 + k_3}{k_2} k_1 u_a - t_d k_1 u_a \tag{6.28}$$

$$C_{n,b} = t_d \sqrt{\Delta_{n,a}} - \frac{k_1 k_2 u_a}{2} t_d^2 \tag{6.29}$$

$$\Delta_{n,a} = (k_2 A_{n,a} - (1 + k_3) k_1 u_a)^2 + 2 u_a k_1 k_2 C_{n,a} \tag{6.30}$$

Similarly, the variables at $t_{n+1,a}$ can be written as:

$$A_{n+1,a} = -\frac{\sqrt{\Delta_{n,b}}}{k_2} + \frac{1+k_3}{k_2} k_1 u_b - t_d k_1 u_b \tag{6.31}$$

$$C_{n+1,a} = -t_d \sqrt{\Delta_{n,b}} - \frac{k_1 k_2 u_b}{2} t_d^2 \tag{6.32}$$

$$\Delta_{n,b} = (k_2 A_{n,b} - (1+k_3) k_1 u_b)^2 + 2 u_b k_1 k_2 C_{n,b} \tag{6.33}$$

As all k, u, t_d are constant, the new initial values of A and C for the next time interval only depend on previous A and C. By combining (6.27)-(6.33), we can construct the iterative functions:

$$(A_{n,b}, C_{n,b}) = f_{b,a}(A_{n,a}, C_{n,a}) \tag{6.34}$$

$$(A_{n+1,a}, C_{n+1,a}) = f_{a,b}(A_{n,b}, C_{n,b}) \tag{6.35}$$

$$(A_{n+1,a}, C_{n+1,a}) = f_{a,b} \circ f_{b,a}(A_{n,a}, C_{n,a}) = f_a(A_{n,a}, C_{n,a}) \tag{6.36}$$

$$(A_{n+1,b}, C_{n+1,b}) = f_{b,a} \circ f_{a,b}(A_{n,b}, C_{n,b}) = f_b(A_{n,b}, C_{n,b}) \tag{6.37}$$

where f are functions which map the integrator constant from the current "on" and "off" period to the next period.

6.3.2 Existence of solution

If (6.36) and (6.37) have respectively a fixed point, the system will have a stable solution. Straightforward calculation may be difficult because it is indeed a quartic function, the verification of its discriminants will be very time consuming and exhausting. Thus, we prefer to only give a proof of the existence of solution by applying Brouwer theorem. Because f_a and f_b are well continuous thanks to its definition, the problem can be transformed to prove that it exists a compact space E that the image of $f(E)$ is still in E.

According to (6.7) and (6.32), it is easy to find that $C_{n,a}$ is always negative and $A_{n+1,a}$ remains also negative if $C_{n,a}$ and $A_{n,a}$ are negative. The upper closed bounded boundaries are found. Next, we examine the function f_a by three cases for lower boundaries: the following i) and ii) will give demonstrations that with a large enough boundary, $A_{n+1,a}$ and $C_{n+1,a}$ are bounded; While in iii), it will be proved that all the internal points with a large enough boundary are bounded.

i) Relation between $A_{n,a}$ and $A_{n+1,a}$ with $0 \gg q A_{n,a} = C_{n,a}$

The conditions in this section are that 1). $|A_{n,a}|$ and $|C_{n,a}|$ are big enough and 2). It exists a constant factor q as the ratio between them. Equation (6.31) can be divided into two parts: the first one A_{p_1} depends on $A_{n,b}$ and $C_{n,b}$; the second part A_{p_2} depends only on the system

parameters. We would like to have $A_{p_1} > -A_{n,b}$ and $A_{p_1} > 0$ so that $A_{n+1,a} > -A_{n,b}$.

$$A_{p_1} = -\frac{\sqrt{\Delta_{n,b}}}{k_2} \tag{6.38}$$

$$A_{p_2} = (\frac{1+k_3}{k_2} - t_d) k_1 u_b \tag{6.39}$$

Because k_1 and u_b are positive, the condition for $A_{p_2} > 0$ is:

$$\frac{1+k_3}{k_2} > t_d \tag{6.40}$$

For A_{p_1}, taking (6.28), (6.29) and (6.33) into (6.38) and leaving the second order term of $A_{n,b}$ in its discriminant, A_{p_1} becomes:

$$A_{p_1} = -\frac{k_2^2 A_{n,b}^2 - 2((1+k_3) - k_2 t_d) k_1 k_2 u_b \frac{\sqrt{\Delta_{n,a}}}{k_2} + D}{k_2} \tag{6.41}$$

where D is a constant term depending only on system parameters. When $|A_{n,a}|$ and $|C_{n,a}|$ are big enough, $A_{n,b}$ trends to $-A_{n,a}$ and so is $\frac{\Delta_{n,a}}{k_2}$. In (6.41), D becomes negligible. If (6.40) is satisfied, the value of the term with in (6.41) is negative. Then, we have $A_{p_1} > -A_{n,b}$ and thus $A_{n+1,a} > -A_{n,b}$.

In the same way, it can be proved that if (6.40) was true, we also have $A_{n,b} < -A_{n,a}$. Finally, the relation $A_{n+1,a} > A_{n,a}$ can be deduced.

ii) Relation between $C_{n,a}$ and $C_{n+1,a}$ while $0 \gg q A_{n,a} = C_{n,a}$

According to (6.28), (6.29) and (6.30), while $|A_{n,a}|$ and $|C_{n,a}|$ are big enough, we use big theta notations Θ (asymptotic notation) to present the boundaries of following functions:

$$\Delta_{n,a} = \Theta(k_2^2 A_{n,a}^2) \tag{6.42}$$

$$A_{n,b} = \Theta(|A_{na}|) \tag{6.43}$$

$$C_{n,b} = \Theta(|t_d k_2 A_{n,a}|) \tag{6.44}$$

Then, taking (6.42), (6.43) and (6.44) into (6.31), (6.32) and (6.33), we have:

$$\Delta_{n,b} = \Theta(k_2^2 A_{n,a}^2) \tag{6.45}$$

$$A_{n+1,a} = \Theta(-|A_{n,a}|) \tag{6.46}$$

$$C_{n+1,a} = \Theta(-|t_d k_2 A_{n,a}|) \tag{6.47}$$

According to (6.47), it exists a positive constant $q > t_d k_2$ that when $A_{n,a}$ is big enough, $C_{n+1,a}$ is always smaller than $q A_{n,a} = C_{n,a}$.

iii) Relation between $A_{n,a}$ and $A_{n+1,a}$ while $q A_{n,a} = -C_{n,a} \gg 0$

According to (6.46), for an $A_{n,a}$ big enough, its image for the next period $A_{n+1,a}$ should be negative so that we always have $A_{n+1,a} < A_{n,a}$ in this case.

iv) Image of $A_{n,a}$ and $C_{n,a}$ while $A_{\mathbf{big}} > A_{n,a} > -2A_{\mathbf{big}}$ and $0 > C_{n,a} > -C_{\mathbf{big}} = -q A_{\mathbf{big}}$

We define the notation $(x_1, y_1) > (x_2, y_2)$ if and only if $x_1 > x_2$ and $y_1 > y_2$. In this subsection, the objective is to prove that given $|A_{n,a}|$ and $|C_{n,a}|$ big enough, we always have $f(A_{n,a}, C_{n,a}) > f(-2A_{\text{big}}, -C_{\text{big}})$.

Introducing $A_p = \max(\frac{(1+k_3)k_1}{k_2|u_1|}, \frac{(1+k_3)k_1}{k_2|u_2|})$, while $(A_p, 0) > (A_{n,a}, C_{n,a}) > (-A_p, -q A_p)$, because f is a continuous function which does not have any singularity point, $f(A_{n,a}, C_{n,a})$ is indeed bounded by a pair $(A_{\text{bound}}, C_{\text{bound}})$.

Otherwise, if $A_{\text{big}} > A_{n,a} > A_p$, as discussed in iii). and $C_{n,a}$ is always negative, we have $(A_{\text{big}}, 0) > f(A_{n,a}, C_{n,a})$. One can also see when $(-A_p, -q A_p) > (A_{n,a}, C_{n,a}) > (-2A_{\text{big}}, -C_{\text{big}})$, the image of f drops into a monotonic interval. The relation $f(A_{n,a}, C_{n,a}) > f(-2A_{\text{big}}, -C_{\text{big}}) > (-2A_{\text{big}}, -C_{\text{big}})$ is always true.

As a result, it exists a pair $(-A_{\text{big}}, -C_{\text{big}})$ that for all $(A_{\text{big}}, 0) > (A_{n,a}, C_{n,a}) > (-2A_{\text{big}}, -C_{\text{big}})$, we have $(A_{\text{big}}, 0) > f(A_{n,a}, C_{n,a}) > (-2A_{\text{big}}, -C_{\text{big}})$.

v) Conclusion

Finally, according to i)., ii)., iii). and iv)., it exists a pair $(A_m, C_m) = (A_m, q A_m)$ with an A_m big enough and we can define a compact square space **E** that $\mathbf{E} = [-2A_m \quad A_m] \times [-C_m \quad 0]$. Under the condition of (6.40), for all pairs $P \in \mathbf{E}$, we have $f_a(P) \in \mathbf{E}$, together with the continuity property of f, the preliminary conditions of Brouwer theorem are satisfied. So, it exists a fixed element $P_{\text{fix}} = (A_a, C_a)$ that $P_{\text{fix}} = f_a(P_{\text{fix}})$.

It can be easily found that $(A_b, C_b) = f_{a,b}(P_{\text{fix}})$ is a fixed point of f_b as well. From now on, we have the right to use the fixed point for other numerical applications.

6.3.3 Second order system stability criteria

According to Fig. 6.1 and Fig. 6.2, the system parameters are:

$$k_1 = \frac{1}{C_1} \tag{6.48}$$

$$k_2 = \frac{1}{C_2 R_2} \tag{6.49}$$

$$k_3 = \frac{C_1}{C_2} \tag{6.50}$$

As discussed in the previous subsections, equation (6.40) is the condition to ensure the existence of the stable point. Taking (6.49) and (6.50) into (6.40), we have:

$$R_2 > \frac{t_d}{C_1 + C_2} \tag{6.51}$$

It can be noticed the shorter the delay is, the more stable the system is. And R_2 should be big enough to adapt the delay time. Normally, in our practice, R_2 is set to be 5 or 10 times greater than its critical value.

Moreover, R_2 also affects the converging velocity while the solution exists. One can find that while R_2 tends to infinity, the system reduces to first order and it will enter stable state after one switching period.

6.3.4 Modulation index and period

In a steady state, A and C should be constant. Replacing $A_{n+1,a}$ by $A_{n,a}$ in (6.21) and merging to (6.16) and (6.17), the switching time can be obtained:

$$T_a = \frac{A_{n,b} - A_{n,a}}{-u_a k_1} \tag{6.52}$$

$$T_a = \frac{A_{n,a} - A_{n,b}}{-u_b k_1} \tag{6.53}$$

The ratio (modulation index) k' between "on" interval and one period is:

$$k' = \frac{T_b}{T_a + T_b} = -\frac{u_a}{u_a + u_b} \quad k' \in [0 \quad 1] \tag{6.54}$$

This result is the same as the solution of (6.10)-(6.15) for the first order system. Otherwise, the switching period for both first order and second order is:

$$T = \frac{A_{n,a} - A_{n,b}}{\min(1 - k', k' - 1) u_a k_1} \tag{6.55}$$

which can be examined later either by direct calculation (first order system) or by the value obtained at steady state (second order system).

6.4 Spectral analysis for non-periodic PWM

The objective of this section is to propose a general analytical method to evaluate the non-periodic PWM. Because the total harmonic distortion (THD) is often used to evaluate the quality of the output signal, the most straight-forward method is to calculate the spectral distribution of the output signal. Due to the non-periodic nature of the self-oscillating amplifier, it is not obvious to apply the direct calculation to obtain an analytical result. As a result, a new method is needed to solve this problem.

The idea in this section is, firstly , separately study each rectangular wave element of a PWM with Fourier transform, and then, put them together. In the second place, we will demonstrate that a PWM waveform is similar to the sum of two saw-tooth waves which can lead to further simplifications, especially for self-oscillating PWM.

6.4.1 Rectangular wave

Each "on" and "off" element of a PWM wave is a single rectangular wave. According to Fig. 6.4, supposing the signal is T periodic, the duration of one element is D and it switches between $-A$ and A (where A is the amplitude), we can obtain the expression for one PWM element as in (6.56). Normally the ratio k (k is defined in $[-1 \quad 1]$ and $k = 2k' - 1$) of the PWM element depends on the value of the original function $f(t)$. One can use the middle value $f(t_m)$, $m \in [\![1, M]\!]$ (M is the number of square elements inside "on" period) to determine the ratio for an element. Supposing the maximum allowable value of signal is A, k is then equal to $\frac{f(t_m)}{A}$.

Firstly, we calculate the Fourier coefficients of one element $g_{rec}(t)$:

$$g_{rec}(t) = \begin{cases} A & -\frac{D}{2} < t < \frac{kD}{2} \\ -A & \frac{kD}{2} < t < \frac{D}{2} \\ 0 & else \end{cases} \tag{6.56}$$

$$C_n^{rec} = \frac{1}{T}\int_{-\frac{D}{2}}^{\frac{kD}{2}} A e^{-in\omega_0 t} dt + \frac{1}{T}\int_{\frac{kD}{2}}^{\frac{D}{2}} -A e^{-in\omega_0 t} dt = \frac{A}{n\pi} e^{n\pi\frac{kD}{T}} - i\frac{A}{n\pi}\cos(n\pi\frac{D}{T}) \tag{6.57}$$

where $\omega_0 T = 2\pi$.

Then, we sum up all the Fourier coefficients of each element together by shifting the element over time t_m. Noticing each element has a different duration and modulation ratio, one can sum up each element shown in Fig. 6.4b with the index m.
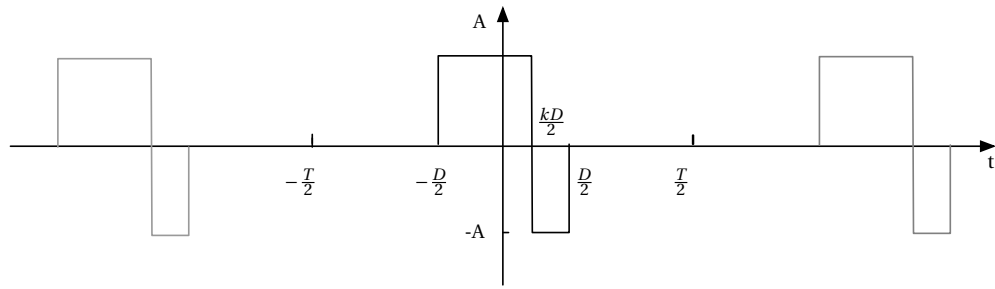
(a) One element of a PWM
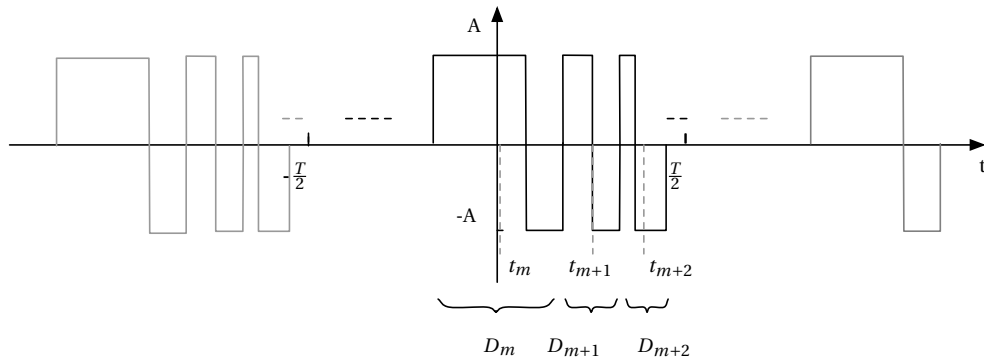
(b) Sum of elements in order to restore the PWM

Figure 6.4 – Steps for the study of a non-periodic PWM
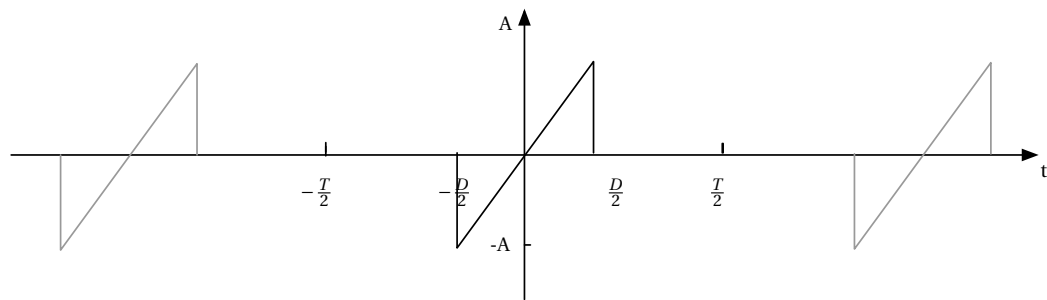
Figure 6.5 – Slash wave

$$C_n^{PWM} = \sum_m C_n^{rec} e^{-i2\pi n \frac{t_m}{T}} = \sum_m \frac{A}{n\pi} e^{n\pi \frac{k_m D_m}{T}} e^{-i2\pi n \frac{t_m}{T}} - \sum_m \frac{iA}{n\pi} \cos(n\pi \frac{D_m}{T}) e^{-i2\pi n \frac{t_m}{T}}$$

(6.58)

6.4.2 Slash wave

Similar to the rectangular wave, a slash wave can also be defined with the periodic parameter T and its local element duration D. The slash wave function $g_{sl}(t)$ is:

$$g_{sl}(t) = \begin{cases} \frac{A}{D}t & -\frac{D}{2} < t < \frac{D}{2} \\ 0 & else \end{cases} \tag{6.59}$$

Its Fourier transform coefficients are:

$$C_n^{sl} = \frac{1}{T} \int_{-\frac{D}{2}}^{\frac{D}{2}} \frac{A}{D} t e^{-in\omega_0 t} dt = -\frac{iA}{n\pi}\cos(n\pi\frac{D}{T}) + \frac{iAT}{n^2\pi^2 D}\sin(n\pi\frac{D}{T}) \tag{6.60}$$

It is trivial to find the last term of (6.57) and the first term of (6.60) are the same. If they are summed up with a same series of D_m, these terms are still equivalent.

Due to the symmetry of the PWM waveform, for the other half of the expression, we want to demonstrate that it is also related to a part of slash wave (sawtooth waveform when summed up) and the candidate should be:

$$g_{sl_2}(t) = \begin{cases} -\frac{A}{D}t & -\frac{D}{2} < t < \frac{D}{2} \\ 0 & else \end{cases} \tag{6.61}$$

$$\sum_m C_n^{sl_2} = \sum_m \frac{iA}{n\pi}\cos(n\pi\frac{D'_m}{T})e^{-i2\pi n\frac{t'_m}{T}} - \sum_m \frac{iAT}{n^2\pi^2 D'_m}\sin(n\pi\frac{D'_m}{T})e^{-i2\pi n\frac{t'_m}{T}} \tag{6.62}$$

where $D'_m = D_m(\frac{1}{2} - k_m) + D_{m+1}(\frac{1}{2} + k_{m+1})$ and $t'_m = t_m + k_m D_m + \frac{D'_m}{2}$. Now the objective is to demonstrate that the first term of (6.62) is equal to the first term of (6.58) while $n \geq 1$. The easiest method is via graphics.

According to the inverse Fourier transform, as shown in Fig. 6.6a, the expression $\frac{A}{n\pi}e^{n\pi\frac{kD}{T}}$ in time domain is a line from $-\frac{T}{2}$ to $\frac{kD}{2}$ and from $\frac{kD}{2}$ to $\frac{T}{2}$ with a slope of $\frac{2A}{T}$. The entire waveform is centrosymmetric at $\frac{kD}{2}$.

The inverse Fourier transform of $\frac{iA}{n\pi}\cos(n\pi\frac{D'_n}{T})$ is given in Fig. 6.6b. It is centrosymmetric and have zeros at $-\frac{T}{2}$, 0 and $\frac{T}{2}$. The points $-\frac{D'}{2}$ and $\frac{D'}{2}$ separate the lines into three segments with the same slope of $\frac{2A}{T}$.

First of all, for the most trivial case where the PWM contains only one element with 50% ratio, thus $D = T$ and $k_n = 0$, it is obvious that $\sum_m \frac{iA}{n\pi}\cos(n\pi\frac{D'_m}{T})e^{-i2\pi n\frac{t'_m}{T}} = \sum_m \frac{A}{n\pi}e^{n\pi\frac{k_m D_m}{T}}e^{-i2\pi n\frac{t_m}{T}}$ due to the identical waveform.

Then, if we delay the step down instant of a PWM element D_m for ΔD as shown in Fig. 6.7, in
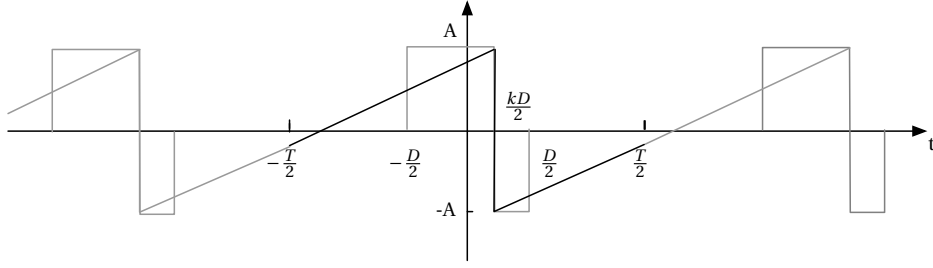
(a) Inverse Fourier transform of $\frac{A}{n\pi} e^{n\pi \frac{kD}{T}} (n \geq 1)$
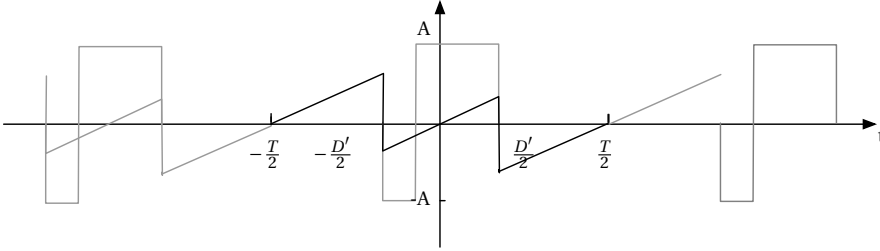
(b) Inverse Fourier transform of $\frac{iA}{n\pi} \cos(n\pi \frac{D'}{T})(n \geq 1)$

Figure 6.6 – Inverse Fourier transform results

the two cases, the difference inside ΔD (hatched area) is $2A$. Besides, in Fig. 6.7a, the waveform moves to the right and the vertical difference becomes $-\Delta D \frac{2A}{T}$ outside ΔD. In Fig. 6.7b, due to the change of symmetry centre, waveforms for D'_n and D'_{n-1} raised both $-\frac{\Delta DA}{T}$, thus the total displacement is $-\frac{2\Delta DA}{T}$ for each instant t outside ΔD. As a result, all the values are changing in the same way for the two cases, thus, they are always identical to each other.

Similarly, we can also obtain the same result if we delay the step up instant of a PWM element. In the two cases, the sum of the waves for each instant remains identical.

Thanks to the two points above, we can recursively demonstrate the problem. Based on the most trivial case, we can add new zero period elements which can then be transformed to cover all possibilities of PWM and the equality is always guaranteed by the second point. Thus, the conclusion is that the equality $\sum_m \frac{iA}{n\pi} \cos(n\pi \frac{D'_m}{T}) e^{-i2\pi n \frac{t'_m}{T}} = \sum_m \frac{A}{n\pi} e^{n\pi \frac{k_m D_m}{T}} e^{-i2\pi n \frac{t_m}{T}}$ is always true for $n \geq 1$.

6.4.3 Sum of two sawtooth waves

According to previous subsection, the sum of the two sawtooth waves is:

$$\sum_m C_0^{sl} + \sum_m C_0^{sl2} = 0 \tag{6.63}$$

$$\sum_m C_n^{sl} + \sum_m C_n^{sl2} = C_n^{PWM} + \sum_m \frac{iAT}{n^2\pi^2 D_m} \sin(n\pi \frac{D_m}{T}) e^{-i2\pi n \frac{t_m}{T}} - \sum_m \frac{iAT}{n^2\pi^2 D'_m} \sin(n\pi \frac{D'_m}{T}) e^{-i2\pi n \frac{t'_m}{T}} \tag{6.64}$$

98
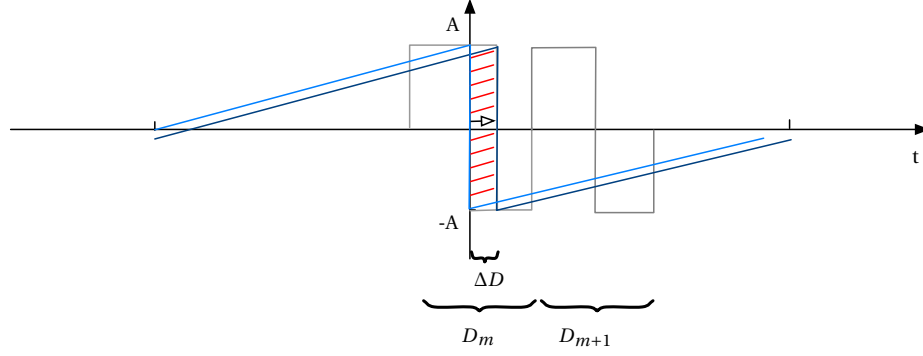
(a) Delay effect to $\sum_m \frac{A}{n\pi} e^{n\pi \frac{k_m D_m}{T}} e^{-i2\pi n \frac{t_m}{T}}$
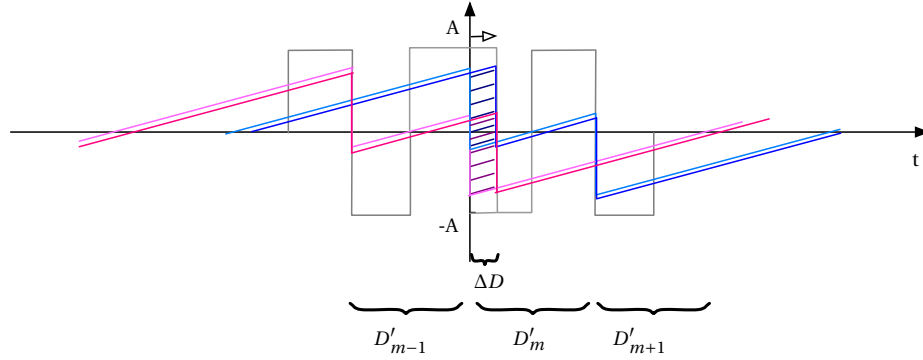
(b) Delay effect to $\sum_m \frac{iA}{n\pi} \cos(n\pi \frac{D'_m}{T}) e^{-i2\pi n \frac{t'_m}{T}}$

Figure 6.7 – Delay of ΔD for the step down of D_n

As the average value of each element is zero, the sine dependent components of the sawtooth waves reflect the average value during each element D_m or D'_m. Thus, the inverse Fourier transform of the last two terms of (6.64) is approximate to the original function $-f(t_m)$. At last, it can be concluded that the sum of two sawtooth waves represents only the harmonics of the PWM compared to original waveform $f(t_m)$.

6.5   Application on self-oscillating PWM

The PWM wave of a class-D self-oscillating amplifier is modellized in sections 6.2, the period of one element can be obtained by (6.55). Supposing $A_{n,a} - A_{n,b}$ being almost constant, we can use T_{min} to replace $\frac{A_{n,a} - A_{n,b}}{u_a k_1}$ which is around two times of the physical delay of the system. For simplicity, we suppose T_{min} is a constant for all elements in the PWM. Thus, each element has a variant duration D_m which depends only on the middle value $f(t_m)$:

$$D_m = \frac{T_{min}}{\min(\frac{k_m+1}{2}, \frac{1-k_m}{2})} \tag{6.65}$$
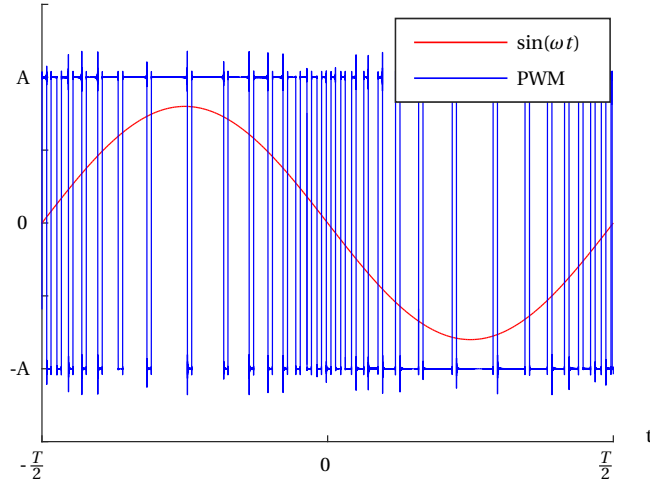
(a) PWM with its sinusoidal original function
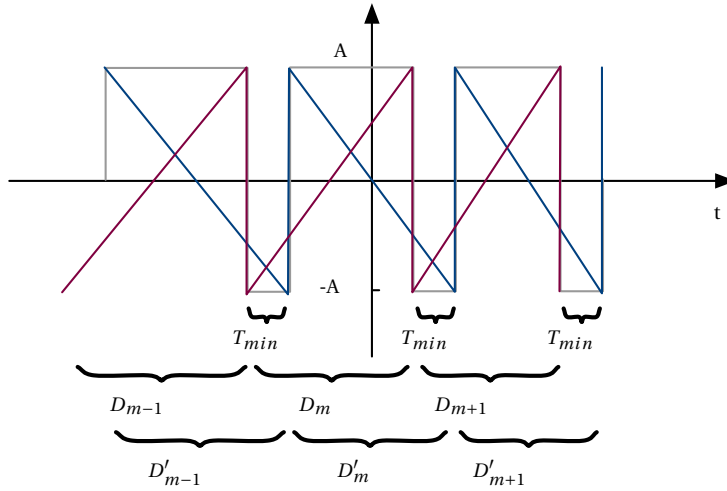
(b) Decomposition into two sawtooth waves

Figure 6.8 – PWM waveform obtained by self-oscillating amplifier

According to the nature of this kind of PWM, from Fig. 6.8b, one can notice that D_m and D'_m share the same high level part. As their low level parts also have the same value T_{min}, we have $D_m = D'_m$. Indeed, (6.65) determines the T_{min} position in an element. If $k_m > 0$, as shown in Fig. 6.8b, the T_{min} part is on the right in an element, so $D_m = D'_m$ and D'_m lags behind D_m for T_{min}. Otherwise, if $k_m < 0$, T_{min} is on the left in an element, we have $D'_{m-1} = D_m$ and D_m lags behind D'_{m-1} for T_{min}.

Thanks to this property of self-oscillating PWM, for $k_m > 0$, (6.64) becomes:

$$h_n = \sum_m C_n^{sl} + \sum_m C_n^{sl2} = \sum_m C_n^{sl}(1 - e^{i2\pi n \frac{T_{min}}{T}}) \tag{6.66}$$

Further simplifications can be made if the original signal is sinusoidal. Because the Fourier transform do not care the sequence order of a signal and the contribution of the harmonics is identical to each other in each quarter of the PWM for a sinusoidal function. The simplest expression of the harmonics becomes:

$$h_n = \sum_{m=1}^{t_m < \frac{T}{4}} C_n^{sl} (1 - e^{i2\pi n \frac{T_{min}}{T}})(1 + e^{i \frac{\pi n}{2}} + e^{i\pi n} + e^{i \frac{3\pi n}{2}}) \tag{6.67}$$

The advantage of (6.67) is that it expresses the harmonics compared to the original signal in frequency domain. The only information required is the length of each element D_m and its middle point t_m.

Supposing that the original signal form is $A\sin(\omega t)$, according to (6.65), the equation for the begining time of each element can be written as:

$$m = \int_0^{T_m} \frac{1 - A\sin(\omega t)}{2T_{min}} dt \tag{6.68}$$

Then we can obtain the theoretical values of $D_m = T_m - T_{m-1}$ and $t_m = \frac{T_m + T_{m-1}}{2}$.

Table 6.1 – THD results for three methods

Direct	Sawtooth		Simplest	
THD	THD	error	THD	error
1.4457	1.4538	0.56%	1.5041	4.0%
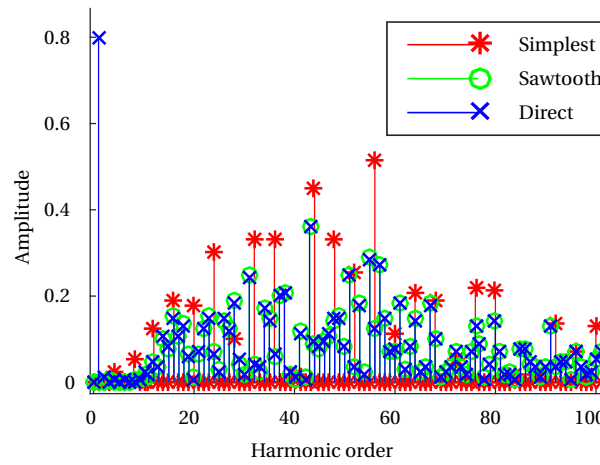
Figure 6.9 – Frequency components of PWM with three calculation methods

A simple application of this method is given with the functions shown in Fig. 6.6a. Supposing $A = 1$, $T = 1$ and $T_{min} = 0.0079$ and the original signal is $f(x) = 0.8\sin(2\pi t)$, two methods have been tested: the complete sawtooth method according to (6.64), the simplified approximative sawtooth method with (6.67). They are also compared with the direct FFT result of the PWM waveform as shown in Fig. 6.9. The non-simplified sawtooth decomposition result is nearly the one with direct transformation. Because the simplest method is $\frac{T}{4}$ periodic, it has four times less components and they have often greater values. The THD can be used to examine the signal quality. Table 6.1 shows the results and with the complete decomposition, there is only 0.5% relative error. The simplified the expression will lead to 4.0% relative error. This error mostly comes from the "connection" between each quarter period.

6.6   Output filter design reference

The non-periodic PWM signal obtained by the self-oscillating class-D amplifier is represented by $y(t)$ in Fig. 6.2. In order to design the low-pass filter, the analytical method can then be applied to calculate the expected spectral distribution of the signal. As the PWM depends also on the input amplitude, we can plot the spectrum with the sinusoidal signals under different amplitudes.
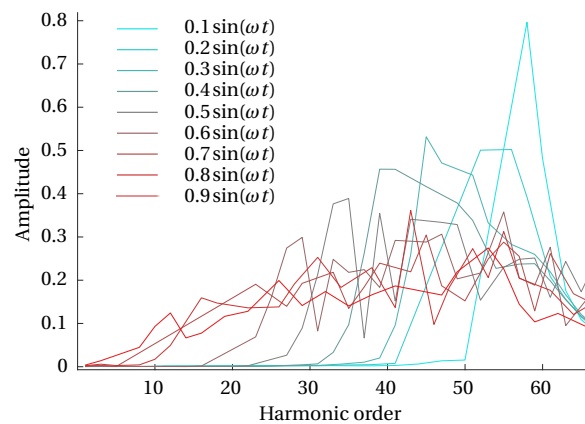
Figure 6.10 – Frequency envelops for different original signal amplitudes

In Fig. 6.10, each line represents a frequency envelop for an original signal with the same frequency but different amplitude coefficients from 0.1 to 0.9 (In order to avoid too many details in the graph representation, envelops are generated by linking local maximal spectral values to show the shape of the spectral distribution). The more important the amplitude is, the flatter the envelop is. The peak values for harmonic frequencies also change in function of the original signal amplitude. In this case, a low pass filter should be carefully designed to achieve an optimal performance of the system. With the developed method, this graph can be obtained faster and easier to deal with the non-periodic PWM.

A RLC filter can be inserted at the output stage shown in Fig. 6.1. As it is a second order low-pass filter, the cutoff frequency is:

$$f = \frac{1}{2\pi\sqrt{L_o C_{load}}} \tag{6.69}$$

and the damping ratio is:

$$\zeta = \frac{R_o}{2}\sqrt{\frac{C_{load}}{L_o}} \tag{6.70}$$

According to Fig. 6.10, one can use the filter transfer function to directly calculate the output spectrum. Or simply to use the graph to decide a cutoff frequency on the basis of the highest amplitude used in the real application, which leads to determine all the parameters for the filter.

As the piezoelectric actuator is equivalent to a capacitive load, it can be used as part of low pass filter. If its value is smaller than C_{load}, another capacitor can be added in parallel to the actuator in order to meet the designed cutoff frequency.

6.7 Hardware design and results

6.7.1 Requirements

The requirements mainly depend on the parameters of the actuator. As we have chosen the piezoelectric actuators from Noliac for our project, the working range of the piezoelectric actuator is from -60 V to 200 V and we will use it mainly from 0 to 150 V. The output waveform should be a sine wave with a frequency from 500 Hz to 20 kHz. The detailed requirements are listed in Table 6.2:

Table 6.2 – Piezolectric actuator electrical parameters

Variable	Symbol	Value
Max. limit voltage	U_{lmax}	200 V
Min. limit voltage	U_{lmin}	-60 V
Max. operating voltage	U_{max}	150 V
Min. operating voltage	U_{min}	0 V
DC offset	U_{offset}	0 V to 100 V
Capacitance	C_d	75 or 300 nF
Resistance	R_s	5Ω (1 kHz)
Number of piezoelectric actuators	n	1

6.7.2 Parameters

The parameters of the circuit are determined according to the functional range of each component. For example, the integrator utilises an amplifier SN10502, it is powered with ±5 V and the maximum value at the output of the integrator should be smaller than 5 V in normal operation. With the respect to practical restriction and theoretical requirement (such as (6.51)), a possible configuration is given in Table 6.3. The design is given in Appendix C.1

Table 6.3 – Piezolectric actuator electrical parameters

Variable	Symbol	Value
First order capacitor	C_1	2 nF
Second order capacitor	C_2	2 nF
Second order resistor	R_2	330 Ω
Input resistor	R_i	1 kΩ
Feedback resistor	R_f	1 kΩ
Output filter resistor	R_o	4.7 Ω
Output filter inductor	L_o	68 uH
Load capacitor	C_L	400 nF
System total delay time	t_d	350 ns

6.7.3 Circuit tests

Fig. 6.11 shows the realised self-oscillating class D amplifier. It equips two IRFB4137 MOSFET which can work up to 300 V with a very small resistance (R_{DS} max. 69 mΩ) between drain and source, which leads also to a maximum current of 38 A. The gate drive is an IRS2011 from International Rectifier. The main parameter we look at is the propagation delay, which is a very important parameter for self-oscillating amplifiers, as it significantly affects the delay parameter of the whole system. The IRS2011 has the shortest delay (max. 80 ns) compared to other similar products and allows the drive having a higher switching rate.

The following tests on the duty ratio, THD and bode diagram have been carried out to demonstrate the effectiveness of the design.

Duty ratio test   First, the experiments are carried out to test the relationship between the switching period and the duty ratio (modulation index). Fig. 6.12 shows both the experimental and analytical results. Because the first order system and second order system are both commonly used in practice, we made a comparison of the two cases. We have found that the first order system has a shorter switching time compared to the second order system. In both cases, the duty ratios are correctly predicted and the relative error is lower than 18%. The results show that the drive works as expected.
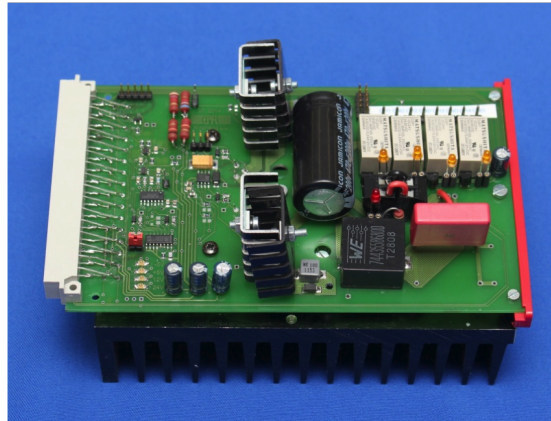
Figure 6.11 – Self-oscillating class-D amplifier for driving piezoelectric actuator
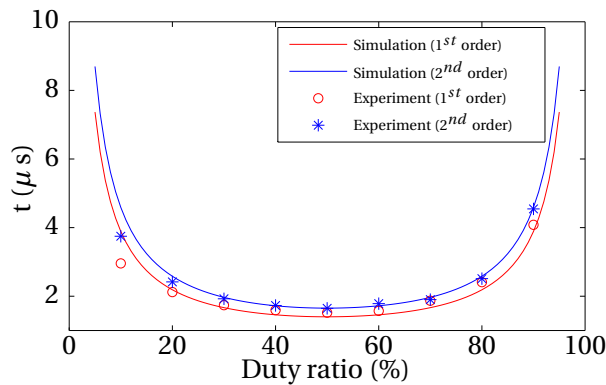
Figure 6.12 – Duty ratio results

THD test   In order to study the quality of the output signal, we can use a THD test. Firstly, the simulation results in Fig. 6.13a show the first order system has an advantage at low frequency. It can be explained by its higher switching frequency shown in duty ratio tests. But the experimental results presented in Fig. 6.13b show that the results of both cases are similar. At around 5 kHz, the second order drive has even less distortion. We can notice that in the experiments, the value of THD is twice the one in the simulations. One of the possible reasons is that the piezo is indeed not an ideal capacitor and therefore affects the result. According to the experimental results, we find the second order self-oscillating amplifier is more interesting and we decided to use it for the following experiments.

Bode diagram   The bode diagram represents properties of the amplifier with regard to frequencies. A second order drive has been used in this test and its results are given in Fig. 6.14. The drive is tested in its working frequency range from 100 Hz to 20 kHz. According to parame-

(a) THD simulation results (b) THD experimental results
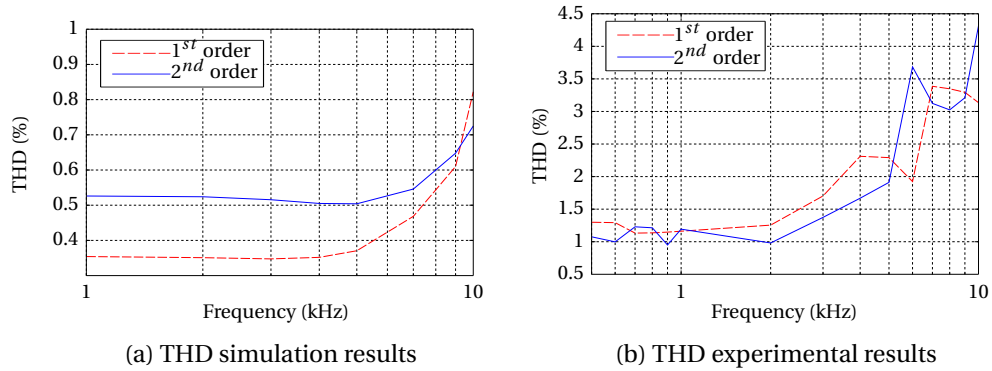
Figure 6.13 – THD results
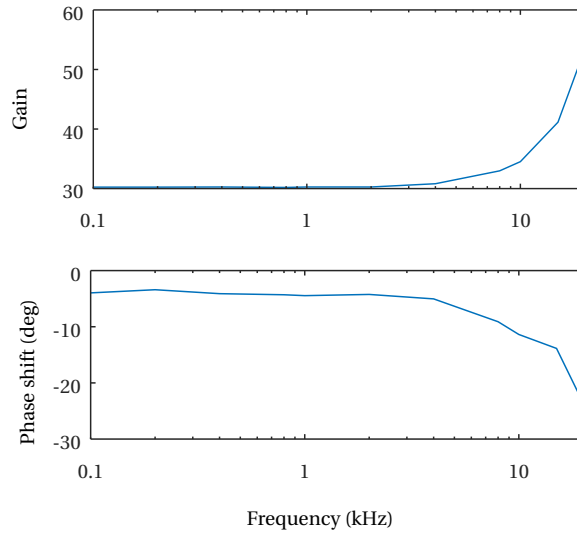
Figure 6.14 – Bode diagram of the second order amplifier

ters of the drive given in Table 6.3, the cutoff frequency is around 30 kHz. Due to the nature of the second order low-pass output filter, the output signal is underdamped ($\zeta = 0.18$). One can clearly see the gain is 30 times at the beginning, and after 10 kHz, it increases. It is possible to reduce the underdamped effect by increasing the resistance value of R_o, however, the resistor will waste a lot of energy in that case. As a result, we decided to use current configuration which allows to provide a compromised solution.

6.8 Conclusion

A theoretical analysis has been carried out for delay based class-D amplifier. The model for second order system has shown interesting properties including stability criteria and modulation index. The result obtained has proved the existence of a stable functional point under stability criteria. The analytical method introduced can be also applied in other studies

of any delay based class-D amplifiers. It can help giving a rigorous mathematical result about the behaviour of such system.

In parallel, an other analytical method has been proposed for the spectrum analysis of the non-periodic PWM signal. It allows us to understand the system output easier and to find the full potential with ideal conditions. This study has provided a new view of the PWM waveform and has proposed a sawtooth decomposition to represent its harmonics. The equivalence between the two waveforms has been theoretically proved. Admitting approximations, a very simple expression has been obtained in order to study self-oscillating amplifiers. Numerical experiments has have been realised to demonstrate the effectiveness of this method.

Finally, a practical design of a piezoelectric delay based class-D drive and its parameters have been given. This latter has verified the expected modelling. Furthermore, a compromised choice of R_o should be made taking into consideration both the performance requirements and the power consumption limits.

Relative publications to the chapter

- X. Liu, P. Germano, Y. Civet and Y. Perriard, "Design of a self-oscillating class D power amplifier for piezoelectric actuators," *2014 17th International Conference on Electrical Machines and Systems (ICEMS)*, Hangzhou, 2014, pp. 3386-3391.

- X. Liu, P. Germano and Y. Perriard, "Non periodic pulse width modulation spectral analysis with approximate decomposition of the signal," *2016 19th International Conference on Electrical Machines and Systems (ICEMS)*, Chiba, 2016, pp. 1-4.

7 Experiments

Contents

This chapter gives experimental results of applications using the time reversal method. Firstly, the excitation pulse position detection is introduced for both single excitation case and multiple excitations case. Then this chapter focuses on the creation of a pulse vibration on a beam. The approche adopted follows instructions presented in previous chapters.

7.1 Introduction

The objective of experiments is to verified previous theoretical modelling of the system. As discussed in Section 4.5, a beam can reduce the two dimensional problem to a one dimensional problem and it is also friendly for simulations in terms of the cost of time and computation resources. Hence, a "narrow" plate has been chosen as the target for our experiments.

The experiments will use an aluminum beam of 250 x 16 x 2 mm^3 with one multilayer piezoelectric actuators of size 10 x 10 x 2 mm^3 (from Noliac^{TM}) glued on the bottom of the plate. The position of the piezoelectric actuator is at one-fourth of the length of the beam (67.5 mm).
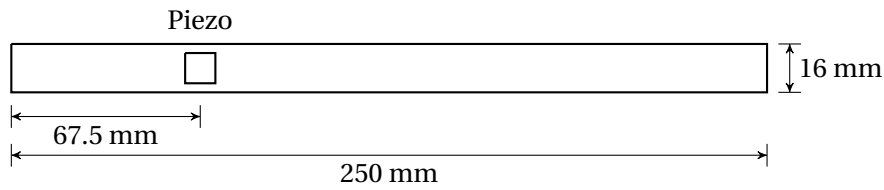
Figure 7.1 – Bottom view of the beam used for experiments

7.2 Excitation pulse position detection

In order to detect the position of an acoustic emission source, the first step is to create the reversed signal. According to previous studies in acoustic source location, we use a pencil to generate an excitation pulse on the beam [29]. The setup of experiment is illustrated in Fig. 7.2. As the piezoelectric actuator works as a sensor, an oscilloscope (LeCroy LT224) is connected to record the signal.
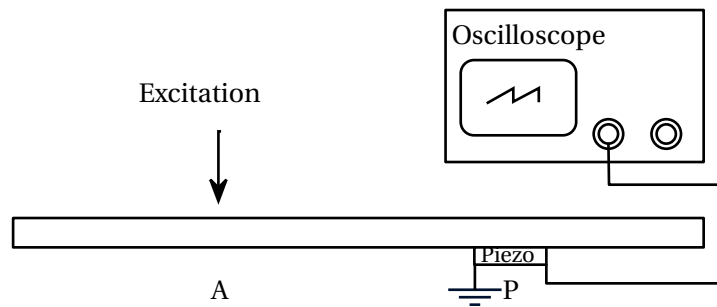
Figure 7.2 – Piezoelectric sensor connected to an oscilloscope for the detection of excitation pulse position

In this expriment, the excitation has been applied at 100 mm (0.4 of the total length) on the top surface of the beam. The signal captured by the piezoelectric actuator is recorded during 2 ms. The result is shown in Fig. 7.3. It is normalised with a maximal amplitude of one and then compared to the theoretical voltage result according to (4.10). The theoretical result takes also

into consideration of damping effect which will be discussed later.

Figure 7.3 – Comparison of the signal received by piezoelectric sensor obtained by experiment and by theoretical calculation

In Fig. 7.4, Fourier Transform results of signals obtained by expriments and by theoretical calculation are given. It can be noticed that they have nearly the same spectrum distribution. As (4.10) contains a $\sin(\omega_n t)$, their coefficients of Fourier Transform represent the product of damping depending terms and eigenmode depending terms. Although there is some differences (for example around 14 kHz in Fig. 7.4) between the spectrum, the theoretical analysis can almost predict the results and one can expect the time reversal method will give a right answer for the excitation position.
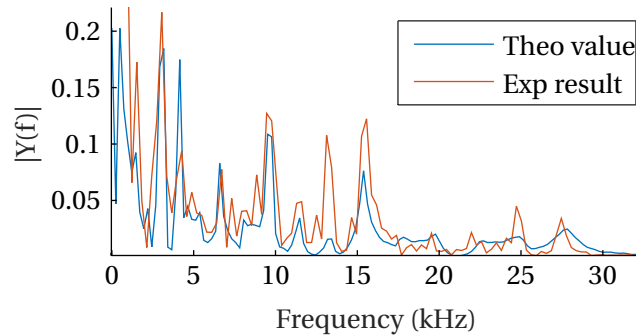
Figure 7.4 – Comparison of FFT coefficients of signals received by piezoelectric sensor

According to the time reversal method, the voltage signal obtained by experiments is then given to a simulation under Ansys$^{\text{TM}}$. The FEM model is made with the real dimension of the beam and piezoelectric actuator. The parameters of piezoelectric actuator are given by [90]. The result is shown in Fig. 7.5. In the simulation, the signal duration used is 1 ms (half of the total duration of recorded signal). It can be found that the maximum peak takes place exactly at 1 ms and at 0.4 of the normalised length.
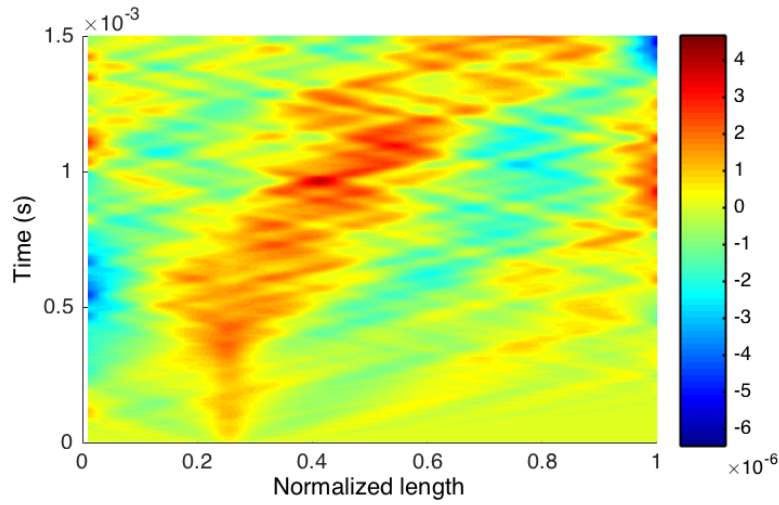
Figure 7.5 – Simulation with the signal obtained from an experiment where the excitation pulse is applied at 0.4.
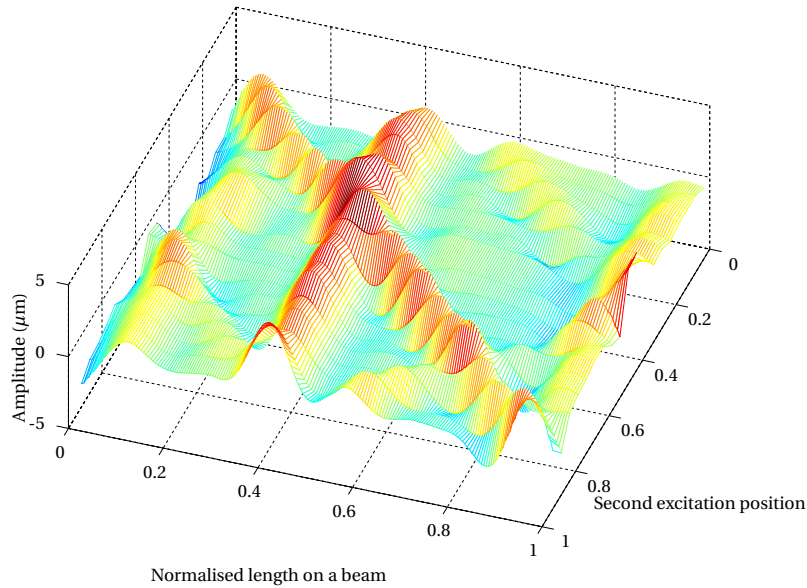
Figure 7.6 – One excitation at 0.4 and another one at from 0.05 to 0.95

7.3 Multiple excitation pulses position detection

The multiple excitation pulses positions detection is a little bit more complicated. Because of the superposition of associated peaks and measurement errors, it could be difficult to find a best solution. However, for our application to detect parts dropping positions, because they drop from a same height, the impact should be at same level for all the parts. Thus, we are mostly interested the resolution of this method to separate two positions of peaks.

This experiment is carried out only by simulation. Supposing we always have a piezoelectric actuator glued at 0.25, two excitation pulses are simultaneously created. One at position 0.4, the other varies its position from 0.05 to 0.95. The result is obtained by FEM simulation as shown in Fig. 7.6. It can be noticed, while the distance between two excitations is less than 0.1, it becomes difficult to distinguish them. This distance is equal to the size of the piezoelectric actuator and thus the length of the created pulse. This property can also be confirmed by the Nyquist-Shannon sampling theorem.

7.4 Pulse generation

7.4.1 Combination of the responses

The input signal is currently generated by our analytical model. As analysed in previous section, the theoretical waveform has nearly the same spectral characteristic as experimental result. Because the cancellation will use the responses at several positions, it is much easier to obtain them by theoretical calculation than by experiments. According to Section 5.3.3, we can use a combination of responses at $x_1 = 0.4$, $x_2 = 0.1$, $x_{3,+} = 0.9 + \frac{2.59}{k_n} = 0.9323$ and $x_{3,-} = 0.8677$ where $k_n = (25 + \frac{1}{2})\pi = 80.11$. The signal generated is plotted in Fig. 7.7.
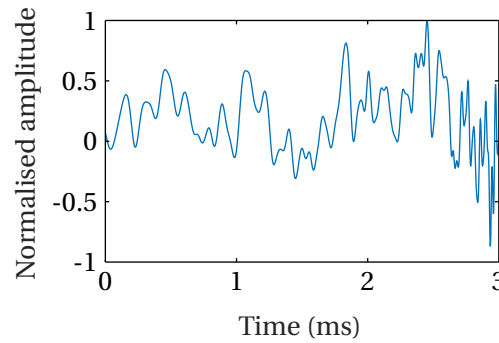
Figure 7.7 – Signal generated for restoring a pulse vibration without associated peaks

7.4.2 Damping ratios

The damping ratios can be obtained by measuring the impedance of the piezoelectric actuator before mounted and after mounted to the plate. Measurement results is shown in Fig. 7.8, each red peak represents an eigenmode. As there is an offset in high frequency range, the equivalent circuit can be referred to (3.40) and then parameters of the piezoelectric actuator equivalent model can be obtained $k_{ir,1} = 0.2$, $k_{ir,2} = 1383$, which is in black in Fig. 7.8. Then the damping ratio of each mode can be deduced. Several results corresponding to most important peaks are listed in Table 7.1.
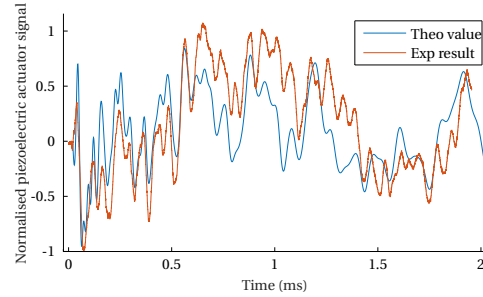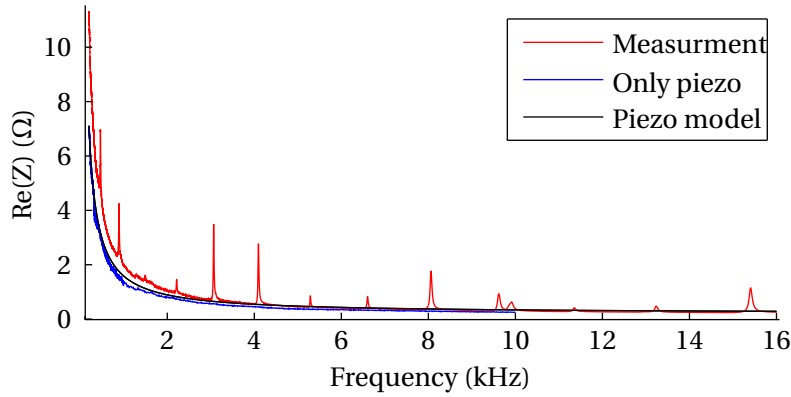
Figure 7.8 – Comparison of the signal received by piezoelectric sensor obtained by experiment and by theoretical calculation

7.4.3 Time reversal duration

According to (5.20), the final amplitude is depending on the damping related term: $\frac{1-e^{-2\zeta_n\omega_n T}}{4\zeta_n\omega_n}$. $\zeta_n\omega_n$ plays and important role for displacement amplitude and reverse signal duration. Hence, it is interesting to compare this product for different frequencies. In Table 7.1, one can notice the 3.06 kHz mode has the lowest $\zeta_n\omega_n$ value. Despite of this mode, 6.52 kHz mode is a strongest one and has a relatively low product. It should be one of the most important modes which can determine the duration for the displacement amplitude saturation.

Table 7.1 – Damping ratio results and mode amplitude against signal duration

Frequency (kHz)	ζ_n	$\zeta_n\omega_n$	T (ms) for x% Amplitude			
			x=50	x=90	T=2	T=5
0.462	0.0431	125.1	2.8	9.2	39.4	71.4
0.884	0.0219	121.6	2.8	9.5	38.5	70.4
3.06	0.0032	61.5	5.6	18.7	21.8	46.0
6.52	0.0048	196.6	1.8	5.9	54.4	86.0
9.68	0.0114	686.2	0.5	1.7	93.6	99.9
15.3	0.0053	509.5	0.7	2.3	87.0	99.4
24.8	0.0050	779.1	0.4	1.5	95.6	100.0
53.0	0.0045	1498.5	0.2	0.8	99.8	100.0

For the frequencies above 6.52 kHz, they all have high $\zeta_n\omega_n$ values. All of them will reach 90% saturation in about 2 ms. The rest will reach this level at 10 ms where 6.52 kHz mode will reach 90% at 5.9 ms. As a result, we can wait for about 2 ms to use up nearly all the potential of high frequency modes. Then, between 2 ms and 5 ms, it is mainly the 6.52 kHz mode which contributes. After that, it lasts only the low frequency modes which can still increase the final amplitude but very limited.
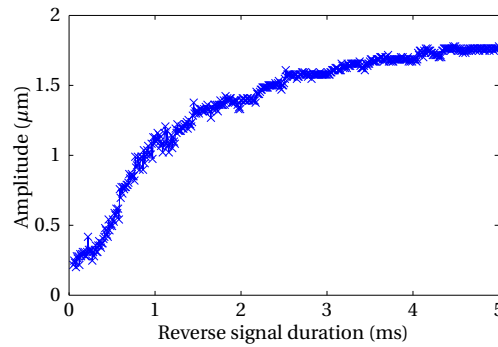
Figure 7.9 – Displacement at position 0.4 (100 mm) in function of reverse time duration T

The measurement is shown in Fig. 7.9. As analysed previously, for a duration less than 2 ms, the amplitude vigorously increases if the duration increases. Then it will reach a saturation. Thus, in practical application (for our case), the total duration should be limited to 5 ms, because it will use up most "efficient" eigenmodes.

7.4.4   Result of pulse creation

A Laser Doppler Vibrometer is used to measure the displacement of the beam surface as shown in Fig. 7.10. The vibrometer is placed on a moving plate, which allows to scan the entire length of a beam.

Fig. 7.11 shows the 3D plot of the displacement in function of time and positions on the beam. As predict in by analytical model, the maximum is obtained at 2 ms (signal begins
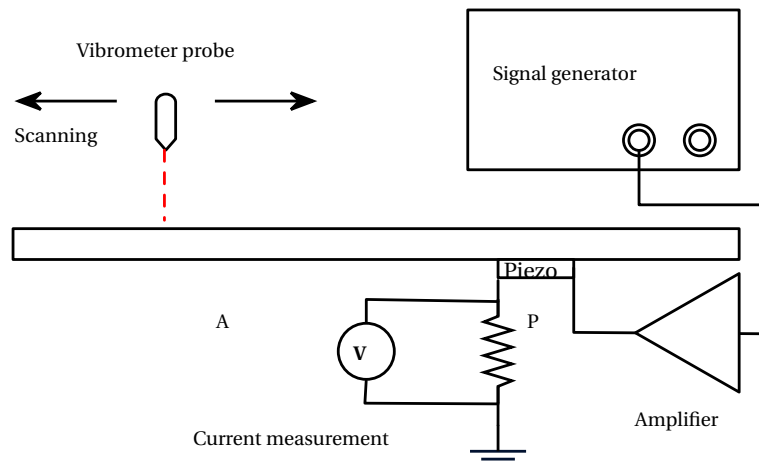
Figure 7.10 – Experiment set-up for beam surface displacement scanning. The vibrometer probe can be moved along the beam with an increment of 0.5 mm. At each position the measurement is triggered by the input signal for the piezoelectric actuator.

at 0 ms) and 100 mm. The peak value is 1.4 μm. Although at other positions, there are also inevitable displacement on the surface, their amplitudes are smaller than the one at 100 mm. This experiment demonstrates the feasibility of creating a pulse vibration at a specific position, which allows to interact with a part on the plate at a specific position only with one piezoelectric actuator.
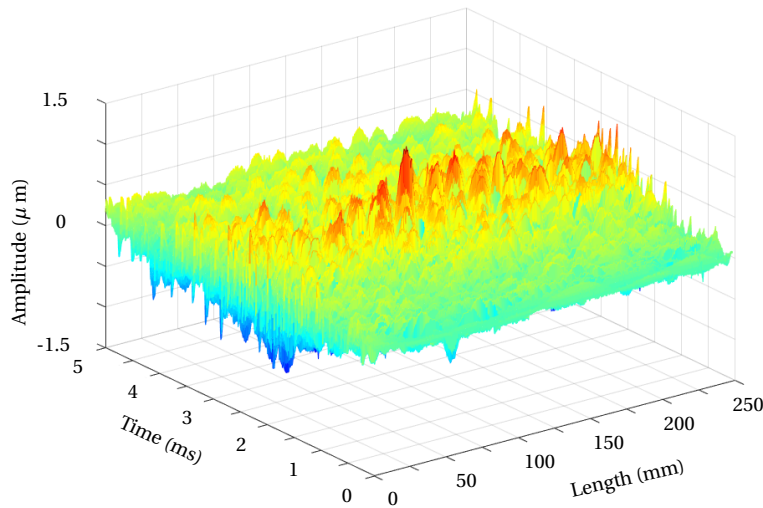
Figure 7.11 – 3D visualisation of the beam surface displacement according to the scanning of a laser doppler vibrometer. The maximum value takes place at 100 mm and at 2 ms

7.5   Conclusion

This chapter presented experiments applying time reversal method for excitation pulse detection and pulse vibration creation. The detection example shows it is an effective method which can find out when and where the excitation applied by investigating the maximum value of the restored wave. Multiple excitations detection can also be realised, but the position between two excitation source should not be too close. The resolution depends on the wave length of the restored wave, thus it depends on the size of the piezoelectric element used in experiments.

Pulse vibration creation is also realised using the proposed method. The duration of time reversal process is also discussed. The longer the duration is, the greater the amplitude is, however, due to saturation, above a certain length, the increase of the amplitude becomes insignifiant. As a result, the duration should be selected wisely in order to find a compromise between the increase of amplitude and the waiting time for a pulse. Finally, a scanning on the surface of a beam validate the pulse creation using the time reversal method.

8 Conclusion

A new design of a working plate for a part feeder utilises piezoelectric actuators to create vibrations. It can work at relative high frequencies which is in the range where the eigenmodes of the plate can be used. Being an innovative attempt to solve the random movement problem when separating/orienting parts on a plate using eigenmodes, the study of such system was done mainly by simulations or experimental trials and it lacks an analytical modelling.

A piezoelectric element can be used both as sensor or as actuator. The state of the art has shown the possibility to detect acoustic emission sources or create vibrations with a piezoelectric system. Among all possible technics, the time reversal method has been found to be the most interesting one for these two tasks. A few related works reported positive results but lack of a complete theoretical analysis. As a result, a more complete modelling is necessary to clarify all the problems and lead to an applicable method for the design of a piezoelectric actuated working plate.

This thesis has accomplished a complete modelling for solving these problems. According to the roadmap shown in Fig. 8.1, the modelling of the whole system has been divided into several subproblems and they have been individually solved during this study. The experiments have shown the effectiveness for the detection and wave creation using the time reversal method.

8.1   Original contributions

The original contributions of this work are listed as follows:

Piezoelectric actuator equivalent model and fast damping ratio test. Normally, damping ratios are obtained by directly measuring the displacement on a plate. In our study, as the piezoelectric actuator and the working plate constitute a coupled system, it has been proved that the damping ratios can be determined by the measurement of the impedance of the piezoelectric actuator coupled with a plate. This new method can improve the efficiency for the damping measurement. Besides, the precision of the damping ratio measurement using this method depends on the real part of the impedance of the piezoelectric actuator. A precise
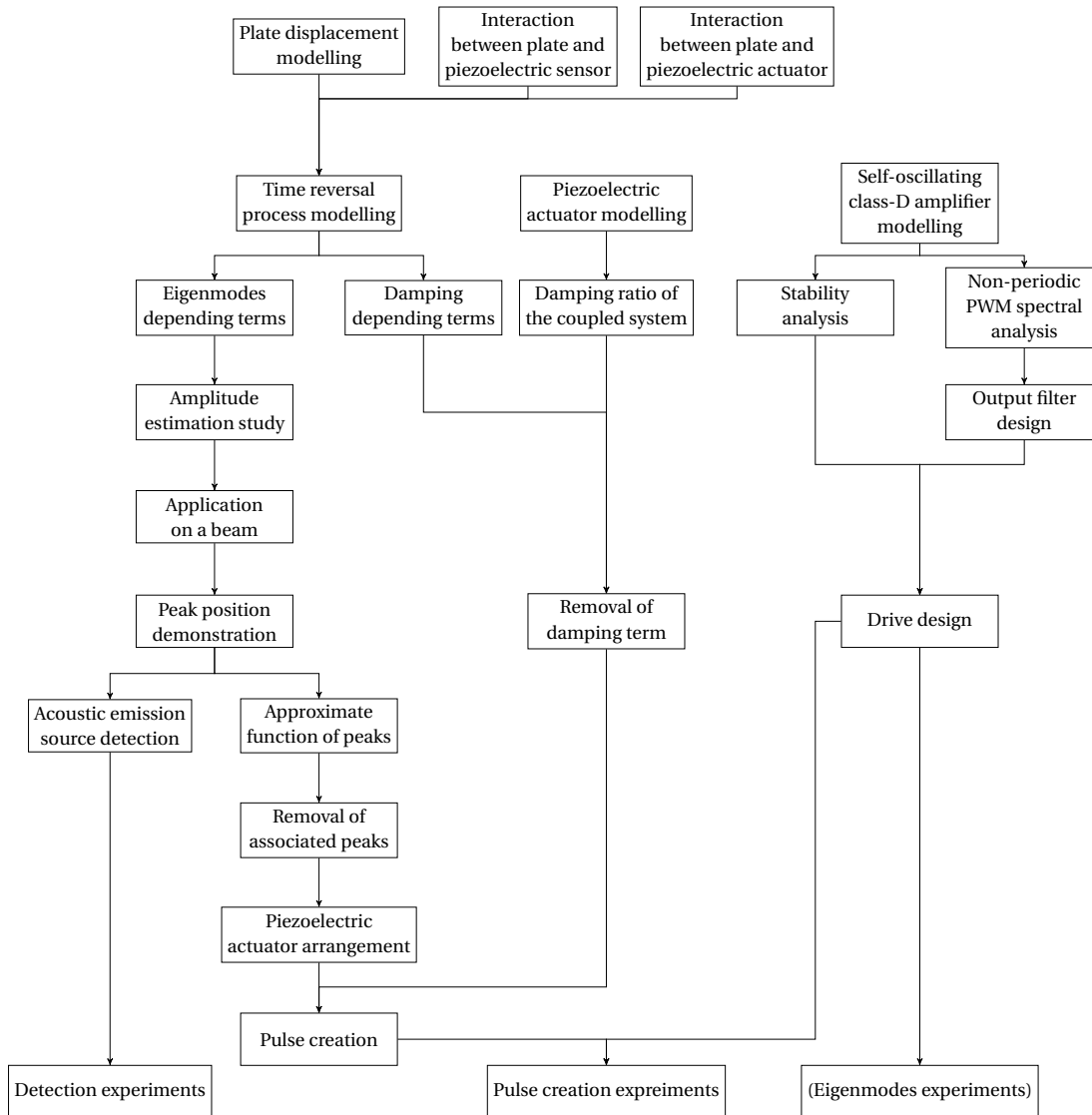
Figure 8.1 – Study roadmap of this thesis

model of this part is crucial for the precision of the result. However, the existing model cannot properly present the characteristic curve obtained from measurement. A new piezoelectric equivalent model has been then proposed, which allows to fit the measurement curve both in high frequency range and in low frequency range. Thus, the development of this new model makes our damping ratio measurement applicable.

Complete modelling of time reversal method. The time reversal method can be used to detect acoustic emission source positions or create vibrations on a plate. However, there were no rigorous demonstration for the results obtained by this method. In this thesis, we have analysed this problem and given a complete modelling based on the configuration using piezoelectric elements (sensor/actuator) for the time reversal process. The interaction between piezoelec-

tric elements and the plate has been firstly discussed, which has given a result which does not attenuate with regard to the order of eigenmodes. It has shown our configuration using piezoelectric elements has an intrinsic advantage compared to other solutions using directly displacement signals. Further calculation has indicated that there are several peaks appearing in the time reversal result of an excitation pulse. The most important peak has been proved that it is at exactly the same position of the original excitation pulse, which has validated the use of time reversal method for position detection.

Pulse creation using responses obtained from the time reversal method. According to results of the response obtained by applying the time reversal method, if the reversal signal of an excitation pulse is directly used for the creation of a pulse vibration, one main peak and several associated peaks will appear on the plate. However, the theoretical study in this thesis has proved it is possible to combine several responses to cancel out associated peaks and thus create a perfect pulse vibration. We have found out approximate functions to describe these peaks with two types of functions. They have allowed to find out the coefficients for cancelling associated peaks. These original results can finally give conditions for the position arrangement of piezoelectric actuators.

Self-oscillating class-D amplifier as a piezoelectric drive. In our application, due to requirements of the system, the drive should be able to provide a high supply voltage and a wide dynamic frequency range for piezoelectric actuators with a great capacitance. It is the first time, a self-oscillating class-D amplifier is used for this case. Thanks to the principle of self-oscillating, the working frequency can reach nearly the limit of switching components. The theoretical modelling has also been established to study its stability. The stability criteria have been proposed, which is useful for the selection of parameters.

Approximate expression of a non-periodic PWM signal in spectral domain. The analytical models exists for periodic PWM to obtain theoretical spectral values. However, due to the complexity of the non-periodic PWM, we noted a lack of a similar tool to study its theoretical result. In this thesis, we have proposed a method to obtain an approximate expression of the spectrum of a non-periodic PWM. In the case of using a self-oscillating class-D amplifier, this expression can be simplified thanks to its property: the shortest switching period is almost constant. This result can fill the blank for modelling non-periodic PWM signals and is useful to guide the output filter design.

8.2 Outlook and perspectives

According to the results obtained, future works can be highlighted in the following topics either to enhance the working plate or for further applications.

Working plate design. This study focuses on the basic functional principles that can be used for a working plate. For example, the generation of a pulse wave provides the possibility to generate any kind of surface displacement. However, the desired waveform of vibration

depends on the study of interactions between parts and plate, which has been discussed in [90]. Together with the other operations using single eigenmode such as general separation and orientation mentioned in [90], a new design of the working plate can be achieved by combining all these knowledges in order to create an optimised solution.

Structure health monitoring applications. One of the applications of the emission source position detection is about the structure health monitoring. The objective is to locate the position of cracks inside the material. According to the result of our study, the time reversal method requires only one piezoelectric actuator, because it makes use of all eigenmodes information contained within the received signal. Compared to other methods using only arrival delay information of signals, the time reversal method can theoretically give a more precise result. A study on this subject would be interesting to improve their current method.

Tactile applications. If dropping parts are replaced by a finger, the plate becomes a tactile input device and the vibration created on the plate is equivalent to a feedback for the user. The advantage of the time reversal method is that it allows turning any rigid flat surface (table, window) to a tactile input device if a piezoelectric sensor/actuator is glued. The precision depends on the size of the piezoelectric sensor which can be adjusted according to the application environment. As humain-machine interfaces become more and more important for "smart" devices, it would be interesting to apply our results in this field.

A Piezoelectric actuator equivalent circuit parameter expressions

The general method to calculate the model's parameters have been given in Section 3.5. Supposing the vector $\mathbf{R_m}$ and vector $\mathbf{X_m}$ are measured data of dimension $n \times 1$ at frequencies $\boldsymbol{\omega_m}$, the objective is to find the $R(\boldsymbol{\omega_m})$ which can satisfy the expression (A.1).

$$\underset{k_1,\dots,k_q}{\arg\min}(\mathbf{R}_m - \mathbf{R}(\boldsymbol{\omega_m}))^T(\mathbf{R}_m - \mathbf{R}(\boldsymbol{\omega_m})) \tag{A.1}$$

(a) Kim's model   (b) Park's model   (c) Guan's model
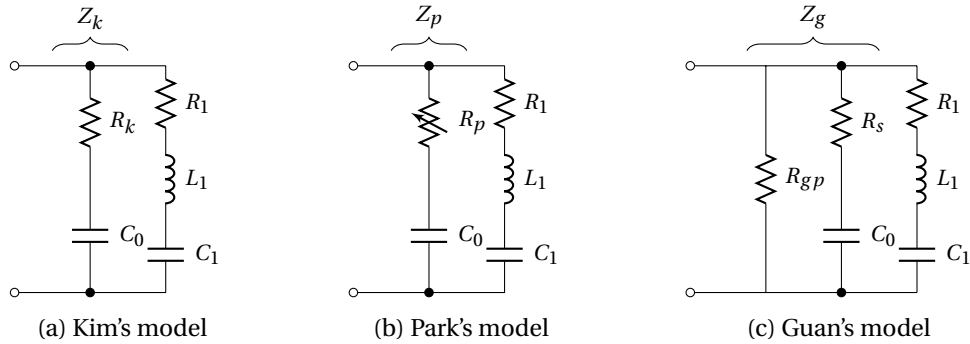
Figure A.1 – Unloaded piezoelectric ceramic models

A.1 Constant resistor model (Kim's model)

Kim's model is shown in Fig. A.1a. It contains only one constant resistor in series with the capacitor [54]. We define that $\mathbf{V}_1 = [1\dots1]^T$ is a vector of n constant elements. The optimum value of its resistance is the average of all the measurement which can be expressed in (A.2)

$$R_k = k_k = \frac{\mathbf{V}_1^T\mathbf{R_m}}{n} \tag{A.2}$$

A.2 Power-law resistor model (Park's model)

In Park's model (Fig. A.1b), the variable resistor is supposed to be in the form of a power-law function (A.3), where $k_{p,1}$ and $k_{p,2}$ are two coefficients to be determined.

$$R_p(\omega) = k_{p,1}\omega^{k_{p,2}} \tag{A.3}$$

Applying the partial derivatives of (A.1) at minimum point and defining that $\boldsymbol{\omega}^{\{x\}} = [\omega_1^x...\omega_n^x]^T$, we have:

$$\sum_{i=1}^{n}(R_{m,i} - k_{p,1}\omega^{k_{p,2}})\omega^{k_{p,2}} = 0 \tag{A.4a}$$

$$\sum_{i=1}^{n}(R_{m,i} - k_{p,1}\omega^{k_{p,2}})k_{p,1}\omega^{k_{p,2}}\log\omega = 0 \tag{A.4b}$$

where ∘ stands for Hadamard product operator which can be defined as $\mathbf{X} \circ \mathbf{Y} = [x_1 y_1 \ldots x_n y_n]^T$.

Because (A.4) forms a transcendental equation system, it can only be solved by a numerical method. If we eliminate $k_{p,1}$, we can find an equation only with $k_{p,2}$. The problem can then be transformed to (A.5a). Once $G(k_{p,2}) = 0$ is numerically solved, $k_{p,1}$ can also be determined by (A.5b).

$$G(k_{p,2}) = \frac{\mathbf{R_m}^T\boldsymbol{\omega_m}^{\{k_{p,2}\}}}{\mathbf{R_m}^T(\boldsymbol{\omega_m}^{\{k_{p,2}\}} \circ \log\boldsymbol{\omega_m})} - \frac{\boldsymbol{\omega_m}^{\{k_{p,2}\}^T}\boldsymbol{\omega_m}^{\{k_{p,2}\}}}{\boldsymbol{\omega_m}^{\{2k_{p,2}\}^T}\log\boldsymbol{\omega_m}} = 0 \tag{A.5a}$$

$$k_{p,1} = \frac{\mathbf{R_m}^T\boldsymbol{\omega_m}^{\{k_{p,2}\}}}{\boldsymbol{\omega_m}^{\{k_{p,2}\}^T}\boldsymbol{\omega_m}^{\{k_{p,2}\}}} \tag{A.5b}$$

Another possible solution is to transform (A.3) into a linear form. Taking logarithm on both sides of (A.3), we obtain (A.6).

$$\log R_{pl}(\omega) = \log k_{pl,1} + k_{pl,2}\log\omega \tag{A.6}$$

Using standard linear regression method, the estimated parameters can be expressed as in (A.7).

$$\begin{bmatrix} \log k_{pl,1} \\ k_{pl,2} \end{bmatrix} = \begin{bmatrix} n & \mathbf{V}_1^T\log\boldsymbol{\omega_m} \\ \log\boldsymbol{\omega_m}^T\mathbf{V}_1 & \log\boldsymbol{\omega_m}^T\log\boldsymbol{\omega_m} \end{bmatrix}^{-1} \begin{bmatrix} \mathbf{V}_1^T \\ \log\boldsymbol{\omega_m}^T \end{bmatrix} \log\mathbf{R_m} \tag{A.7}$$

The advantage of the linear transformation is that we can avoid solving the transcendental

equation and all the parameter can be explicitly expressed. However, it is not the optimal solution in term of least-squares before transformation.

A.3 Two resistors model (Guan's model)

As in Fig. 2.7c, Guan's model uses two resistors: R_s in series with C_0 and they are in parallel with the second resistor R_{gp}. Applying Laplace transform to represent its impedance, then, separating the real part and imaginary part, we can find the following relation as shown in (A.8).

$$Z_g(s) = \frac{R_{gp}R_s(R_{gp} + R_s) - \frac{R_{gp}}{s^2 C_0^2} + \frac{R_{gp}^2}{sC_0}}{(R_{gp} + R_s)^2 - \frac{1}{s^2 C_0^2}} \tag{A.8}$$

Replacing s by $j\omega$, firstly for the imaginary part, we have (A.9). Assuming that R_{gp} is much bigger than R_s and ω is much bigger than $\frac{1}{(R_{gp}+R_s)C_0}$, we find the imaginary part being approximately the same as other models. Thus we can implement the same method to calculate the value of C_0.

$$X_g(\omega) = -\frac{\frac{\frac{R_{gp}^2}{(R_{gp}+R_s)^2}}{\omega C_0}}{1 + \frac{\frac{1}{(R_{gp}+R_s)^2 C_0^2}}{\omega^2}} \approx \frac{1}{\omega C_0} \tag{A.9}$$

Secondly, for the real part, it can be written as in (A.10). With the same hypothesis, the formula can be simplified by ignoring the small terms.

$$R_g(\omega) = \frac{R_{gp}R_s}{R_{gp} + R_s} \frac{1 + \frac{\frac{1}{R_s(R_{gp}+R_s)C_0^2}}{\omega^2}}{1 + \frac{\frac{1}{(R_{gp}+R_s)^2 C_0^2}}{\omega^2}} \approx R_s(1 + \frac{\frac{1}{R_s R_{gp} C_0^2}}{\omega^2}) \tag{A.10}$$

According to the approximative form of its resistance, it can be easily concluded that the resistance function behind this electrical model is (A.11).

$$R_g(\omega) = k_{g,1}(1 + \frac{k_{g,2}}{\omega^2}) \tag{A.11}$$

Using the same method as described in previous section to fit the measured data by least-

squares, the expression of the two parameters are given in (A.12)

$$k_{g,2} = \frac{\mathbf{V}_1^T \mathbf{R_m} \boldsymbol{\omega_m}^{\{-1\}^T} \boldsymbol{\omega_m}^{\{-1\}} - n\mathbf{R_m} \boldsymbol{\omega_m}^{\{-2\}}}{\boldsymbol{\omega_m}^{\{-1\}^T} \boldsymbol{\omega_m}^{\{-1\}} \mathbf{R_m} \boldsymbol{\omega_m}^{\{-2\}} - \mathbf{V}_1^T \mathbf{R_m} \boldsymbol{\omega_m}^{\{-2\}^T} \boldsymbol{\omega_m}^{\{-2\}}} \tag{A.12a}$$

$$k_{g,1} = \frac{\mathbf{R_m}^T \boldsymbol{\omega_m}^{\{-2\}}}{\boldsymbol{\omega_m}^{\{-2\}^T} (\mathbf{V}_1 + k_{g,2} \boldsymbol{\omega_m}^{\{-2\}})} \tag{A.12b}$$

Comparing (A.10) and (A.11), the values of R_s and R_{gp} can then be approximated in (A.13).

$$R_s \approx k_{g,1} \tag{A.13a}$$

$$R_{gp} \approx \frac{1}{k_{g,1} k_{g,2} C_0^2} \tag{A.13b}$$

Guan's model provides an equivalent circuit with only classic passive components. This property can facilitate the simulation and integration of the piezoelectric elements. It can also be noticed, when ω is big enough, the resistance tends to R_s (or $k_{g,1}$). As a result, Kim's model is a simplified case of Guan's model at high frequency. The parameters of Guan's model are estimated under two hypothesis which are $R_{gp} \gg R_s$ and $\omega \gg \frac{1}{(R_{gp}+R_s)C_0}$. Once the results will be obtained, hypothesis would have to be validated.

B Projection of sinc function on the basis generated by eigenmodes of a beam

According to (4.44), we ignore the hyperbolical part of the eigenmodes of a beam. This approximation is valid with a n great enough on the open interval of $(0,1)$. As a result, the approximative eigenmodes of a beam can be expressed as:

$$\psi_n(x) = \sin(k_n x - \frac{\pi}{4}) \tag{B.1}$$

where $k_n = (n + \frac{1}{2})\pi$.

It is easy to verify that ψ_n forms an orthogonal basis for the inner product defined as $< \psi_n(x), \psi_m(x) >= \int_0^1 \psi_n(x)\psi_m(x)dx$.

According to (4.26), the projection of a delta function $\delta(x - x_A)$ on this basis is:

$$< \delta(x - x_A), \psi_n(x) >= \psi_n(x_A) = \sin(k_n x_A - \frac{\pi}{4}) \tag{B.2}$$

Taking a Sinc function defined as follows:

$$\text{sinc}_{A,n}(x) = \frac{\sin(k_n(x - x_A))}{\pi(x - x_A)} \tag{B.3}$$

we want to prove given a n, its projection on the basis ψ_m is equal to the projection of $\delta(x - x_A)$ on it if $m \le n$, otherwise, if $m > n$ its projection on the basis ψ_m is zero.

Proof. The proof will be done by directly calculating the projection of $\text{sinc}_{A,n}(x)$ on ψ_m.

$$< \text{sinc}_{A,n}(x), \psi_m >= \int_0^1 \text{sinc}_{A,n}(x)\psi_m(x)dx \tag{B.4}$$

$$= \int_0^1 \frac{\sin(k_n(x - x_A))}{\pi(x - x_A)} \sin(k_m x - \frac{\pi}{4})dx$$

Appendix B. Projection of sinc function on the basis generated by eigenmodes of a beam

$$
\begin{aligned}
= &\frac{1}{\pi} \int_0^1 \frac{\sin(k_n(x - x_A)) \sin(k_m x - \frac{\pi}{4})}{x - x_A} dx \\
= &\frac{1}{\pi} \frac{1}{2\sqrt{2}} \Big[(\sin(k_m x_A) + \cos(k_m x_A)) (\text{Ci}((k_m - k_n)(x - x_A)) - \text{Ci}((k_m + k_n)(x - x_A))) \\
&- (\cos(k_m x_A) - \sin(k_m x_A)) (\text{Si}((k_m + k_n)(x - x_A)) - \text{Si}((k_m - k_n)(x - x_A))) \Big]_0^1
\end{aligned}
$$

where $\text{Si}(x)$ and $\text{Ci}(x)$ are respectively sin integral function and cos integral function defined as:

$$
\text{Si}(x) = \int_0^x \frac{\sin(t)}{t} dt \tag{B.5a}
$$

$$
\text{Ci}(x) = \int_x^\infty \frac{\cos(t)}{t} dt \tag{B.5b}
$$

$\text{Ci}(x)$ is an even function. $\text{Ci}(0)$ is $-\infty$ and $\text{Ci}(x) = 0 \big|_{x \to \infty}$. We can use an approximative expression of $\text{Ci}(x)$ such that $\text{Ci}(0) = -\infty$ and $\text{Ci}(x) \approx 0$ for $x \neq 0$. Then the part of Ci in (B.4) becomes:

$$
\Big[(\sin(k_m x_A) + \cos(k_m x_A)) (\text{Ci}((k_m - k_n)(x - x_A)) - \text{Ci}((k_m + k_n)(x - x_A))) \Big]_0^1 \tag{B.6}
$$

$$
= (\sin(k_m x_A) + \cos(k_m x_A)) \Big[(\text{Ci}((k_m - k_n)(x - x_A)) - \text{Ci}((k_m + k_n)(x - x_A))) \Big]_0^1
$$

$$
= (\sin(k_m x_A) + \cos(k_m x_A)) \Big[(\text{Ci}((k_m - k_n)(1 - x_A)) - \text{Ci}((k_m + k_n)(1 - x_A)))
$$

$$
- (\text{Ci}((k_m - k_n)(-x_A)) + \text{Ci}((k_m + k_n)(-x_A))) \Big]
$$

$$
\approx \begin{cases} (\sin(k_m x_A) + \cos(k_m x_A)) [0 - 0 - 0 + 0] & m \neq n \\ (\sin(k_m x_A) + \cos(k_m x_A)) [\text{Ci}(0) - 0 - \text{Ci}(0) + 0] & m = n \end{cases}
$$

$$
= 0
$$

Similarly, $\text{Si}(x)$ is an odd function, $\text{Si}(0)$ is equal to 0 and $\text{Si}(x)$ is approximate to $\frac{\pi}{2}$ if $x > 0$ and to $-\frac{\pi}{2}$ if $x < 0$. Thus, knowing that $x_A \in (0, 1)$ the Si part of (B.4) can be written as:

$$
\Big[(\cos(k_m x_A) - \sin(k_m x_A)) (\text{Si}((k_m + k_n)(x - x_A)) - \text{Si}((k_m - k_n)(x - x_A))) \Big]_0^1 \tag{B.7}
$$

$$
= (\cos(k_m x_A) - \sin(k_m x_A)) \Big[(\text{Si}((k_m + k_n)(x - x_A)) - \text{Si}((k_m - k_n)(x - x_A))) \Big]_0^1
$$

$$
= (\cos(k_m x_A) - \sin(k_m x_A)) \Big[(\text{Si}((k_m + k_n)(1 - x_A)) - \text{Si}((k_m - k_n)(1 - x_A)))
$$

$$
- (\text{Si}((k_m + k_n)(-x_A)) + \text{Si}((k_m - k_n)(-x_A))) \Big]
$$

$$\approx \begin{cases} (\cos(k_m x_A) - \sin(k_m x_A)) \left[\frac{\pi}{2} - (-\frac{\pi}{2}) - (-\frac{\pi}{2}) + \frac{\pi}{2} \right] & m < n \\ (\cos(k_m x_A) - \sin(k_m x_A)) \left[\frac{\pi}{2} - 0 - (-\frac{\pi}{2}) + 0 \right] & m = n \\ (\cos(k_m x_A) - \sin(k_m x_A)) \left[\frac{\pi}{2} - \frac{\pi}{2} - (-\frac{\pi}{2}) + (-\frac{\pi}{2}) \right] & m > n \end{cases}$$

$$= \begin{cases} 2\pi(\cos(k_m x_A) - \sin(k_m x_A)) & m < n \\ \pi(\cos(k_m x_A) - \sin(k_m x_A)) & m = n \\ 0 & m > n \end{cases}$$

As a result, thanks to (B.6) and (B.7), one can obtain the final form of the projection on the basis:

$$< \text{sinc}_{A,n}(x), \psi_m > \approx \begin{cases} -\frac{1}{\sqrt{2}}(\cos(k_m x_A) - \sin(k_m x_A)) & m < n \\ -\frac{1}{2\sqrt{2}}(\cos(k_m x_A) - \sin(k_m x_A)) & m = n \\ 0 & m > n \end{cases} \tag{B.8}$$

$$= \begin{cases} \sin(k_m x_A) - \frac{\pi}{4}) & m < n \\ \frac{1}{2}\sin(k_m x_A) - \frac{\pi}{4}) & m = n \\ 0 & m > n \end{cases}$$

When comparing (B.2) and (B.8), one can find that they share the same result while $m < n$. If $m = n$, the projection of $\text{sinc}_{A,n}(x)$ is half of the one of $\delta(x - x_A)$. $\qquad\square$

C Circuit design

C.1 Drive schematics

The schematics of the drive are shown as follows:

Title Half Bridge Interface

Size A4

Number 1

Revision

Date: 21.11.2014   Sheet of
File: C:\Users\halfbridgeInterface.SchDoc   Drawn By: Xinchang Liu

P59 32 pin connector

TEMP	PIN1	1	2	PIN2	CURRENTOUT
12VGND	PIN3	3	4	PIN4	12V
24VGND	PIN5	5	6	PIN6	24V
5VGND	PIN7	7	8	PIN8	+5V
5VGND	PIN9	9	10	PIN10	-5V
PIEZO SENSE 2	PIN11	11	12	PIN12	PIEZO SENSE 1
PIEZO SENSE 4	PIN13	13	14	PIN14	PIEZO SENSE 3
	PIN15	15	16	PIN16	POWER GND 1
	PIN17	17	18	PIN18	INPUT H
	PIN19	19	20	PIN20	INPUT L
GND	PIN21	21	22	PIN22	INPUT SWITCH
GND	PIN23	23	24	PIN24	
GND	PIN25	25	26	PIN26	CONTROL IN 1
CONTROL IN 2	PIN27	27	28	PIN28	CONTROL IN 3
CONTROL IN 4	PIN29	29	30	PIN30	INPUT
GND	PIN31	31	32	PIN32	COMMAND H

GND

PIEZO IN

R83 Res3 49k
R84 Res3 1k

POWER GND 1

U20 AD592
1
2
3

+5VIN
5VGND R86 Res3 4.7k
TEMP

+12V
C59 Cap2 47uF
R79 Res3 3k
D40 LED2
GND

+5V
R80 Res3 1.2k
D41 LED2
C60 Cap2 47uF
GND

-5V
C61 Cap2 47uF
R81 Res3 4.7
D42 LED2
GND

+24V
R82 Res3 6k
D43 LED2
GND

+12V
D44 D Zener
GND

+5V
D45 D Zener
GND

-5V
D47 D Zener
GND

+24V
D46 D Zener
GND

P27 Header 2
1
2
150V
GND

P28 Header 2
1
2
Output
GND

PIEZO IN
R41 Res Semi 40k
D24 Diode 1N914
P25
Header 2
POWER GND

C29 Cap Semi 100pF
C28 Cap Semi 100pF
C27 Cap Semi 100pF
C26 Cap Semi 100pF
C25 Cap Poll 100uF
+24V
GND

P3
Header 2
PIEZO IN
POWER GND

P4
Header 8
PIEZO OUT 1
POWER GND
PIEZO OUT 2
PIEZO OUT 3
POWER GND
PIEZO OUT 4
POWER GND

P5
Header 5X2
PIEZO SENSE 1
PIEZO SENSE 2
PIEZO SENSE 3
PIEZO SENSE 4
POWER GND 1
PIEZO SENSE 1L
PIEZO SENSE 2L
PIEZO SENSE 3L
PIEZO SENSE 4L
POWER GND

P6
Header 5
GND
CONTROL IN 1
CONTROL IN 2
CONTROL IN 3
CONTROL IN 4

PIEZO OUT 2
K2
PIEZO IN
PIEZO SENSE 2L
+24V
P24 Header 2
Relay-DPST
R36 Res Semi 6K
D23 Diode
Q4 2N4400
R38 Res Semi 1K
R40 Res Semi 500
C88 Cap Semi 100nF
CONTROL IN 2
GND

PIEZO OUT 4
K4
PIEZO IN
PIEZO SENSE 4L
+24V
P64 Header 2
Relay-DPST
R44 Res Semi 6K
D31 Diode
Q6 2N4400
R46 Res Semi 1K
R48 Res Semi 500
C90 Cap Semi 100nF
CONTROL IN 4
GND

PIEZO OUT 1
K1
PIEZO IN
PIEZO SENSE 1L
+24V
P23 Header 2
Relay-DPST
R35 Res Semi 6K
D22 Diode
Q3 2N4400
R37 Res Semi 1K
R39 Res Semi 500
C87 Cap Semi 100nF
CONTROL IN 1
GND

PIEZO OUT 3
K3
PIEZO IN
PIEZO SENSE 3L
+24V
P26 Header 2
Relay-DPST
R43 Res Semi 6K
D30 Diode
Q5 2N4400
R45 Res Semi 1K
R47 Res Semi 500
C89 Cap Semi 100nF
CONTROL IN 3
GND

Title: Half Bridge Output Mux
Size: A4
Number: 3
Revision
Date: 21.11.2014
File: C:\Users\..\mux.SchDoc
Sheet of
Drawn By: Xinchang Liu

134

Header 4X2A
P13

RXCH1-slave
TXCH1-slave
CTSCH1-slave
RTSCH1-slave

TXCH1-master
RXCH1-master
RTSCH1-master
CTSCH1-master

R56 Res3 270
R55 Res3 270
+5V
+5V

D39
LED2
D38
LED2

R59 Res3 10K
+5V

TXCH1-master
RXCH1-master
RTSCH1-master
CTSCH1-master

PWRENCH1-master

U12 FT232RL

TXD
RXD
RTSn
CTSn
DTRn
DSRn
DCDn
RIn
CBUS0
CBUS1
CBUS2
CBUS3
CBUS4

VCCIO
VCC
USBDM
USBDP
NC
RESETn
NC
OSCI
OSCO
3V3OUT
TEST
GND
GND
GND
AGND

GND

C52 Cap Semi 100n
GND

+5V

C48 Cap Semi 1u
C47 Cap Semi 100n
C46 Cap Semi 100n
GND

J2 0481900001
MH4 MH3 MH2 MH1

R57 Res3 4.7K
R60 Res3 10K
GND

C54 Cap Semi 100n
C56 Cap Semi 100n
GND

R66 Res3 1K
3V3

U14 LVC2G74
CLK
D
Q
VCC
PRE
CLR
Q
GND
3V3
GND
GND

R62 Res3 20K
R61 Res3 20K
GND
GND
GND

RX-slave
TX-slave

U13 FT2232D

TCK
TDI
TDO
TMS
TRSTn

ADBUS0
ADBUS1
ADBUS2
ADBUS3
ADBUS4
ADBUS5
ADBUS6
ADBUS7
ACBUS0
ACBUS1
ACBUS2
ACBUS3
SI/WUA
BDBUS0
BDBUS1
BDBUS2
BDBUS3
BDBUS4
BDBUS5
BDBUS6
BDBUS7
BCBUS0
BCBUS1
BCBUS2
BCBUS3
SI/WUB
PWRENn

3V3OUT
VCCIOB
VCCIOA
VCC
VCC
AVCC
USBDM
USBDP
RSTOUTn
RESETn
XTIN
XTOUT
EECS
EESK
EEDATA
TEST
GND
GND
GND
AGND

C45 Cap Semi 1u
C49 Cap Semi 100n
3V3
GND

+5V
C44 Cap Semi 1u
R54 Res3 4,7
C50 Cap Semi 100n
+5V GND

C51 Cap Semi 100n
GND GND

R63 Res3 27
R64 Res3 2.2k
R65 Res3 1M

Y1 XTAL
C53 Cap Semi 27p
C55 Cap Semi 27p
C57 Cap Semi 100n
GND

U15 93LC46B
CS
CLK
D-IN
D-OUT
VCC
GND
3V3
GND

U16 93LC46B SOIC
CS
CLK
DI
DO
VCC
NC
NC
VSS
3V3
C58 Cap Semi 100n
GND

R67 Res3 2.2K
R68 Res3 10K
3V3

J3 0481900001
MH4 MH3 MH2 MH1
R58 Res3 27

Title: Mother Board DSP Peripherics
Size A4
Number 5
Revision
Date: 21.11.2014
File: C:\Users\...\dspPeripheric.SchDoc
Sheet of
Drawn By: Xinchang Liu
4

Mother Board DSP Interface

136

Mother Board Interaces

137

C.2 Drive layout

The layout of the drive PCB as follows:
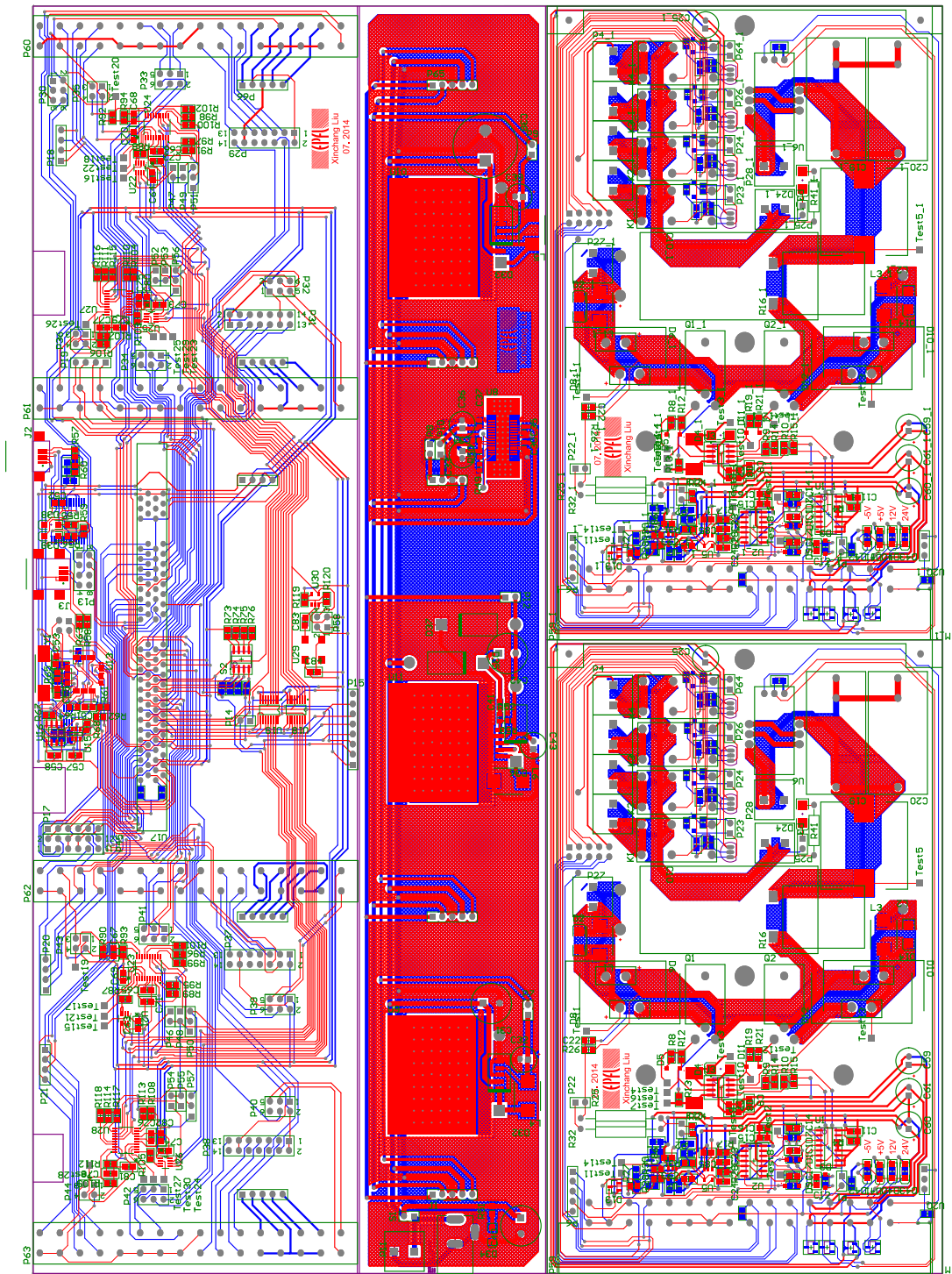
Bibliography

[1] Kodjo Agbossou, J-L Dion, Sylvain Carignan, Meftah Abdelkrim, and Ahmed Cheriti. Class d amplifier for a power piezoelectric load. *IEEE transactions on ultrasonics, ferroelectrics, and frequency control*, 47(4):1036–1041, 2000.

[2] Gregory R Ainslie-Malik. *Mathematical analysis of PWM processes.* PhD thesis, University of Nottingham, 2013.

[3] Dirk Aljets, Alex Chong, Steve Wilcox, and Karen Holford. Acoustic emission source location in plate-like structures using a closely arranged triangular sensor array. *Journal of Acoustic emission*, 28:85–98, 2010.

[4] APEX. Pa93 datasheet. *Available at http://www.apexanalog.com/wp-content/uploads/2012/08/PA93U1.pdf*.

[5] Leslie Anne Ballard, Selma Sabanovic, Jasleen Kaur, and Stasa Milojevic. George charles devol, jr.[history]. *IEEE Robotics & Automation Magazine*, 19(3):114–119, 2012.

[6] Ray Batchelor. *Henry Ford, mass production, modernism, and design*, volume 1. Manchester University Press, 1994.

[7] Matthew Geoffrey Baxter, Rhys Pullin, Karen M Holford, and Sam L Evans. Delta t source location for acoustic emission. *Mechanical systems and signal processing*, 21(3):1512–1520, 2007.

[8] A Bedford and DS Drumheller. *Elastic wave propagation.* Wiley, 1994.

[9] RC Beecher. Puma: Programmable universal machine for assembly. In *Computer vision and sensor-based robots*, pages 141–152. Springer, 1979.

[10] Marco Berkhout, Lucien Breems, and Ed van Tuijl. Audio at low and high power. In *Proc. ESSCIRC*, pages 40–49, 2008.

[11] Dina R Berkowitz and John Canny. Designing parts feeders using dynamic simulation. In *Robotics and Automation, 1996. Proceedings., 1996 IEEE International Conference on*, volume 2, pages 1127–1132. IEEE, 1996.

Bibliography

[12] Carl Blake and Chris Bull. Igbt or mosfet: Choose wisely. *Available at http://www.irf.com/ technical-info/whitepaper/choosewisely.pdf* , 4 2013.

[13] Kumen Blake. Driving capacitive loads with op amps. *Microchip, Application note*, 884, 2008.

[14] K-F Bohringer, Vivek Bhatt, and Kenneth Y Goldberg. Sensorless manipulation using transverse vibrations of a plate. In *Robotics and Automation, 1995. Proceedings., 1995 IEEE International Conference on*, volume 2, pages 1989–1996. IEEE, 1995.

[15] Geoffrey Boothroyd et al. *Assembly automation and product design*, volume 536. Cambridge Univ Press, 2005.

[16] Geoffrey Boothroyd, Corrado Poli, and Laurence E Murch. *Automatic assembly*. M. Dekker, 1982.

[17] Felix Buchi, Issa Nesnas, and Brian R Carlisle. Impulse-based, flexible parts feeder, May 2 2000. US Patent 6,056,108.

[18] Niklaus Burger. *Design of Control Electronics for an Insulin Micropump Actuator*. Master's thesis, EPFL, 2014.

[19] Michael Caine. The design of shape interactions using motion constraints. In *Robotics and Automation, 1994. Proceedings., 1994 IEEE International Conference on*, pages 366–371. IEEE, 1994.

[20] Alfredo Vázquez Carazo and Kenji Uchino. Novel piezoelectric-based power supply for driving piezoelectric actuators designed for active vibration damping applications. *Journal of Electroceramics*, 7(3):197–210, 2001.

[21] Greg C Causey, Roger D Quinn, and Michael S Branicky. Testing and analysis of a flexible feeding system. In *Robotics and Automation, 1999. Proceedings. 1999 IEEE International Conference on*, volume 4, pages 2564–2571. IEEE, 1999.

[22] Sriram Chandrasekaran, Douglas K Lindner, and Ralph C Smith. Optimized design of switching amplifiers for piezoelectric actuators. *Journal of Intelligent Material Systems and Structures*, 11(11):887–901, 2000.

[23] Yaow-Ming Chen, Ming-We Chou, and Hsu-Chin Wu. Sigma-delta modulation inverters for piezoelectric actuators. In *Industrial Electronics Society, 2007. IECON 2007. 33rd Annual Conference of the IEEE*, pages 2296–2300. IEEE, 2007.

[24] Reymond Clavel. Device for the movement and positioning of an element in space, December 11 1990. US Patent 4,976,582.

[25] Dan J Clingman and Mike Gamble. High-voltage switching piezo drive amplifier. In *5th Annual International Symposium on Smart Structures and Materials*, pages 472–478. International Society for Optics and Photonics, 1998.

140

[26] Stephen M Cox, Meng Tong Tan, and Jun Yu. A second-order class-d audio amplifier. *SIAM Journal on Applied Mathematics*, 71(1):270–287, 2011.

[27] Jr George C Devol. Programmed article transfer, June 13 1961. US Patent 2,988,237.

[28] Isaac Elishakoff. *Free Vibrations of Beams and Frames. Eigenvalues and Eigenfrequencies.* Hindawi Publishing Corporation, 2005.

[29] R Ernst and J Dual. Acoustic emission localization in beams based on time reversed dispersion. *Ultrasonics*, 54(6):1522–1533, 2014.

[30] Claude Fendzi, Nazih Mechbal, Marc Rebillat, Mikhail Guskov, and G Coffignal. A general bayesian framework for ellipse-based and hyperbola-based damage localization in anisotropic composite plates. *Journal of Intelligent Material Systems and Structures*, 27(3):350–374, 2016.

[31] Mathias Fink et al. Time-reversed acoustics. *Scientific American*, 281(5):91–97, 1999.

[32] Markus Flückiger. *Sensorless Position Control of Piezoelectric Ultrasonic Motors: a Mechatronic Design Approach.* PhD thesis, École Polytechnique Fédérale de Lausanne, 2010.

[33] Ran Gabai and Izhak Bucher. Spatial and temporal excitation to generate traveling waves in structures. *Journal of Applied Mechanics*, 77(2):021010, 2010.

[34] Victor Giurgiutiu. Lamb wave generation with piezoelectric wafer active sensors for structural health monitoring. In *Smart Structures and Materials*, pages 111–122. International Society for Optics and Photonics, 2003.

[35] Gunnar Gnad and Roland Kasper. A power drive control for piezoelectric actuators. In *Industrial Electronics, 2004 IEEE International Symposium on*, volume 2, pages 963–967. IEEE, 2004.

[36] Estill I Green. The story of q. *American Scientist*, pages 584–594, 1955.

[37] Mingjie Guan and Wei-Hsin Liao. Studies on the circuit models of piezoelectric ceramics. In *Information Acquisition, 2004. Proceedings. International Conference on*, pages 26–31. IEEE, 2004.

[38] MA Hamstad, A O'Gallagher, and J Gary. A wavelet transform applied to acoustic emission. *J. Acoust. Emiss*, 20:39–61, 2002.

[39] Yoshiki Hashimoto, Yoshikazu Koike, and Sadayuki Ueha. Transporting objects without contact using flexural traveling waves. *The Journal of the Acoustical Society of America*, 103(6):3230–3233, 1998.

[40] J Heil, I Kouroudis, B Luthi, and P Thalmeier. Surface acoustic waves in metals. *Journal of Physics C: Solid State Physics*, 17(13):2433, 1984.

Bibliography

[41] J Hensman, R Mills, SG Pierce, K Worden, and M Eaton. Locating acoustic emission sources in complex structures using gaussian processes. *Mechanical Systems and Signal Processing*, 24(1):211–223, 2010.

[42] M Hermann and W Schinköthe. Piezoelectric travelling wave motors generating direct linear motion. In *Conference Proceedings, S*, volume 200, page 203, 1999.

[43] Walter Heywang, Karl Lubitz, and Wolfram Wersing. *Piezoelectricity: evolution and future of a technology*, volume 114. Springer Science & Business Media, 2008.

[44] Donald Hoke. Ingenious yankees, the rise of the american system of manufactures in the private sector. *The Journal of Economic History*, 46(02):489–491, 1986.

[45] Karen M Holford and DC Carter. Acoustic emission source location. In *Key Engineering Materials*, volume 167, pages 162–171. Trans Tech Publ, 1999.

[46] Max-Olivier Hongler. *Chaotic and stochastic behaviour in automatic production lines*, volume 22. Springer Science & Business Media, 2008.

[47] Mikkel CW Høyerby and Michael AE Andersen. Carrier distortion in hysteretic self-oscillating class-d audio power amplifiers: Analysis and optimization. *IEEE transactions on power electronics*, 24(3):714–729, 2009.

[48] Lina Huang, Zhe Zhang, and Michael AE Andersen. A review of high voltage drive amplifiers for capacitive actuators. In *Universities Power Engineering Conference (UPEC), 2012 47th International*, pages 1–6. IEEE, 2012.

[49] H Janocha and C Stiebel. New approach to a switching amplifier for piezoelectric actuators. *energy*, 2:2, 1998.

[50] Ilpo Karjalainen, Dadi Gudmundsson, and Ken Goldberg. Optimizing robotic part feeder throughput with queueing theory. *Assembly Automation*, 27(2):134–140, 2007.

[51] Michael Karpelson, Gu-Yeon Wei, and Robert J Wood. Milligram-scale high-voltage power electronics for piezoelectric microrobots. In *Robotics and Automation, 2009. ICRA'09. IEEE International Conference on*, pages 2217–2224. IEEE, 2009.

[52] Michael Karpelson, Gu-Yeon Wei, and Robert J Wood. Driving high voltage piezoelectric actuators in microrobotic applications. *Sensors and Actuators A: Physical*, 176:78–89, 2012.

[53] Christopher Kauczor and N Frohleke. Inverter topologies for ultrasonic piezoelectric transducers with high mechanical q-factor. In *Power Electronics Specialists Conference, 2004. PESC 04. 35th Annual*, volume 4, pages 2736–2741. IEEE, 2004.

[54] Jina Kim, Benjamin L Grisso, Jeong K Kim, Dong Sam Ha, and Daniel J Inman. Electrical modeling of piezoelectric ceramics for analysis and evaluation of sensory systems. In *Sensors Applications Symposium, 2008. SAS 2008. IEEE*, pages 122–127. IET, 2008.

[55] George C King. *Vibrations and waves*. John Wiley & Sons, 2013.

[56] Syuichi Kondo, Daisuke Koyama, and Kentaro Nakamura. Miniaturaization of traveling wave ultrasonic linear motor. In *Proceedings of Symposium on Ultrasonic Electronics*, volume 30, pages 109–110, 2009.

[57] Richard Krimholtz, David A Leedom, and George L Matthaei. New equivalent circuits for elementary piezoelectric transducers. *Electronics Letters*, 6(13):398–399, 1970.

[58] Tribikram Kundu. Acoustic source localization. *Ultrasonics*, 54(1):25–38, 2014.

[59] Minoru Kurosawa, Masakazu Takahashi, and Toshiro Higuchi. Ultrasonic linear motor using surface acoustic waves. *IEEE Transactions on Ultrasonics, Ferroelectrics, and Frequency Control*, 43(5):901–906, 1996.

[60] Chun Kit Lam, Meng Tong Tan, Stephen Michael Cox, and Kiat Seng Yeo. Class-d amplifier power stage with pwm feedback loop. *IEEE Transactions on Power Electronics*, 28(8):3870–3881, 2013.

[61] Hyungjin Lee, Hyunsun Mo, Wanil Lee, Mingi Jeong, Jaehoon Jeong, and Daejeong Kim. Phase-shift self-oscillating class-d audio amplifier with multiple-pole feedback filter. *IEICE Electronics Express*, 8(16):1354–1360, 2011.

[62] Rongyuan Li, Norbert Fröhleke, and Joachim Böcker. Design and implementation of a power inverter for a high power piezoelectric brake actuator in aircrafts. In *Conf. Brazilian Power Electronics*, 2007.

[63] Rongyuan Li, N Froleke, and J Bocker. Analysis and design of a novel three-level llcc inverter supplying an airborne piezoelectric brake actuator. In *Power Electronics Specialists Conference, 2007.*, pages 2155–2161. IEEE, 2007.

[64] Byoung-Gook Loh and Paul I Ro. An object transport system using flexural ultrasonic progressive waves generated by two-mode excitation. *IEEE transactions on ultrasonics, ferroelectrics, and frequency control*, 47(4):994–999, 2000.

[65] Jingxue Lu and Ranjit Gharpurey. Design and analysis of a self-oscillating class d audio amplifier employing a hysteretic comparator. *IEEE Journal of Solid-State Circuits*, 46(10):2336–2349, 2011.

[66] John A Main, David V Newton, Lloyd Massengill, and Ephrahim Garcia. Efficient power amplifiers for piezoelectric applications. *Smart Materials and Structures*, 5(6):766, 1996.

[67] Stéphane G Mallat and Zhifeng Zhang. Matching pursuits with time-frequency dictionaries. *IEEE Transactions on signal processing*, 41(12):3397–3415, 1993.

[68] John C Mason and David C Handscomb. *Chebyshev polynomials*. CRC Press, 2002.

Bibliography

[69] A Meitzler, HF Tiersten, AW Warner, D Berlincourt, GA Couqin, and FS Welsh III. IEEE standard on piezoelectricity, 1988.

[70] E Montané, P Miribel-Català, J López-Sánchez, M Puig-Vidal, S Bota, and J Samitier. High-voltage smart power integrated circuits to drive piezoceramic actuators for microrobotic applications. 148(6):343–347, 2001.

[71] John Murdock Murphy. Analytical design and optimization of ultrasonic vibrational transducers for spinal surgery. 2007.

[72] David V Newton, John A Main, Ephrahim Garcia, and Lloyd Massengill. Piezoelectric actuation systems: optimization of driving electronics. In *1996 Symposium on Smart Structures and Materials*, pages 259–266. International Society for Optics and Photonics, 1996.

[73] Ehsan Dehghan Niri, Salvatore Salamone, and Puneet Singla. Acoustic emission (ae) source localization using extended kalman filter (ekf). In *SPIE Smart Structures and Materials+ Nondestructive Evaluation and Health Monitoring*, pages 834804–834804. International Society for Optics and Photonics, 2012.

[74] Shimon Y Nof, Wilbert Wilhelm, and H Warnecke. *Industrial assembly*. Springer Science & Business Media, 2012.

[75] Noliac. Capacitance. *Available at http://www.noliac.com/Default.aspx?ID=679*, 4 2013.

[76] NoliacAS. *Available at http://www.noliac.com/*.

[77] Chul H Park. On the circuit model of piezoceramics. *Journal of Intelligent Material Systems and Structures*, 12(7):515–522, 2001.

[78] Sebastien Perroud, Tobias Hafner, and Yves Mussard. System for supplying components, October 8 2013. US Patent 8,550,233.

[79] Gaël Pillonnet, Rémy Cellier, Emmanuel Allier, Nacer Abouchi, and Angelo Nagari. A topological comparison of pwm and hysteresis controls in switching audio amplifiers. In *Circuits and Systems, 2008. APCCAS 2008. IEEE Asia Pacific Conference on*, pages 668–671. IEEE, 2008.

[80] Søren Poulsen and Michael Andreas E Andersen. Self oscillating pwm modulators, a topological comparision. In *Power Modulator Symposium, 2004 and 2004 High-Voltage Workshop. Conference Record of the Twenty-Sixth International*, pages 403–407. IEEE, 2004.

[81] WH Prosser and MR Gorman. Plate mode velocities in graphite/epoxy plates. *The Journal of the Acoustical Society of America*, 96(2):902–907, 1994.

[82] Bruno Putzeys. Simple self-oscillating class d amplifier with full output filter control. In *Audio Engineering Society Convention 118*. Audio Engineering Society, 2005.

144

[83] Arthur E Quaid and Ralph L Hollis. Cooperative 2-dof robots for precision assembly. In *Robotics and Automation, 1996. Proceedings., 1996 IEEE International Conference on*, volume 3, pages 2188–2193. IEEE, 1996.

[84] Ajay Raghavan and Carlos ES Cesnik. Guided-wave signal processing using chirplet matching pursuits and mode correlation for structural health monitoring. *Smart Materials and Structures*, 16(2):355, 2007.

[85] Junuthula Narasimha Reddy. *Theory and analysis of elastic plates and shells*. CRC press, 2006.

[86] James A Rinde, Barry C Mathews, Miguel A Morales, Joel C Kent, Drew John Loucks, John Seymour Mattis, Jeff Dolin, Mark W Ellsworth, and Frank Wasilewski. Sealing system for acoustic wave touchscreens, July 3 2001. US Patent 6,254,105.

[87] Giulio Rosati, Maurizio Faccio, Christian Finetto, and Andrea Carli. Modelling and optimization of fully flexible assembly systems (f-fas). *Assembly Automation*, 33(2):165–174, 2013.

[88] Toshiiku Sashida and Takashi Kenjo. Introduction to ultrasonic motors. 1993.

[89] Eyal Setter and Izhak Bucher. Flexural vibration patterning using an array of actuators. *Journal of Sound and Vibration*, 330(6):1121–1140, 2011.

[90] Dan Shi. *Modelling of Mechanical Interaction in Piezoelectric Actuated Resonant System*. PhD thesis, EPFL, 2016.

[91] W Richard Smith, Henry M Gerard, Jeffrey H Collins, Thomas M Reeder, and Herbert J Shaw. Analysis of interdigital surface wave transducers by use of an equivalent circuit model. *IEEE Transactions on Microwave Theory and Techniques*, 17(11):856–864, 1969.

[92] David Su. Cmos rf power amplifiers: Nonlinear, linear, linearized. In *IEEE Santa Clara Valley Solid State Circuits Society Meeting*, 2002.

[93] Nobuo Tanaka, Scott D Snyder, Yoshihiro Kikushima, and Masaharu Kuroda. Vortex structural power flow in a thin plate and the influence on the acoustic field. *The Journal of the Acoustical Society of America*, 96(3):1563–1574, 1994.

[94] Touchscreen technology. *Available at http://suntroniclcd.com/touch-tech.html*, 2007.

[95] PS Tua, ST Quek, and Q Wang. Detection of cracks in plates using piezo-actuated lamb waves. *Smart Materials and Structures*, 13(4):643, 2004.

[96] KS Van Dyke. The piezo-electric resonator and its equivalent network. *Proceedings of the Institute of Radio Engineers*, 16(6):742–764, 1928.

[97] Christophe Vloebergh. *Modélisation et optimisation d'actionneurs piézoélectriques linéaires à onde progressive*. PhD thesis, Université catholique de Louvain, Louvain-la Neuve, 2010.

Bibliography

[98] Jun Yu, Meng Tong Tan, Stephen Michael Cox, and Wang Ling Goh. Time-domain analysis of intermodulation distortion of closed-loop class-d amplifiers. *IEEE Transactions on Power Electronics*, 27(5):2453–2461, 2012.

[99] Aharon Zeiger and Kenneth Jassby. Measurement of acoustoelastic coefficients of rayleigh waves in steel alloys. *Journal of Nondestructive Evaluation*, 3(2):115–124, 1982.

Curriculum Vitae

Xinchang LIU
Born on July 2nd, 1987

xinchang.liu@gmail.com

Educations

2013 - 2017	PhD student at Integrated Actuators Laboratory (LAI) in Microengineering, School of engineering in École Polytechnique Fédérale de Lausanne (EPFL, Swiss Federal Institute of Technology in Lausanne), Switzerland
2010 - 2012	Diplôme d'Ingénieur in Systems and Control in Ecole Supérieure d'Electricité (SUPELEC), France
2009 - 2012	Master of Science in Electrical Enginnering in Beihang University, Beijing
2005 - 2009	Bachelor of Science in Computer Science in Beihang University, Beijing

Publications

1. **X. Liu**, P. Germano and Y. Perriard, "Non periodic pulse width modulation spectral analysis with approximate decomposition of the signal," *2016 19th International Conference on Electrical Machines and Systems (ICEMS)*, Chiba, 2016, pp. 1-4.

2. **X. Liu**, Y. Civet and Y. Perriard, "Piezoelectric tactile device feedback generator using acoustic time reversal method," *2016 19th International Conference on Electrical Machines and Systems (ICEMS)*, Chiba, 2016, pp. 1-5.

3. **X. Liu**, Y. Civet and Y. Perriard, "Quality factor and vibration amplitude estimation of a piezoelectric-actuated system using impedance measurements," *2015 18th International Conference on Electrical Machines and Systems (ICEMS)*, Pattaya, 2015, pp.

1993-1996.

4. **X. Liu**, P. Germano, Y. Civet and Y. Perriard, "Design of a self-oscillating class D power amplifier for piezoelectric actuators," *2014 17th International Conference on Electrical Machines and Systems (ICEMS)*, Hangzhou, 2014, pp. 3386-3391.

5. **X. Liu**, Y. Civet and Y. Perriard, "Equivalent piezoelectric actuator circuits and comparison," *2014 IEEE/ASME International Conference on Advanced Intelligent Mechatronics*, Besacon, 2014, pp. 222-226.

6. **X. Liu**, D. Shi, Y. Civet and Y. Perriard, "Modelling and optimal design of a ring-type structure for the generation of a traveling wave," *2013 International Conference on Electrical Machines and Systems (ICEMS)*, Busan, 2013, pp. 1286-1291.